RICE UNIVERSITY

High Resolution Measurement and Modeling of Ion Dynamics in an Ultracold Neutral Plasma

by

Patrick McQuillen

A Thesis Submitted
in Partial Fulfillment of the
Requirements for the Degree

Doctor of Philosophy

Approved, Thesis Committee:

Thomas C. Killian, Chair
Professor of Physics and Astronomy

Barry F. Dunning
Sam and Helen Worden Professor of Physics

Stephan Link
Associate Professor of Chemistry

Houston, Texas

April, 2015

ABSTRACT

High Resolution Measurement and Modeling of Ion Dynamics in an Ultracold Neutral Plasma

by

Patrick McQuillen

Using high-resolution laser-induced fluorescence spectroscopy, ion dynamics in an expanding ultracold neutral plasma (UNP) have been studied in unprecedented detail. The evolution of the ion temperature is of great interest because the ions in an ultracold neutral plasma are strongly coupled, meaning their Coulomb interaction energy exceeds the thermal energy. This leads to novel plasma properties that are hard to describe theoretically. Understanding all the factors that contribute to ion temperature evolution is critical for designing schemes to cool the ions and achieve even stronger Coulomb coupling.

This work has also observed several phenomena that have not previously been studied in ultracold plasmas. Ion adiabatic cooling has been observed in a UNP for the first time, resulting in ion temperatures as low as 100 mK and up to a tripling of the Coulomb coupling parameter. The importance of electron-ion energy transfer is demonstrated with the first observations of electron-ion collisional heating. Inclusion of this effect into existing numerical models provides better agreement with experimental results. Results of molecular dynamics simulations of equilibrating plasmas have been compared to early time experimental data, which provides a new method of density determination that is much less sensitive to experimental systematics and

is accurate to within 10%. This improved certainty in the density allows accurate comparison between data and a theoretical model of the plasma dynamics. The agreement is excellent, but on a hydrodynamic time scale a small amount of extra heat (on order of 100 mK), not ascribable to electron-ion collisions or other sources in the model, is detected in the ion component. Potential sources are discussed within as well as proposals for further studies and improvements.

Acknowledgments

There are several people who undeniably must share credit for the accomplishments within this document. While I have not room to name them all, I hope to address everyone, at least in spirit.

First and foremost, my advisor Prof. Thomas Killian. Through the years he has consistently demonstrated unrivaled patience, passion for science, as well as incredible technical skills. His knack for finding optimism in the midst of obscurity is a cause for envy. Without him, I would not be here today.

In general, the community that is Rice University shares many extraordinary qualities, defining the atypical norm of this unique institution. I am honored to have worked with many great scientists while here. Thank you Dr. Jose Castro for welcoming me to the experiment and being such an inspiration during my beginning years at Rice. Prof. Barry Dunning, it has been both a pleasure and an honor to work with you. Prof. Anthony Chan, your enthusiasm for and skills at teaching have left an everlasting impression. Prof. Qimiao Si and Prof. Huey Huang, your classes challenged me to unexplainable lengths, I thank you for that humbling experience. To the current plasma team, Dr. Trevor Strickler and Thomas Langin, thank you for sharing the long hours and good times in making this project happen. To everyone, I've learned many great things from you all and our time together will always be remembered.

I thank my family for their love and support throughout the years. Their impact on my success can never be measured or repaid. Dad, you have taught me the meaning of responsibility and hard-work. Mom, you have taught me unwavering love and dedication to doing things 'my best'. I can't thank either of you enough. Brother,

you help keep me balanced and together we share some of my fondest memories.

No one has co-suffered through this experience as much as my life's partner, Dr. Emily Aaron. You are the epitome of beauty and you light my path through this crazy world. I can't wait to see where our road takes us, I'm sure it will be adventurous and full of excitement. Thank you for challenging my mind, heart, body and spirit.

Acquaintances come and go, true friends stay, marking the exception. Regardless, every relationships leaves it's impact and shapes who we become. With that in mind, I thank my fans as well as the haters, you both motivate me. Friends and family, it's time to feast on the spoils.

P.S. Thank you for nachos.

Contents

Abstract ii

Acknowledgments iv

List of Illustrations ix

1 Introduction 1

2 Ultracold Neutral Plasma Creation and Diagnostics 8

2.1 Creating Ultracold Neutral Plasmas of Strontium 8

2.2 Strontium UNP Diagnostics 11

2.3 Ion Absorption Spectroscopy 15

2.3.1 Considerations 18

2.4 Laser Induced Fluorescence Spectroscopy 20

2.4.1 Density Calibration 24

2.4.2 Regional Analysis 26

2.4.3 Full 2D Analysis 27

2.5 Frequency Calibration 33

3 Ultracold Neutral Plasma Dynamics 36

3.1 Introduction 36

3.2 Initial Temperatures 36

3.3 Non-Equilibrium Ions Dynamics 38

3.3.1 Disorder Induced Heating 38

3.3.2 Kinetic Energy Oscillations 39

3.3.3 DIH Magnitude 39

3.3.4 DIH Time Scale 42
3.3.5 Scaled KEOs 43
3.4 Adiabatic Expansion 47
3.5 Electron Ion Collisions 50
3.6 Three-body Recombination 58

4 Numerical Modeling of UNP Dynamics 59

4.0.1 Modeling Disorder Induced Heating and Kinetic Energy Oscillations 59
4.0.2 Adiabatic Expansion 64
4.0.3 Including Electron Ion Heating 68
4.0.4 Including Three-body Recombination 68
4.0.5 Complete Model 69
4.0.6 Evolution of Γ_i 71
4.1 Calibrating Density with Ion Temperature Evolution 86
4.1.1 Regional Density compared to T_{DIH} 86
4.1.2 Determining Regional Density from Kinetic Energy Oscillation Frequency, $2\omega_{KEO}$ 89
4.1.3 Fitting KEOs to MD Simulation Results 90

5 Anomalous Heating 91

5.1 Introduction 91
5.2 Mixing of Expansion Velocity 91
5.2.1 Region Size and Camera Gatewidth Effects 92
5.2.2 Imaging System Resolution 95
5.3 Anomalous Ion Energy 102
5.3.1 Density Perturbations 103
5.3.2 Enhanced Electron Heating 109
5.3.3 Optical Pumping 110

5.4 Conclusions 112

A Calculations **113**

A.1 Derivation of TBR Electron Cooling Shut off 113

A.2 Spectral Guessing Algorithms 114

A.3 Error Propagation 115

A.4 Numerically Simplified Formulas 116

B Useful Plots **117**

B.1 Size Corrections 117

B.1.1 Correction at later times 117

B.2 Typical Value Plots 120

B.3 2D Density Image Fits 121

B.4 Plasma Parameter Summary 122

C Image Analysis **124**

C.1 Salt and Pepper Code 127

C.2 Binning the Point Spread Function 129

D Bonus Material **132**

D.1 Improving Stability 132

D.2 Labview 134

D.2.1 10Hz Implementation 135

D.3 MATLAB 135

D.4 LaTeX 137

Bibliography **139**

Illustrations

1.1 At very high Coulomb coupling parameters strong correlations result in crystalline structure of a dusty plasma, (a) side view (b) top view. Dusty plasmas are formed by introducing micron-sized silica spheres, or "dust", into a plasma. The spheres accumulate significant charge, increasing the Coulomb interactions between dust particles and making them strongly coupled. Adapted from Ref. [1]. 2
1.2 Density and temperature phase space diagram of various plasma regimes. 4

2.1 Generalized timing diagram for UNP production at Rice. The 10 Hz master clock coordinates firing of the ionization lasers defining plasma creation time, t_0. A variable wait time elapses before the probing the plasma. The plasma evolution time, t, is defined to include half of the variable camera gatewidth (GW) as shown. 9
2.2 Level diagram for ^{88}Sr trapping and photoionizing. 10
2.3 Level diagram for $^{88}Sr^{+}$ ion. The 422 nm transition is used for imaging as well as ion manipulation (such as optical pumping). 12
2.4 Schematic representation of UNP imaging system (not to scale). Laser induced fluorescence is imaged into the ICCD by a 1:1 optical relay and 1X Macro lens or the 1x Macro can be replaced with a microscope objective setup for selectable 4x and 10x magnification. The orange arrows indicate focusing degrees of freedom. 14

2.5 Two dimensional image of areal ion density obtained by ion absorption spectroscopy. $\hat{x}$ and $\hat{y}$ are defined in the traditional Cartesian sense. 17

2.6 Typical spectrum evolution obtained by ion fluorescence spectroscopy for the center of a UNP. Fitting each spectra to a Voigt profile provides a measure of ion temperature, density and center frequency (green dashed lines). The results of the fit parameters as well as the plasma expansion time are shown in each legend. Blue dashed lines showing adaptive guesses which result in faster re-analysis times and helps ensure proper fitting over a wide range of UNP parameters. Notice the difference in spectral widths between 3.3 K (middle top) and 0.9 K (bottom left), reflecting the cooling of the ions. 25

2.7 Cartoon depicting geometry of regions (vertical white strips) for regional analysis of UNPs at 4x magnification, relative size of regions and plasma is to scale, however there are typically 85 regions within the 1 mm^2. Since the regional filter is 3 pixels wide, each region overlaps one column of pixels with each of it's neighbors. The regions are numbered left to right. 27

2.8 Typical spectrum evolution obtained by ion fluorescence spectroscopy for a region 0.5 mm to the left of plasma center. Notice the evolution of the center frequency, which is negatively proportional to the $\hat{x}$-component of the bulk velocity within the region. This clearly shows the movement of ions to the left, i.e. away from plasma center. The uneven spacing of detunings was intentional in order to improve fit performance of centered spectra, however we see it is not ideal for off-centered spectra. The degree of irregularity has since been reduced. 28

2.9 Same as 2.8 except for a region 0.5 mm to the right of plasma center. Notice the down-shifted center frequencies reflecting the right going bulk velocities. 29

2.10 Regional analysis of a UNP with $T_e(0) = 430\,\mathrm{K}$ and $\sigma_0 = 1\,\mathrm{mm}$. Results are plotted versus time and thus display the evolution of ion fluorescence spectra fit parameters. Color reflects the plasma region number which from left to right, goes from red through purple. Each region is 12.6 µm wide. Black markers indicate robust averages taken at each time point. These are the values displayed throughout this thesis. Notice how both the density and temperature decrease as the time evolves and the plasma expands. Center frequencies are negatively proportional to the $\hat{x}$-component of the ion's bulk velocity and their behavior displays the expansion dynamics. Offset is an extra fit parameter to account for any additive offset on the spectra. It is plotted relative to the signal peak. 30

2.11 Regional analysis of a UNP with $T_e(0) = 430\,\mathrm{K}$ and $\sigma_0 = 1\,\mathrm{mm}$. Results are plotted versus region number and thus represent a 1D cut (along $\hat{x}$) through the center of the plasma, $\pm$ 0.5 mm from center. Color reflects the plasma evolution time, t, as displayed in the legend. From this perspective we can see features within both the density and temperature profiles. The center frequency plot clearly shows the bulk velocity's linear dependence on x 31

2.12 Small region analysis of the entire field of view results in high resolution 2D maps of ion temperature, density and center frequencies. Here time passes from left to right. 32

2.13 Saturated absorption signal from Rb scan (white) with fit to a triple Lamb dip model, i.e. Eqn. 2.19 (red) plotted versus control voltage, V, allows for calibration of control voltage to imaging beam detuning as well as determination of imaging laser linewidth. 34
2.14 Rb saturated absorption signal (white-left y-axis) including beat note measurement (red-right y-axis) shows highly linear response to imaging beam frequency control voltage, V (x-axis). 35

3.1 Typical values of ω_{pe}. 37
3.2 Typical values of ω_{pi} for UNP of ^{88}Sr. 39
3.3 Early time ion temperatures show disorder induced heating and kinetic energy oscillations. Notice the dependence on density in both the magnitude of temperatures as well as the time scale for oscillations. 40
3.4 Typical values of κ plotted versus T_e and n, calculated from Eqn. 3.3. 42
3.5 Typical values of a_{ws} plotted versus n. 43
3.6 Typical values for λ_D plotted versus T_e and n, calculated from Eqn. 3.4. 44
3.7 Calculated DIH equilibration temperatures from MD simulations of Yukawa systems 44
3.8 Calculated Γ_i for DIH equilibration temperatures. The seemingly interesting regime of high density low electron temperature is not only experimentally inaccessible for us, but it is precisely the regime of strong electron coupling which presents many complications as discussed in Secs. 3.6 and 4.0.6 45
3.9 Early time ion temperatures show disorder induced heating and kinetic energy oscillations. This is the same data as Figure 3.3 but here the temperatures has been scaled by the DIH temperature calculated as in Eqn. 3.5 and time has been scaled by the ion plasma oscillation period, i.e. the inverse of Eqn. 3.6. 46

3.10 Long time temperature evolution shows the rapid DIH then a decrease from the equilibrium temperatures as the UNP adiabatically expands into the vacuum chamber. The time scale is set by the electron temperature and the cloud size. Here we have varied the electron temperature by nearly an order of magnitude. Initial cloud radius is, σ_0 =1 mm 47
3.11 Typical values for τ_{exp} plotted versus $T_e(0)$ and σ_0. 48
3.12 Long time temperature evolution shows decrease from DIH temperatures as the UNP adiabatically expands into the vacuum chamber. Same data as 3.10 but the temperatures have been scaled by T_{DIH} and the times by τ_{exp}. 50
3.13 Typical values for $\ln[\Lambda]$ plotted versus T_e and n, calculated with Eqn. 3.20. 53
3.14 Typical values for $\frac{dT_i}{dt}$ due to electron-ion heating plotted versus T_e and n, calculated with Eqn. 3.24 assuming a constant density and T_e. 54
3.15 Typical values for τ_{EIC} plotted versus T_e and n, calculated with Eqn. 3.25. 55
3.16 Total temperature gained by ions due to ion-electron collisions over a time equal to τ_{exp} for a 1 mm ^{88}Sr UNP. Note, this figure does not account for changing the plasma conditions due to the global expansion. 56
3.17 Similar to Fig. 3.16 except normalized by initial disorder induced heating temperatures. 57

4.1 Linear approximation of DIH (i.e. Eqn. 4.2) compared to early time experimental data for a range of densities and electron temperatures. Qualitative agreement is good however the model clearly lacks kinetic energy oscillations. 61

4.2 Molecular dynamics simulation of kinetic energy oscillations compared to experimental data. Early time ion temperature measurements agree well with results from MD simulations of equilibrating Yukawa plasmas. Here density is a single fit parameter which agrees with calibration by absorption. Discrepancies tend to increase as time passes hinting at longer time scale dynamics. 63

4.3 Molecular dynamics simulation of kinetic energy oscillations adjusted for EIC and adiabatic cooling compared to experimental data. Adjusting molecular dynamics results for EICs and adiabatic cooling enhances agreement slightly. Solid lines are the adjusted simulation results and dashed lines are the raw unadjusted MD results. The remaining discrepancy in the T_E =430 K data will be addressed later. 65

4.4 Experimental ion temperature measurements compared to numerical models of UNP dynamics. Dashed lines are results of 4.8 through 4.12 and clearly miss a significant amount of energy when compared to experimental data points. The solid lines represent the inclusion of electron ion collisional heating (solution to Eqns.4.22 through 4.26) and clearly do a better job describing data across all regimes. The insets show fits of early time data fit to MD simulations which are used to determine density. 74

4.5 Excess temperature observed in the ions when compared to full numerical model, Eqns.4.22 through 4.26. Discrepancies on the order of 200 mK to 400 mK are typical. Higher density seems to increase the extra energy. 75

4.6 Measured density evolution for data presented in Fig. 4.4. Within a few expansion timescales, densities plummet by orders of magnitude, to levels which begin to become experimentally challenging, i.e. $n_i < 10^{13}$ m^{-3}. 76

4.7 Calculated electron temperature evolution for data presented in Fig. 4.4. 77
4.8 Calculated Γ_e for data presented in Fig. 4.4. Both strongly coupled regimes (top row) and weakly coupled regimes (bottom row) are easily accessible through experimental studies of UNPs. The results do not represent either limit of accessible values for Γ_e 78
4.9 Calculated ion temperature values after the first τ_{exp}, without electron-ion thermalization, i.e. Eqns. 4.22 through 4.26 without the EIC term, $\frac{T_e(t)-T_i(t)}{\tau_{EIC}}$. 79
4.10 Calculated ion temperature values after the first τ_{exp}, with electron-ion thermalization, i.e. Eqns. 4.22 through 4.26. 79
4.11 Calculated Γ_i for data presented in Fig. 4.4. Dashed lines show expected evolutions calculated with and without EICs, (red and blue dashed line, respectively) The remaining discrepancy from experimental values is attributed to extra ion heating unaccounted for in our model. 80
4.12 Ion coupling parameter values after the first τ_{exp}. Results are calculated via Eqns. 4.22 through 4.26 without the EIC term, $\frac{T_e(t)-T_i(t)}{\tau_{EIC}}$. 81
4.13 Ion coupling parameter values after the first τ_{exp}. Results are calculated via Eqns. 4.22 through 4.26. The optimal density is a result of suppressed coupling due to electron-ion heating at higher densities. 82
4.14 Ion coupling parameter values at $t = 2\tau_{exp}$. Further suppression is visible at the highest densities. High initial density results in longer timescales for electron-ion heating before dropping densities quench collisions. 83
4.15 Ion coupling parameter values at $t = 4\tau_{exp}$. 83
4.16 Ion coupling parameter values at $t = 4\tau_{exp}$ for 2 mm cloud. 84

4.17 Ion coupling parameter values at $t = 4\tau_{exp}$ for 0.5 mm cloud. 84

4.18 Calculated $\tilde{\Gamma}_i$ for data presented in Fig. 4.4. Dashed lines show expected evolutions calculated with and without EICs, (red and blue dashed line, respectively) The remaining discrepancy from experimental values is attributed to extra ion heating unaccounted for in our model. 85

4.19 Kinetic energy oscillations in RMS from tree code simulations of equilibrating zero temperature electrons show that electron temperatures oscillate such that the equilibrium temperature (shown by dashed line) skims the top of the KEOs. $\rho_i = 1 \times 10^{20}\,\mathrm{m}^{-3}$, $1 \times 10^{19}\,\mathrm{m}^{-3}$, $1 \times 10^{18}\,\mathrm{m}^{-3}$ and $1 \times 10^{17}\,\mathrm{m}^{-3}$ (from top to bottom). Notice how the lack of a screening species qualitatively effects the dynamics. Copied from [2] 87

4.20 Molecular dynamics simulation of disorder induced heating for an UNP with $n_i = 4e16$ m^{-3} and $T_e = 60\,\mathrm{K}$. The dark grey line represents the true rms spread of ion velocities while the grey line is a fit to the velocity distribution using a Voigt profile. The discrepancy between the two can be attributed to the fact the ions are not in thermal equilibrium. The lower panes show details of the velocity distribution at four time points indicated by vertical grey lines in the upper panel. The actual velocity distributions are shown in black and corresponding Voigt fits in grey, notice the deviations in the wings due to high energy ions, particularly before the DIH peak and during the subsequent troughs of the KEOs. Copied from [3]) 88

5.1 Center frequencies of LIF spectra for neighboring regions in an UNP of $T_e = 430\,\mathrm{K}$ and the characteristic radius is σ =0.9 mm. Average spacing is about 2.7 MHz for a single pixel region width of 13 µm . . . 94

5.2 Increasing the region width results in spectral broadening and higher measured temperatures. Here $T_e = 430\,\mathrm{K}$, $n_0 = 2 \times 10^{15}\,\mathrm{m}^{-3}$ and $\tau_{exp} = 5\,\mu\mathrm{s}$. These parameters represent the fastest expansion for our typical regime and thus reflect the greatest potential broadening. . . . 95

5.3 Data taken at 1x magnification and without truncating the imaging beam into a thin sheet. Large temperature discrepancies on order 5 K are observed. 97

5.4 Comparison of datasets for similar UNPs taken at different magnifications show extra heating in the case of non magnified images. Unfortunately the plasma does not evolve far in these scans but the difference is clear and repeatable. Presumably the discrepancy should increase as plasma expansion accelerates. 97

5.5 Central peak of experimentally obtained and post processed PI-MAX2 ICCD's PSF. 99

5.6 Log plot of PSF amplitude versus radius shows far reaching extent of PSF. Rotationally filtering the signal greatly increase the SNR of the measured PSF. 100

5.7 PSF with compressed colormap highlights extent of PSF out to about $\pm$ 100 pixels 100

5.8 Rotationally symmetric 2D Tunkey window used to truncate the measured PSF. 101

5.9 Results of windowing the PSF, notice how the peak is uneffected while the edge of the signal tapers off towards zero. 101

5.10 2D images of UNPs created with different MOT expansion times (top row). Note the decreasing structure within the normalized residues from a 2D Guassian fit as evolution time passes, particularly noticeable out to 500 µs. It is postulated this structure induces ion motion and contributes to ion heating. 104

5.11 (Top Left) Ion temperatures are higher for plasmas created from MOTs with less expansion time. (Top Right) Initial densities are similar and follow similar evolutions when scaled by τ_{exp}. (Bottom Left) The shielded coupling parameter reaches higher values for datasets with $t_{MOT} \geq$500 µs. 105
5.12 Comparison of coaxial versus transverse ionization (relative to fluorescence beam) shows earlier and more significant extra heating for transverse ionization. This supports the idea that extra energy is the result of ionization modulation induced ion motion. For this study, $T_e = 50\,\mathrm{K}$ and $n = 4 \times 10^{15}\,\mathrm{m}^{-3}$ 108
5.13 Detailed regional analysis of transversely ionized UNP shows significant structure in both density and temperature profiles consistent with ionization induced ion motion. 109
5.14 Detailed regional analysis of coaxially ionized UNP shows less significant structure in temperature profiles. 110
5.15 Artificial broadening of ion florescence spectra due to optical pumping to the dark state. Notice how imaging times of even 200 ns can begin to cause 10% deviations in measured ion temperature. . . 111

B.1 Size correction,Z_{corr}, plotted versus beam:cloud radius ratio 117
B.2 Slit correction, $Slit_{corr}$, plotted as a function of slit:cloud and beam:cloud size ratios 118
B.3 Total correction, $Slit_{corr} * Z_{corr}$, plotted as a function of slit:cloud and beam:cloud size ratios 119
B.4 Typical values for the electron Coulomb coupling parameter, Γ_e plotted versus T_e and n. 120
B.5 Typical values for the ion Coulomb coupling parameter, Γ_i plotted versus T_i and n. 121

B.6 Evolution of 2D density images constructed from calibrated fluorescence spectroscopy signal. 122
B.7 Summary plasma parameter plot offers a convenient summary of useful plasma parameters for quick reference and review. 123

C.1 Results of salt and pepper removal on each image and each background. The automated elimination of extreme outliers results in better overall data quality and enhanced image contrast. Results are for various cutoff criteria of 2,4, or 6 times the local standard deviation. The process is ran on each detuning's image and background seperately, however, results are shown for the calibrated density representing an integration over detunings. Notice how a cutoff of $2\,\sigma_{SD}$ results in a slight alteration of measured peak density and is thus considered too stringent. Cutoff values of $4\,\sigma_{SD}$ and higher do not affect spectra fits results, other than sometimes improving error bars. 126
C.2 Running the process on each image, each background and then the image after background subtraction (i.e. $I_{img} - I_{bkd}$) yields even better results, as compared to Fig. C.1. 127
C.3 PSFs with various binning. Color indicates percentage of total signal within that pixel. 131

Chapter 1

Introduction

Most plasmas, such as in the sun, a fluorescent lamp bulb, or a candle flame, have temperatures on the order of or greater than the energy scale needed to collisionally liberate electrons and create a gaseous collection of charged particles. At lower temperatures, particles recombine into neutral atoms and molecules and systems typically do not exist in the plasma state. However, there are exotic plasmas that violate this tendency. One such example is ultracold neutral plasmas, which are created by photoionizing laser-cooled atoms near the ionization threshold. This results in ion temperatures below 1 degree kelvin and tunable electron temperatures that can be as low as a few kelvin.

Ultracold plasmas are of great fundamental interest because they can be non-ideal, or strongly coupled. The degree of strong coupling is characterized by the Coulomb coupling parameter, Γ, defined as the ratio of nearest-neighbor potential energy to thermal energy. For a bare Coulomb potential (i.e. neglecting electron shielding of the ion potential), the coupling parameter, for electrons (e) or ions (i), can be written as,

$$\Gamma_{e,i} = \frac{1}{4\pi\varepsilon_0}\frac{e^2}{a_{ws}k_B T_{e,i}}, \tag{1.1}$$

Where $\pi = 3.1415926535897...$, ε_0 is the permittivity of free space, e is the electron charge, a_{ws} is the average interparticle spacing (aka the Wigner-Seitz radius), k_B is

the Boltzmann constant, and $T_{e,i}$ is the electron or ion temperature. * Typical values for Γ_e and Γ_i are shown in Fig. B.4 and Fig. B.5, respectively.

Plasmas are strongly coupled when $\Gamma > 1$. For $1 < \Gamma \lesssim 170$ the plasma component is in the liquid-like regime and for $\Gamma \gtrsim 170$ the plasma component becomes solid. Crystalline structure has even been directly photographed, in the case of dusty plasma experiments, see Figure 1.1. [1]

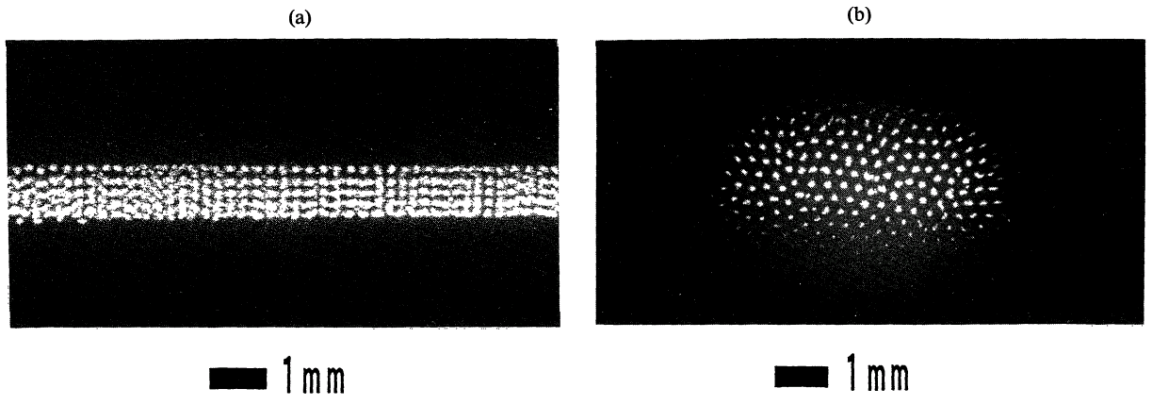

Figure 1.1 : At very high Coulomb coupling parameters strong correlations result in crystalline structure of a dusty plasma, (a) side view (b) top view. Dusty plasmas are formed by introducing micron-sized silica spheres, or "dust", into a plasma. The spheres accumulate significant charge, increasing the Coulomb interactions between dust particles and making them strongly coupled. Adapted from Ref. [1].

These non-ideal (aka strongly coupled) plasmas are a forefront of plasma physics research. [4] They are interesting and challenging because they violate the fundamental plasma approximation, i.e. that collisional interactions are dominated by the cumulative effects of many, weak, long-range Coulomb collisions. At very high densities or very low temperatures, correlations (in both velocity and position) become

*Standard SI units are used throughout this thesis (meter,Kelvin,Hz,etc.) while literature referenced varies by author.

significant and long range order prevails, i.e. short-range, binary, particle-particle interactions and collisions become important and new physics occurs. [5]

Much interest in strongly coupled plasmas stems from inertial confinement fusion efforts, in which plasmas are compressed beyond solid densities in order to harness fusion energy. [6, 7] These systems can also be strongly coupled, making it important to understand the effect of strong coupling on thermalization and transport processes in order to model and optimize the plasmas. [8] It is very difficult to directly study these effects in fusion plasmas and other similar high-energy density systems formed by laser-matter interactions because the required facilities are very expensive, diagnostics are indirect, and the timescale for plasma dynamics is very fast. Model systems, like ultracold neutral plasmas, provide an important, experimentally accessible window into strongly coupled physics [9]

Other examples of strongly coupled plasmas include dusty plasmas, certain astrophysical objects such as white dwarfs, and ultracold molecular beam plasmas. [10, 11, 12] They are also produced in some industrial processes. [13] Figure 1.2 shows a density-temperature phase diagram of various neutral plasma regimes.

The importance of spatial correlations between particles and the strong particle interactions significantly complicates theoretical efforts to describe strongly coupled plasmas and many of the traditional hydrodynamic and kinetic tools become questionable in the strongly coupled regime. [14] While some theories have been extended [15, 16, 17] many phenomena in strongly coupled plasmas can only be described with full molecular dynamics simulations, which are very computationally expensive. [18] Due to limitations in computational power, even molecular dynamics simulations cannot currently treat all the complexities of an ultracold neutral plasma, such as electron and ion dynamics, and plasma expansion, which all occur on very different

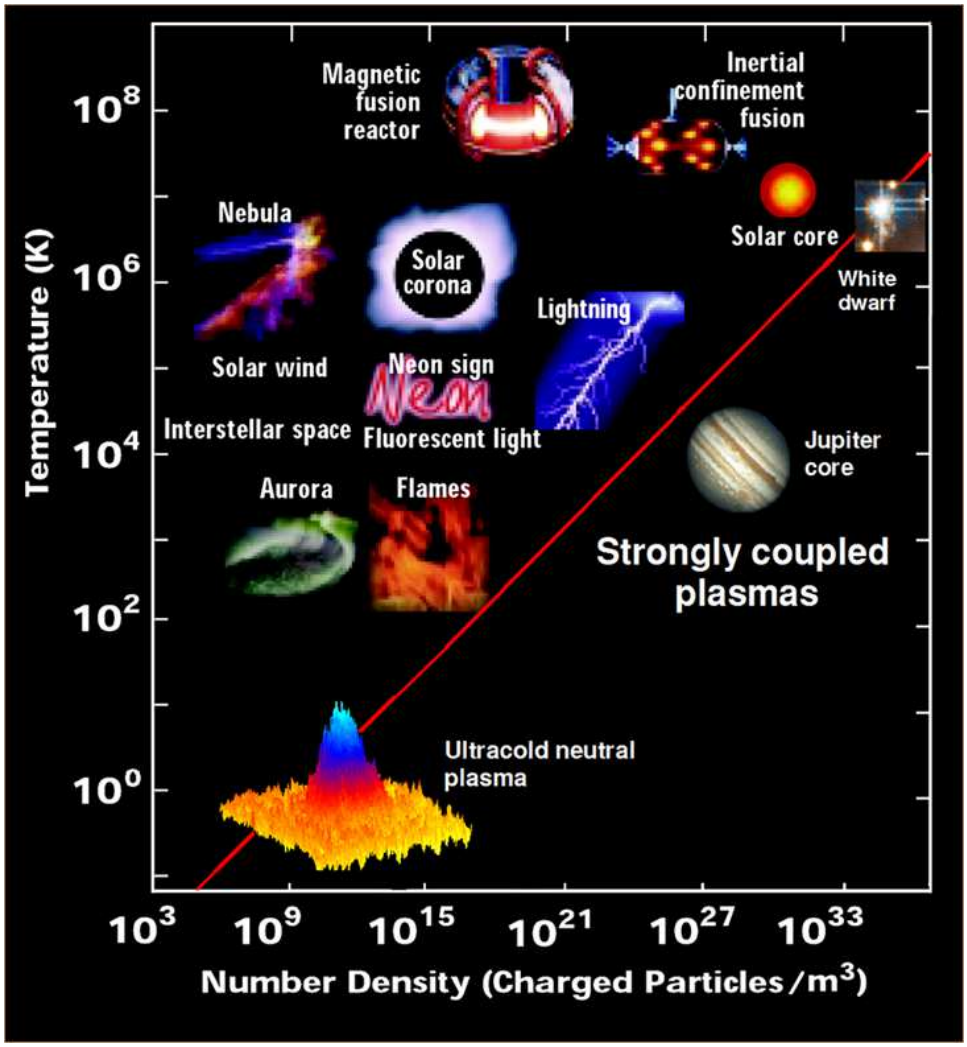

Figure 1.2 : Density and temperature phase space diagram of various plasma regimes.

timescales. Therefore experimental probes of strongly coupled plasmas are paramount to the advancement of the field.

Ultracold neutral plasmas, created by photoionizing laser cooled atoms, provide a well suited test-bed for benchmarking theories and exploring strongly coupled plasma physics, all within a table top, extremely clean and well-controlled environment.[19] The use of well-known atomic physics techniques allows precise control and diag-

nostics mediated by laser-atom interactions. They are created in a completely non-equilibrium state and thus provide opportunity for studying non-equilibrium physics, as well as thermalization-rate measurements.[20, 21] Many previous studies have focused on collective modes of both the strongly-coupled ions [22, 23, 24] and weakly-coupled electrons. [25, 26, 27, 28] They are also closely related to the ultracold Rydberg gas and many studies have been performed exploring the overlap and transition between the two systems. [29, 30, 31, 32, 33]

The current methods to create UCNPs yield a very limited range of equilibrium $\Gamma_i = 1-4$ over a surprisingly large range of initial experimental conditions. [34, 35, 36] Thus there is great interest in the possibility of creating even more strongly coupled ultracold neutral plasmas with a range of proposals including laser cooling of the ions [37, 38], and ionizing atoms that already possess a degree of spatial correlation such as from an optical lattice, [39, 40] a quantum degenerate Fermi gas, [41] or a Rydberg-blockaded sample. [39, 42] Making more strongly coupled plasmas would provide access to a wide range of new physics.

In weakly coupled plasmas, the relaxation of correlations towards equilibrium occurs much faster than the relaxation of the single particle distribution function, creating a hierarchy of timescales known as the Bogoliubov hypothesis in kinetic theory. [43] This is consistent with the molecular chaos hypothesis introduced by Boltzmann that particles are uncorrelated between collisions, [44] and it leads in general to exponential relaxation of thermodynamic properties towards equilibrium. However, this description no longer applies in strongly coupled plasmas for which these timescales become comparable [45, 46, 47, 48, 49]. Also, the relaxation of correlations leads to an exchange of energy between kinetic and potential energy [45, 47, 49] that is large in strongly coupled plasmas and cannot be neglected. The potential

discoveries studying more strongly coupled UCNPs are numerous and diverse. A modest increase in the coupling parameter, i.e. $\Gamma \sim 30$ induces liquid-like behavior and caging effects should become prominent, which qualitatively changes the particle dynamics. [50, 51, 52]

This thesis concentrates on accurate measurement and predictive calculation of fundamental plasma parameters important for understanding the evolution of the ion temperature and the ion Coulomb coupling in an UNP, namely local ion density and ion temperature. Detailed studies of systematic concerns identified numerous sources of error in ion temperature measurements and effects that could lead to an apparent increase in ion temperature. These are now avoided through better understanding of experimental constraints, revisions to regional analysis techniques, experimental upgrades, and advanced digital image processing. Density calibrations were also greatly improved by leveraging known equilibrium processes, namely the frequency of kinetic energy oscillations.

With a refined and calibrated probe we compared experimental results to the most complete numerical UNP model available [53] and observed, for the very first time, ion adiabatic cooling in an UNP. [54] Similar to an ideal gas the plasma will cool as it expands into the surrounding vacuum and by simply allowing the plasma to evolve, temperatures as low as 100 mK were observed. The expansion of plasmas into a vacuum has been a long standing problem of interest both experimentally and theoretically. [55, 56, 57, 58, 59, 60, 61, 62, 63, 64, 65, 66] It is typically the dominant effect in the dynamics of plasmas created with pulsed lasers, [67] such as in experiments pursuing inertial confinement fusion, [68] x-ray lasers, [69] or the production of energetic (>MeV) ions through irradiation of solids, [70, 71] thin foils, [72] and clusters. [73] Exciting theoretical predictions in UNP systems show that as

plasma expands, the coupling parameter increases and accurately reflects correlations within the ions, at least initially. [38, 74, 75] Indeed, we observe coupling parameters of up to $\Gamma = 6 \pm 1$, nearly tripling the initial coupling strength!

It was consistently found that experimental temperatures were higher than calculations predicted, by up to several 100 mK. This discrepancy was mitigated by the inclusion of electron-ion collisional thermalization, an exchange that had previously been considered insignificant in our regimes. This represents the first demonstration of electron-ion collisional energy transfer in a UNP. [54] After inclusion of electron-ion thermalization the good agreement between revised theory and measurement shows that there is very little additional heating that cannot be explained by known sources. Potential sources for the remaining discrepancy of up to a few 100 mK as well as possible solutions are discussed within.

In general, inter-species heat exchange is a big and interesting problem. It is particularly important for inertial confinement fusion experiments. [7, 76, 77] Beyond that, precise understanding of the underlying collision rates is key to understanding numerous plasma phenomena; not only multi-species temperature relaxation rates [78, 79, 80, 81, 82], but also stopping power [83], diffusion [84], thermal conductivity [85, 86, 87, 84], and electrical conductivity [85, 88, 89, 90, 86, 87, 91].

These studies are not only of great fundamental interest but pave the way for future efforts such as laser cooling of the ions and, the goal being, even more strongly coupled plasma systems.

Chapter 2

Ultracold Neutral Plasma Creation and Diagnostics

Ultracold neutral plasmas at Rice University are made with pure atomic strontium. [34] Alkaline earth atoms make ideal candidates for precision studies of ultracold neutral plasmas. Due to the dual valence electron structure, a singly ionized ion is electronically similar to an alkali atom. This single valence structure is well understood and provides access to a powerful set of diagnostics mediated by laser-valence electron interactions, i.e. absorption and LIF (laser-induced-fluorescence) spectroscopy, which can measure ion densities and velocity distributions, *in situ*. By imaging with an ICCD (intensified charge coupled device) these diagnostics are extremely sensitive (single photon detection) with high spatial ($\sim 10\,\mu m$) and temporal ($\sim 10\,ns$) resolution, all together permitting unprecedented probing of a clean plasma system.

The ultracold neutral plasma creation and diagnostics techniques at Rice have been well described in numerous sources [19, 34, 92, 93, 94, 66] so the following chapter will only contain a concise review aimed at understanding the calibration of density and accuracy of temperature measurements. For a detailed discussion on the internal operations of the camera see Ref. [95].

2.1 Creating Ultracold Neutral Plasmas of Strontium

We make our UNPS by photoionizing laser-cooled ^{88}Sr atoms collected in a magneto-optical trap (MOT). Plasmas are produced and probed at a 10 Hz rate and data are

accumulated for $\geq$ 100000 shots per typical dataset, see Fig. 2.1 for a generalized timing diagram.

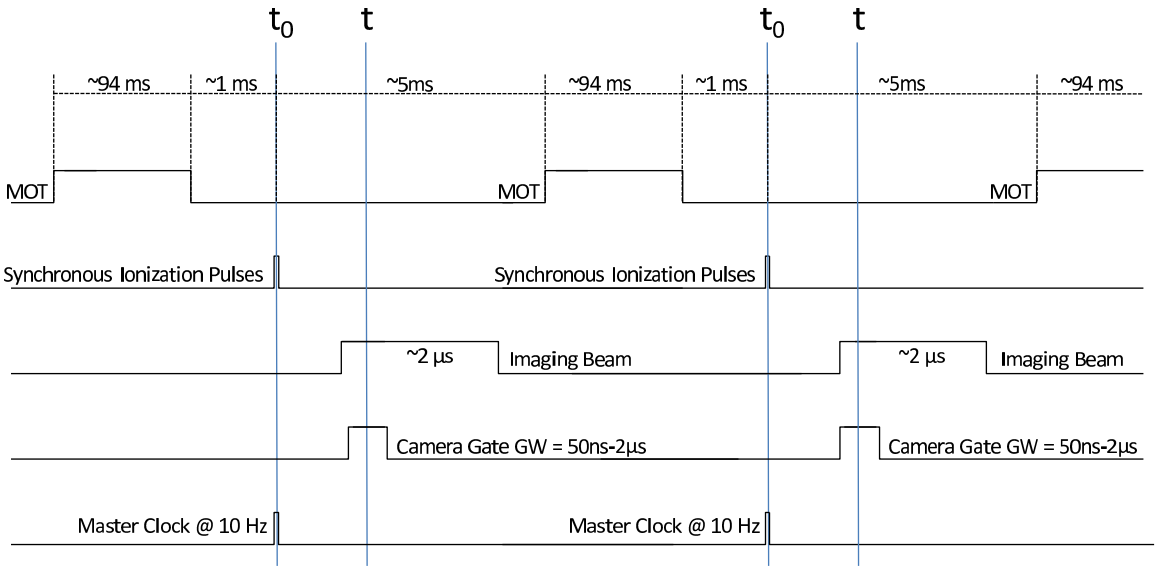

Figure 2.1 : Generalized timing diagram for UNP production at Rice. The 10 Hz master clock coordinates firing of the ionization lasers defining plasma creation time, t_0. A variable wait time elapses before the probing the plasma. The plasma evolution time, t, is defined to include half of the variable camera gatewidth (GW) as shown.

Strontium atoms originate from a small nozzled aperture on a resistively heated oven of 99% pure strontium metal. The four stable isotopes (^{84}Sr, ^{86}Sr, ^{87}Sr, and ^{88}Sr) are found in their naturally abundant ratios (0.56%, 9.86%, 7.0%, and 82.58%, respectively), however laser cooling is isotope selective and we only affect ^{88}Sr via the primary electronic transition $^1\mathbf{S}_0 - {}^1\mathbf{P}_1$ at 461 nm, see Fig. 2.2. The atom beam first passes a 2D collimation stage in which the atoms are Doppler cooled in both transverse degrees of freedom. A Zeeman slower then cools in the axial direction. Ultimately, a fraction of the atoms are then cool enough to be captured by the MOT.The atom trap typically captures about 1×10^9 atoms in a spherical Gaussian cloud with a characteristic $e^{-1/2}$ radius of $\sigma \approx 0.5$ mm to 2 mm and atom temperatures

of about 10 mK. The necessary 461 nm laser light is generated in two lab-made second-harmonic-generation cavities (based on $KNbO_3$), pumped by a continuous wave Ti:sapphire laser at 922 nm.

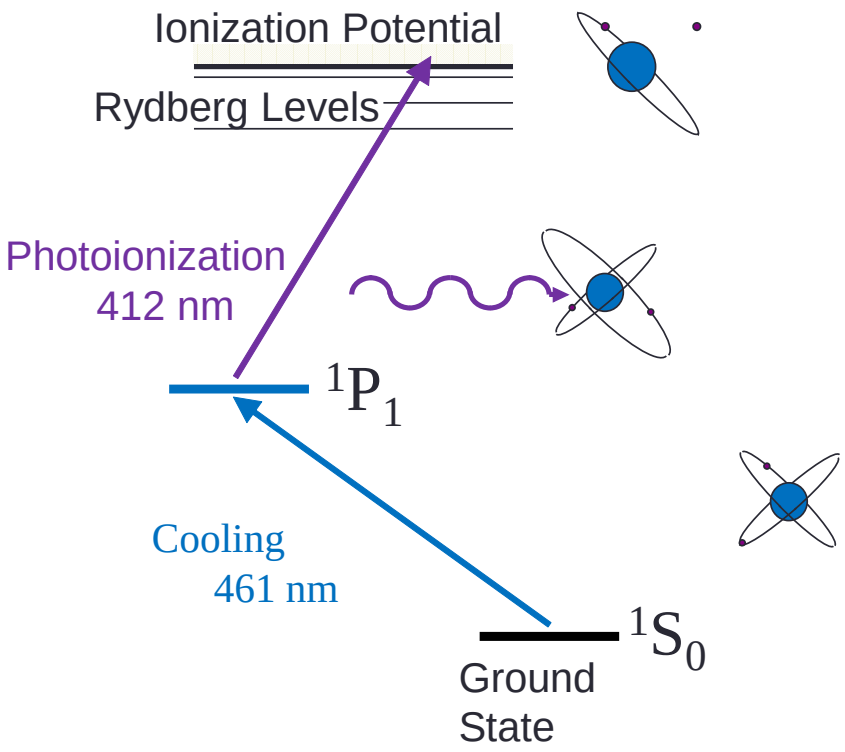

Figure 2.2 : Level diagram for ^{88}Sr trapping and photoionizing.

About a millisecond before ionization, the MOT beams and fields are turned off and the atoms begin to ballistically expand. Using a pair of 10 ns pulses at 461 nm and 412 nm, a single electron is liberated from a fraction of the atoms, see Fig. 2.2. Ionization fractions are typically 10-30%, but can approach 100% near an autoionizing resonance. [96, 97] The pulse pairs originate as the third harmonic (355 nm) from a pulsed Nd:YAG laser which is split into two paths; one pumps a 461 nm-seeded

Bethune-style dye cell of coumarin-460 in methanol and the other pumps a three stage pulse dye laser using exalite-411 in p-Dioxane to produce a wavelength tunable pulse about 412 nm. The high intensity of the pulse amplified 461 nm light greatly saturates the intermediate transition. The ionization fraction is controlled, and limited by the intensity of the 412 nm beam which permits spatially resolved control of the initial density distribution. [22, 23, 24] The wavelength of the 412 nm pulse determines the initial kinetic energy of the electrons and therefore their initial temperature, with 1 K resolution.

The plasma and any unionized atoms are free to evolve under their own forces (or those we externally impose). From a macroscopic view the prominent dynamics include a rapid expansion of the plasma cloud, driven by the electron thermal pressure. This offers a few milliseconds to conduct experiments before the plasma dissipates into the surrounding vacuum. The 10 Hz production rate is an operating requirement of the Nd:YAG laser and is imposed by an external master clock and high resolution timing generators. Thus, plasma creation time, t_0, and all other triggers within the experiment are well known to within ± 10 ns.

2.2 Strontium UNP Diagnostics

Post ionization, a variable wait time elapses and the plasma is probed via laser-ion scattering at a imaging wavelength of $\lambda_{img} = 422$ nm, see Fig. 2.3. We have two methods available to us. In ion absorption spectroscopy, the shadow from the atoms is analyzed to obtain an areal density distribution. In ion fluorescence spectroscopy, scattered light is recorded to measure density and velocity distributions. In general, fluorescence spectroscopy benefits from higher signal to noise ratio (SNR) and, with proper considerations, the capability of distinguishing thermal kinetic energy from

bulk motion. Absorption imaging benefits from being an absolute measurement and it has historically been used for calibration of fluorescence signal to density. Both techniques will be discussed in further detail in the following sections.

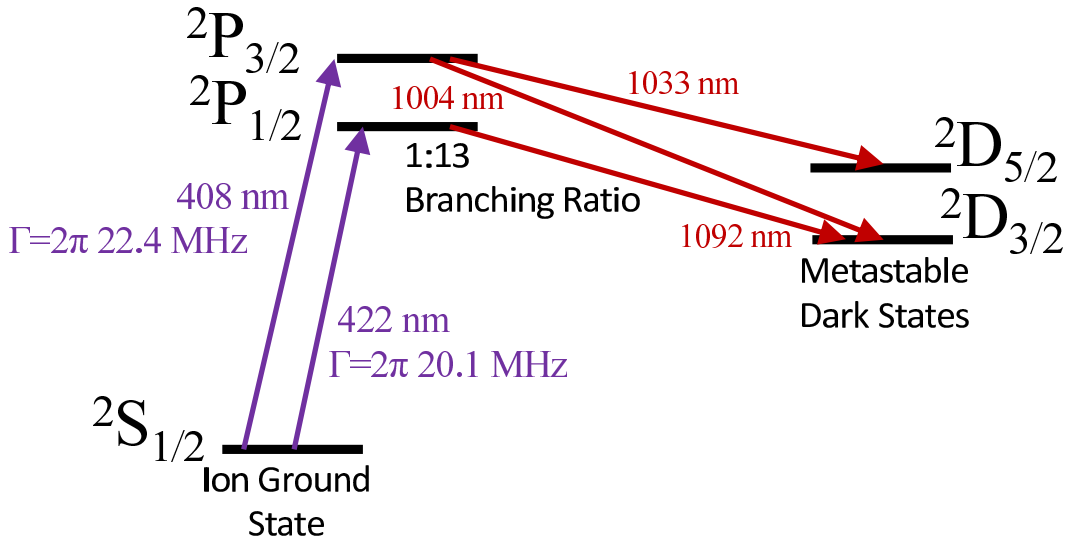

Figure 2.3 : Level diagram for $^{88}Sr^+$ ion. The 422 nm transition is used for imaging as well as ion manipulation (such as optical pumping).

Incidentally the $^2\mathbf{S_{1/2}} - {}^2\mathbf{P_{3/2}}$ transition at 408 nm could be used for diagnostics and ion manipulation just as well. The primary reasons for originally using 422 nm light, 15 years ago, was that of compatibility with standard optical coatings, slightly better quantum efficiency of detectors and viable access to a laser source. Today, 408 nm light can be obtained from Blu-Ray diodes which are naturally centered about 405 nm. Using modern Blu-Ray burners hobbyist have reported several 100 mWs without temperature regulation, using low-grade power supplies. This amount of power is an order of magnitude greater than what we have available using 422 nm light (roughly 30 mW) and could saturate the transition over the entire plasma cloud. This scenario could potentially be useful for laser cooling of the ions. Over the years the pieces of a Blu-Ray burner diode injection locked by an extended cavity diode

laser have been collected and demonstrated individually, however they have not been implemented as one and injection locking remains to be accomplished.

The additional transitions shown in Fig. 2.3 shows various metastable dark states that are long-lived compared to typical plasma time scales and thus prevent an ion from further scattering of imaging light. This happens one out of every 13 scattering events and is not a significant concern for typical parameters presented here. However it represents a limit in interaction time that is independent of plasma dynamics and can lead to apparent heating. Further details are discussed in Sec. 5.3.3.

As the primary data collection device we use a Princeton Instruments PI-MAX2 intensified CCD optically coupled to the center of the plasma cloud via a series of optical relays, see Fig. 2.4. CCD pixel size is 13 µm and pixels can be binned on chip. We typically operate in a 4x4 binning mode to maximize SNR within a pixel and minimize file size while not impacting the resolution of the sensor. [95] The intensifier stage of the camera represents state of the art night vision technology and permits single photon sensitivity as well as ultrafast gatewidths ($\geq$50 ns) mediated by electronic gating with 10 ns resolution. Unfortunately this intensifier essentially limits the minimal feature size to about 40 µm, hence the 4x4 binning.

Currently the relay system is comprised of a 1 : 1 optical relay made from two f =200 mm achromatic doublets (Thorlabs PN:AC508-200-A). The optical path is bent 90° by a 2" longpass dichroic mirror which reflects blue but transmits red. The dichroic was used to avoid imaging decay fluorescence from the $^3\mathbf{P_1}$ level at 689 nm. The entire relay assembly is assembled from 2" lens tubing from Thorlabs and a tube right-angle kinematic mirror mount. Both relay lenses are installed within adjustable end tubes for easy focusing. When imaging the ions at 422 nm, a 450 nm OD 4 shortpass filter is inserted on the output of the relay to block any residual

461 nm or longer wavelength light. Ideally, wavelength selection would be managed via selection of laser line filters centered at 461 nm and 422 nm, for atom or ion imaging respectively. This would simplify the system making wavelength selection very straightforward, eliminate the chance of IR transmission through the dichroic into the imaging system (currently covered with foil), and eliminate the current contamination caused by 412 nm photoionizing photons and 355 nm UV from the Nd:YAG. This solution has only recently become available using "off the shelf" optics and would be worth pursuing.

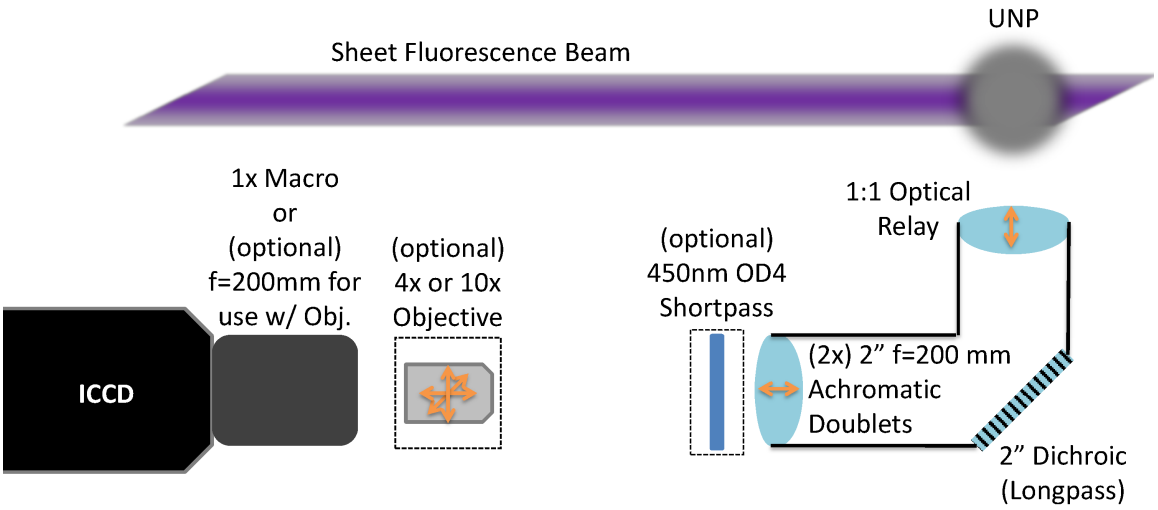

Figure 2.4 : Schematic representation of UNP imaging system (not to scale). Laser induced fluorescence is imaged into the ICCD by a 1:1 optical relay and 1X Macro lens or the 1x Macro can be replaced with a microscope objective setup for selectable 4x and 10x magnification. The orange arrows indicate focusing degrees of freedom.

The image plane of the relay is refocused onto the ICCD using a Nikon lens (Nikon 105 mm f/2.8 AF Micro) for standard 1x imaging. The Nikon lens is mounted directly to the ICCD via an F-mount adapter from Princeton Instruments.

We have also develop a magnification system to provide both 4x and 10x magnified

imaging. When imaging at higher magnification the 1x Nikon macro lens is replaced by a microscope objective (Thorlabs PN:RMS4X or RMS10X) and a zooming telephoto lens (Nikon 55-200 mm f/4-5.6G ED AF-S DX Zoom). The zoom lens is set to f=200 mm acting equivalent to a microscope's eyepiece and the choice of objective determines the magnification of the system. Data collected for this thesis was taken at 4x magnification unless otherwise noted.

Data comes in the form of raw 2D matrices of recorded intensity values, which are post processed in MATLAB to extract various plasma parameters. Experimental control is accomplished via graphical user interface built in National Instrument's Labview.

2.3 Ion Absorption Spectroscopy

Traditional absorption spectroscopy can be performed on the primary ion transition $^2\mathbf{S_{1/2}} - {}^2\mathbf{P_{1/2}}$ with resonant 422 nm laser light. [34] For this technique a collimated laser beam is projected through the plasma cloud and into the imaging system. Two images are captured, one with ions in the beam and one without, I_{ions} and I_{bkgd} respectively. Using Beer's law the ratio of the recorded intensities can be related to the OD (optical depth) of the cloud by the following relationship

$$\mathrm{OD}(x, y, \nu) = \ln[I_{bkgd}(x, y, \nu)/I_{ions}(x, y, \nu)] \tag{2.1}$$

where ν is the imaging laser frequency and the coordinate axis is set by the camera perspective, i.e. standard 2D Cartesian image with optical axis along $\hat{z}$. This is a very useful measurement since OD is related to density as follows,

$$\mathrm{OD}(x, y, \nu) = \alpha_\nu n_{areal}(x, y) \tag{2.2}$$

where $n_{areal}(x,y)$ is the areal density, i.e. $n_{areal}(x,y) \equiv \int_{-\infty}^{\infty} dz\, n_i(x,y,z)$ and α_ν is absorption crossection as a function of laser frequency. Neglecting cloud expansion, and saturation of the transition, which is negligible for laser intensities used during absorption imaging, the cross section can be written as [98]

$$\alpha_\nu = \frac{3^*\lambda_{img}^2}{2\pi} \int_{-\infty}^{\infty} d\acute{\nu}\, \frac{\gamma_0/\gamma_{eff}}{1+\left[\frac{2\pi(\nu-\acute{\nu})}{\gamma_{eff}/2}\right]^2} \otimes \frac{1}{\sqrt{2\pi}\sigma_D[T_i]} exp\left(-\frac{(\acute{\nu}-\nu_0)^2}{2\sigma_D^2[T_i]}\right). \tag{2.3}$$

3^*, called "three star", accounts for the relative alignment of the field polarization and the ions/atoms, γ_0 is the transition's natural decay rate and γ_{eff} includes the laser linewidth, i.e. $\gamma_{eff} = \gamma_0 + \gamma_{laser} = 2\pi(20.1+5.5)$MHz. The convolution over dummy variable $\acute{\nu}$ combines the Doppler broadened Gaussian distribution of velocities and the rest frame Lorentzian response of the ions. σ_D is the Doppler width velocity and depends on the local ion temperature, T_i. In our case we assume randomly oriented ions and have a linear field thus $3^* \approx 1$. Within the uncertainty afforded by absorption imaging this value appears accurate, nonetheless it could be measured directly via strong saturated absorption, e.g. see Ref. [99].

For the most robust analysis one should use a series of images to build spectra which are fit to Eqn. 2.2 with $n_{areal}(x,y)$ as a fit parameter. However, there are additional considerations regarding the ion kinetic energy that alter Eqn. 2.2, these considerations have been thoroughly studied in Refs. [34, 92] and will not be repeated here.

Alternative we can integrate over the entire spectrum and proceed with the following analysis. We integrate equation 2.2 over frequency to obtain the following,

$$\int_{-\infty}^{\infty} d\nu\, \mathrm{OD}(x,y,\nu) = \frac{3^*\gamma_0\lambda_{img}^2}{8\pi} n_{areal}(x,y). \tag{2.4}$$

Experimentally this results in images such as Fig. 2.5.

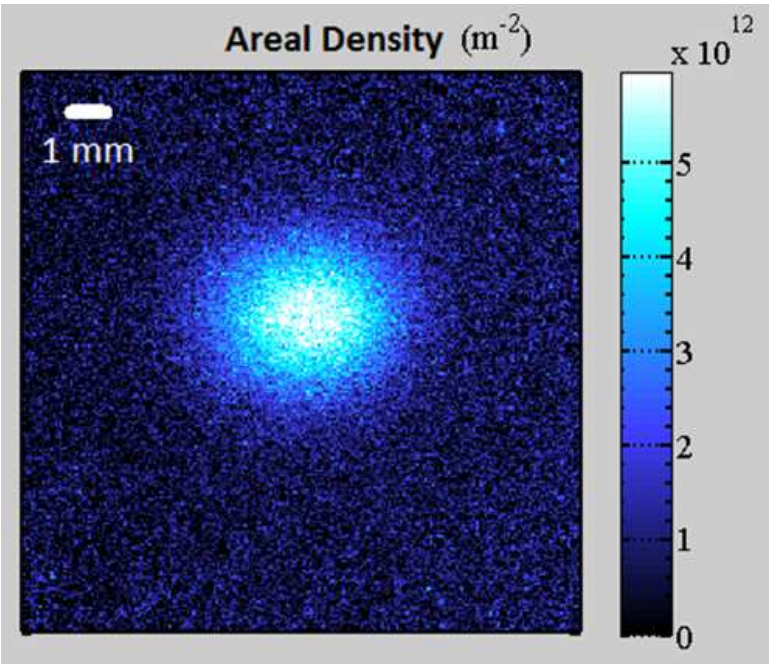

Figure 2.5 : Two dimensional image of areal ion density obtained by ion absorption spectroscopy. $\hat{x}$ and $\hat{y}$ are defined in the traditional Cartesian sense.

By integrating the areal density over the area of the entire plasma one can find total number of ions, N.

$$\int\int n_{areal}(x,y)\,dx\,dy = N \tag{2.5}$$

It's worth noting this measured number and the areal density are not subject to any assumptions regarding the size or shape of the plasma and can be considered a rather robust measurement. However, in order to relate this to a volume density one must assume a specific distribution of ion density along the camera's line of sight. Typically the cloud can be described by a three dimensional Gaussian density distribution with sizes σ_x, σ_y and σ_z. Then areal density can be converted to volume density of the

equatorial plane by the following expression,

$$n(x,y) = \frac{n_{areal}(x,y)}{\sqrt{2\pi}\sigma_z}. \tag{2.6}$$

Unfortunately our current setup can not measure σ_z, so we exploit the symmetry of the apparatus and assume it is equal to σ_y. This introduces an inevitable uncertainty in density of approximately 20%. This estimated uncertainty is based on how easily the visible dimensions (σ_x and σ_y) can be affected by alignment, up to a similar percentage.

2.3.1 Considerations

There are many aspects of this textbook treatment that must be considered when implementing the idea.

First, equation 2.1 shows that any additive background will not be removed when taking the ratio of intensities with and without atoms. To ensure absorption measurements are not effected by extraneous signal it must be subtracted from both I_{ions} and I_{bkgd} before the OD is calculated. Traditionally this has been referred to as the electronic background and provisions are available within our experimental control software to handle this easily. However it should not be thought of as just an electronic background. The electronic background is the signal present on readout even with zero exposure (e.g. with the intensifier disabled), it is about 1000 counts per pixel. However this is not the only extraneous signal. Any light that isn't the imaging beam needs to be removed from the images and should be included in what has been referred to as the electronic background. This could be ambient light or reflection of a laser other than the imaging laser or any other light source. Going forward the provisions in Labview will be renamed absorption background and it

should be recorded just before the scan is started with nothing more than the image beam blocked. Blocking the chamber window might inadvertently block non-imaging light and is not ideal. If the beam is blocked too close to the chamber scattered light could become an issue therefore it's best to block only the imaging beam several feet upbeam from the chamber.

Since images are collected and stored digitally they are discretized into pixels and therefore densities will be in pixel units, i.e. areal density is ions per square pixel. Also, integrals in space become summations of pixels. For our current system the pixel size is $12.6\,\mu\text{m} \pm 0.1\,\mu\text{m}$. This was measured by recording images of the absorption beam with a Ronchi grating inserted above and below the vacuum chamber in order to introduce intensity patterns of known spacing. The two calibration values varied little from each other.

Data are collected for a set of discrete imaging laser frequencies and therefore integrals in frequency (like Eqn. 2.4) are approximated by the trapezoidal method. It is important to probe enough frequencies (over the entire spectra, including wings) with close enough spacing that this approximation is accurate.

It is very important to control the intensity of the imaging beam. The technique relies on a constant intensity between I_{ions} and I_{bkgd} and Eqn. 2.3 assumes that the imaging beam intensity is much less than the saturation intensity. Plus the beam is shining directly into the camera and has serious potential to permanently damage the intensifier. We generally use powers of 5 mW or less (with $\approx 10\,\text{mm}$ beam radius). Gatewidths of 200 ns or less minimize plasma expansion during imaging and prevent optical pumping, which will be discussed further in sections 3.4 and section 5.3.3 respectively. Finally, gain should be SLOWLY increased from 1 in order to nearly saturate camera counts $2^6 = 65536$ for I_{bkgd}. Nearly saturating the camera ensures

we are using the full dynamic range of the sensor and maximizes the SNR

2.4 Laser Induced Fluorescence Spectroscopy

Using the primary ion transition of $^2\mathbf{S_{1/2}} - {}^2\mathbf{P_{1/2}}$ at 422 nm one can scatter photons *in situ* in order to probe plasma properties such as density and kinetic energy distributions. By spatially and temporally resolving this process one can study local plasma properties with incredible precision. In contrast to absorption spectroscopy, this technique directly measures volume density (not areal density) and benefits from higher SNR. Furthermore, with careful consideration, the kinetic energy associated with the cloud expansion can be separated from local thermal energy, providing a measure of local temperature as well as one component (coaxial with the fluorescence beam) of the local bulk velocity.

We consider a plasma centered at the origin, the imaging system still defines the coordinate system with the imaging axis along $\hat{z}$ and a fluorescence laser light beam propagates in the $-\hat{x}$ direction. The differential scattering rate of resonant light from the ions in a small volume of plasma $dxdydz$ into solid angle $d\Omega$ can be written as

$$dR_s(x, y, z, \nu, s, \Omega) = dxdydz\, n_i \frac{s}{1+s} \frac{\gamma_0}{2} f(\Omega) Conv(\nu, s, T_i, \nu^x_{exp}) \tag{2.7}$$

where n_i is the local ion density, s is the local saturation parameter (i.e. laser intensity divided by the saturation intensity, $s \equiv \frac{I}{I_{sat}}$), γ_0 is the natural linewidth, $f(\Omega)$ describes the normalized dipole radiation pattern. The final term, $Conv(s, T_i, \nu^x_{exp})$ is the convolved excitation spectrum of the ion. For ions in thermodynamic equilibrium this can be written as a Voigt profile representing the Doppler broadened and shifted

Gaussian velocity distribution convolved with both laser and ion spectra,

$$Conv(\nu, s, T_i, \nu_{exp}^x) = \int_{-\infty}^{\infty} \frac{\gamma_0/\gamma_{eff}(s)}{1 + \left(\frac{2\pi(\nu-\acute{\nu})}{\gamma_{eff}(s)/2}\right)^2} \otimes \frac{1}{\sqrt{2\pi\sigma_D^2(T_i)}} \mathbf{exp}^{-\frac{\left(\acute{\nu}-(\nu_0+\nu_{exp}^x)\right)^2}{2\sigma_D^2(T_i)}} d\acute{\nu} \quad (2.8)$$

ν is the laser frequency and ν_0 is the ion's resonance frequency, γ_0 is the natural linewidth and $\gamma_{eff}(s) = \gamma_0\sqrt{1+s} + \gamma_{laser}$ includes power broadening and the laser linewidth. The Doppler width,

$$\sigma_D(T_i) = \frac{1}{\lambda_{img}}\sqrt{\frac{k_B T_i}{m_i}} \quad (2.9)$$

depends on the local ion temperature, T_i. ν_{exp}^x is the Doppler shift due to bulk velocities along the fluorescence beam, v_{bulk}^x, they are related as

$$v_{bulk}^x = -\lambda_{img}\nu_{exp}^x. \quad (2.10)$$

For rigorous analysis we consider how this process results in the experimental data we obtain in the form of 2D matrices, i.e. intensity values from the ICCD. Of these scattered photons, how many will make it to the sensor and what will be the resulting signal? The first consideration is if the photon was emitted into the collection solid angle of the imaging system. The differential rate of photons entering our imaging system will be

$$d\tilde{R}_{SA}(x, y, z, \nu) = \int_{Collected} dR_s(x, y, z, \nu, s, \Omega) d\Omega \quad (2.11)$$

with the efficiency characterized by

$$SA \equiv \int_{Collected} f(\Omega) d\Omega. \quad (2.12)$$

In order to maximize this value the excited ion's dipole moment must be perpendicular to the imaging axis. Typical imaging with linear polarization results in the maximum

possible signal with light that is polarized parallel to the optics table (since the camera axis is perpendicular to the table). This is accomplished experimentally by tuning the polarization of the fluorescence beam for maximum signal. Circularly polarized light is used to address specific spin states in experiments not described in this thesis. In this case, the fluorescence signal is diminished.

We now consider what happens to those photons on their way to the CCD. The photon scattering rate is related to the signal in a pixel centered at (x_i, y_i), by considering multiple effects within the following expression,

$$S(x_i, y_i, \nu) \;=\; G * QE * T * \int\limits_{\tau_{cam}} \iiint\limits_{(x,y,z)} d\tilde{R}_{SA}(x, y, z, t, \nu) \otimes PSF(x, y, z, x_i, y_i) dt. \tag{2.13}$$

The first three factors represent (in)efficiencies of various stages of system, G is the photon:signal conversion factor (i.e. total electronic signal per imaged photocathode event), QE is the camera's quantum efficiency or the percentage of incident photons causing a photocathode event, T is the transmission throughput of the imaging optics. The integral in time represents the camera gating with a total exposure time calculated by $\tau_{cam} = GW * CCDs * Sums$ where GW is the camera gatewidth, $CCDs$ is the number of on CCD exposures and $Sums$ is the number of images combined in post processing. In practice we keep the camera gatewidth small enough to approximate $R_{SA}(x, y, z, t, \nu)$ as a constant, greatly simplifying the integral. $PSF(x, y, z, x_i, y_i)$ is the unit-normalized three dimensional PSF (point spread function) which represents the physical mapping of emitted photon location to corresponding image intensity distribution, i.e. it characterizes the blurring of the imaging process. Procedures taken to account for the PSF will be discussed in Sec. 5.2.2. For now we assume the PSF is a perfect mapping from the object plane to the ccd.

Thus far we have made no approximations and Eqn. 2.13 is very accurate. However to continue we will now assume a Gaussian distribution for the plasma density,

$$n_i(\mathbf{r}) = n_i(x,y,z) = n_0 e^{-\frac{x^2}{2\sigma_x^2}-\frac{y^2}{2\sigma_y^2}-\frac{z^2}{2\sigma_z^2}} \tag{2.14}$$

and a truncated Gaussian for the beam intensity,

$$I(\mathbf{r}) = I(y,z) = \begin{cases} I_0 e^{-\frac{2y^2}{w_y^2}-\frac{2z^2}{w_z^2}}, & \text{if } |z| \leq \frac{H_{slit}}{2} \\ 0, & \text{otherwise,} \end{cases} \tag{2.15}$$

σ and w are the characteristic sizes of the plasma and imaging beam respectively and the imaging beam is assumed to be centered with the plasma. Here H_{slit} is the height of a slit-like aperture on the imaging beam which limits excitation to a thin layer of plasma, thus minimizing the variance in density along the camera's line of sight. This simple restriction offers many advantages now that we can assume the plasma properties are constant within a pixel. This greatly simplifies many of the proceeding integrals and facilitates spatially resolved measurement of local plasma properties. Note, small H_{Slit} is not a strict requirement, and the following corrections hold even when the slit is large. However, plasma properties will then be averaged over the varying density.

With all of the above assumptions and integrating along $\hat{z}$, the signal can be rewritten as

$$S(x_i,y_i,\nu) = (G*QE*T*SA)\,\tau_{cam}\left(\frac{s_0}{1+s_0}e^{-\frac{2y_i^2}{w_y^2}}\right)\frac{\gamma_0}{2}\left(\sqrt{2\pi}\sigma_z n_0 e^{-\frac{x_i^2}{2\sigma_x^2}-\frac{y_i^2}{2\sigma_y^2}}\right) \left(\frac{w_z}{\sqrt{w_z^2+4\sigma_z^2}}\right) erf\left(\frac{H_{slit}\sqrt{w_z^2+4\sigma_z^2}}{2^{3/2}w_z\sigma_z}\right) Conv(s,T_i,\nu_{exp}^x). \tag{2.16}$$

with variables grouped into logical quantities. The imaging system efficiency is summarized as $C_{img} = G*QE*T*SA$, this is the colloquial "camera cal. factor". We

group $\sqrt{2\pi}\sigma_z n_0 e^{-\frac{x_i^2}{2\sigma_x^2}-\frac{y_i^2}{2\sigma_y^2}}$ which is recognized as areal density, $n_{areal}(x_i, y_i)$. $\frac{s_0}{1+s_0}e^{-\frac{2y_i^2}{w_y^2}}$ will be called I_{corr} meaning intensity correction, here $s_0 \equiv \frac{I_0}{I_{sat}}$. The term $\frac{w_z}{\sqrt{w_z^2+4\sigma_z^2}}$ is a correction to account for distribution of density and intensity along the z-axis, we'll call it's reciprocal Z_{corr}. The term $erf\left(\frac{H_{slit}\sqrt{w_z^2+4\sigma_z^2}}{2^{3/2}w_z\sigma_z}\right)$ is a correction due to the finite slit height, we'll call it's reciprocal $Slit_{corr}$. For a detailed discussion of these corrections, their typical values and evolution, see appendix B.1. This gives us

$$S(x_i, y_i, \nu) = \frac{C_{img} * \tau_{cam} * n_{areal}(x_i, y_i) * I_{corr} * Conv(x_i, y_i)}{Slit_{corr} * Z_{corr}}. \quad (2.17)$$

Which we rearrange to define our fully normalized signal $FNS(x_i, y_i, \nu)$,

$$FNS(x_i, y_i, \nu) \equiv \frac{S(x_i, y_i, \nu) * Slit_{corr} * Z_{corr}}{C_{img} * \tau_{cam} * I_{corr}} = n_{areal}(x_i, y_i) * Conv(x_i, y_i). \quad (2.18)$$

By fitting our signal to Eqn. 2.18 we obtain measurements of the local ion temperature, the spectra's center frequency and the local ion density. Typical results for the center of the plasma are shown in Fig. 2.6. Uncertainties are 95% confidence intervals calculated by the fitting routine.

Key to the performance of any fitting routine is initialization with proper guesses for fitting parameters. To this end adaptive guessing algorithms were implemented where on subsequent re-analysis of datasets, prior analysis results are passed along to assist in predicting each spectra. The details of such are discussed in Appendix A.2. As shown in Figs. 2.6, 2.8, and 2.9 the resulting guesses are very close to the final fit functions over a fairly wide range of parameters.

2.4.1 Density Calibration

One of the most critical aspects of collecting precise fluorescence data is calibrating the signal to true ion density. Ultimately one must supply a value for C_{img} which

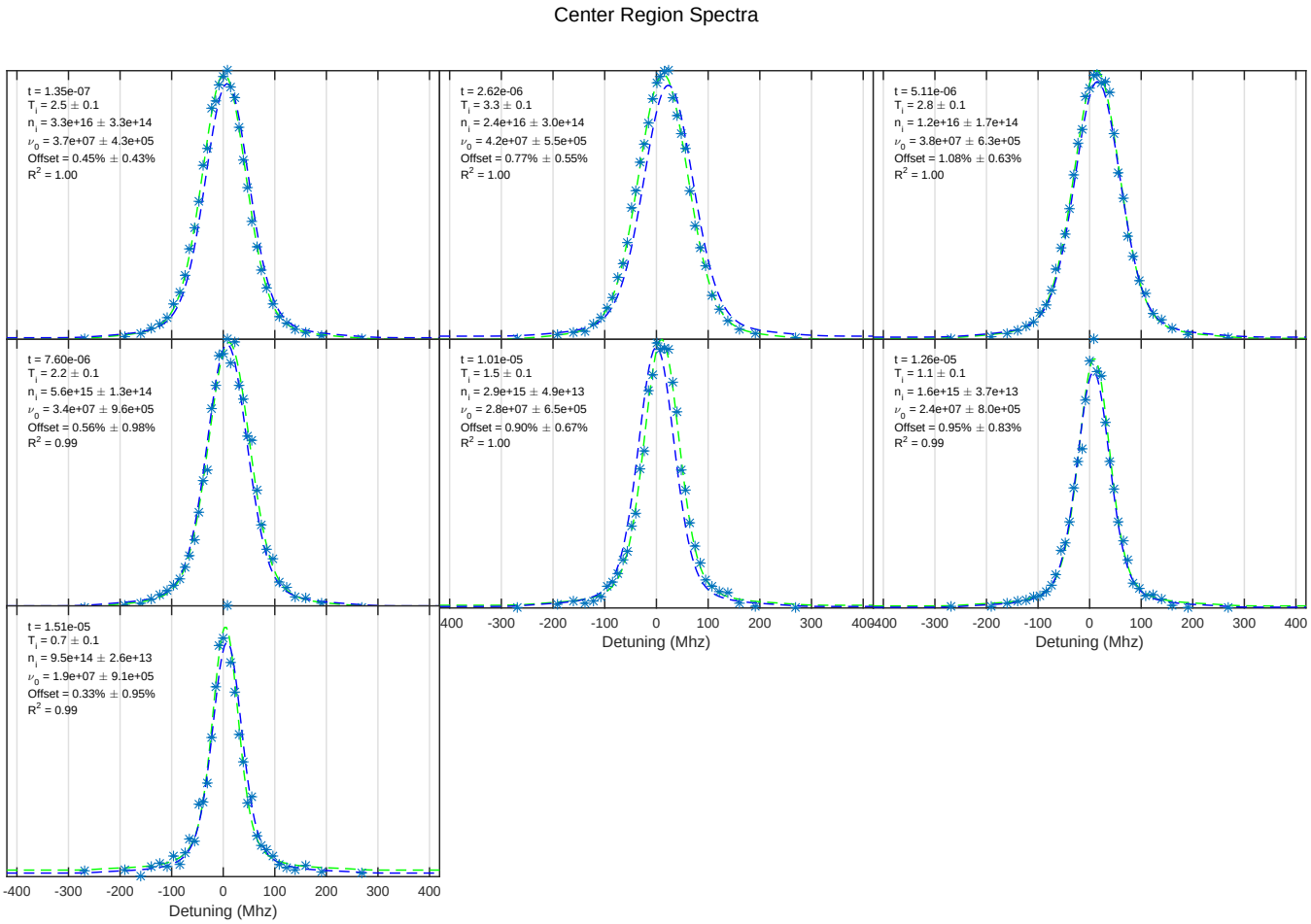

Figure 2.6 : Typical spectrum evolution obtained by ion fluorescence spectroscopy for the center of a UNP. Fitting each spectra to a Voigt profile provides a measure of ion temperature, density and center frequency (green dashed lines). The results of the fit parameters as well as the plasma expansion time are shown in each legend. Blue dashed lines showing adaptive guesses which result in faster re-analysis times and helps ensure proper fitting over a wide range of UNP parameters. Notice the difference in spectral widths between 3.3 K (middle top) and 0.9 K (bottom left), reflecting the cooling of the ions.

scales the measured density. Historically this was accomplished by comparison against ion absorption data but this technique has many potential pitfalls. First off the physical changes involved experimentally to switch between the two imaging modes

can often unlock a laser and effect the plasma significantly, obscuring the comparison. Furthermore ion absorption is inherently blind along the camera's line of sight, while the fluorescence technique is tailored (at least for these studies) to isolate a thin layer of plasma. At some point, an assumption on the density distribution must enter and we do not have imaging capabilities along this axis, therefore significant uncertainty is innate and on the order of 20 %. In section 4.1 we will discuss alternative methods of density calibration which are experimentally easier to conduct and more accurate.

2.4.2 Regional Analysis

The previous discussion considers analyzing the signal in each pixel independently however typical SNRs are insufficient for analyzing single pixels and so we employ what we call regional analysis. In essence, signal from a small region of roughly constant plasma parameters is collected and analyzed. Regional signal is collected by means of 2D spatial filter using a Guassian kernel 3 pixels wide and 1 mm tall with $\sigma_{Guass} = 1\,\text{mm}$. After filtering, a plasma-centered horizontal strip of regions 1 mm wide (representing 85 regions at 4x magnification) is analyzed, each region independently. These regions of analysis are depicted in Fig. 2.7. Figure 2.8 shows results of spectral fits for a region 0.5 mm left of plasma center, i.e. Region #1.

The regional ion temperatures and densities can be studied independently or can be averaged for greater SNR. We use a robust average as to avoid effects from the occasional bad spectral fit, i.e. ignoring fit results from any region which deviate more than six standard deviations as compared to all regions. It is this robust average of regional parameters that is presented as parameter evolution throughout this thesis. Error bars on the averaged values represent the robust standard deviation of the mean, again neglecting extreme outliers. This technique utilizes all the signal in a

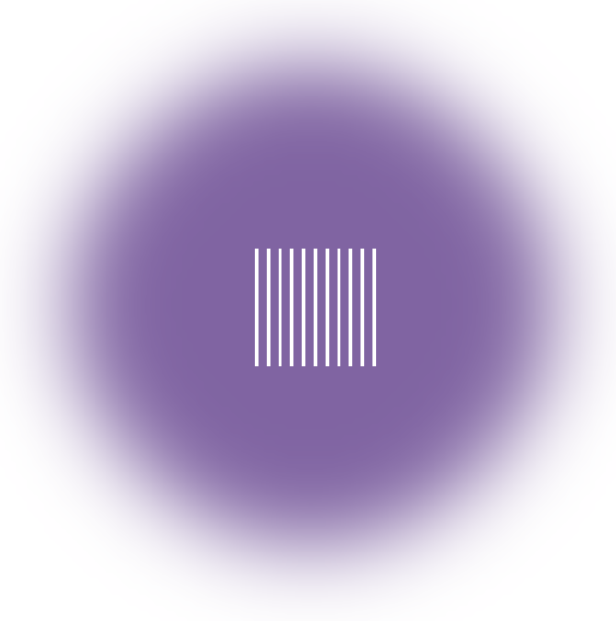

Figure 2.7 : Cartoon depicting geometry of regions (vertical white strips) for regional analysis of UNPs at 4x magnification, relative size of regions and plasma is to scale, however there are typically 85 regions within the 1 mm^2. Since the regional filter is 3 pixels wide, each region overlaps one column of pixels with each of it's neighbors. The regions are numbered left to right.

super-region 1 mm by 1 mm while still analyzing narrow regions independently as necessary to avoid apparent heating of the ions, which results from the spread of bulk velocities within a region. This potential pitfall will be discussed in detail in Sec. 5.2.1. Typical detailed results of regional analysis are shown in Fig. 2.10 and Fig. 2.11.

2.4.3 Full 2D Analysis

Taking regional analysis to the next level we can analyze the entire field of view via smaller regional filters (3 pixels wide by 10 pixels tall) and construct a 2-dimensional

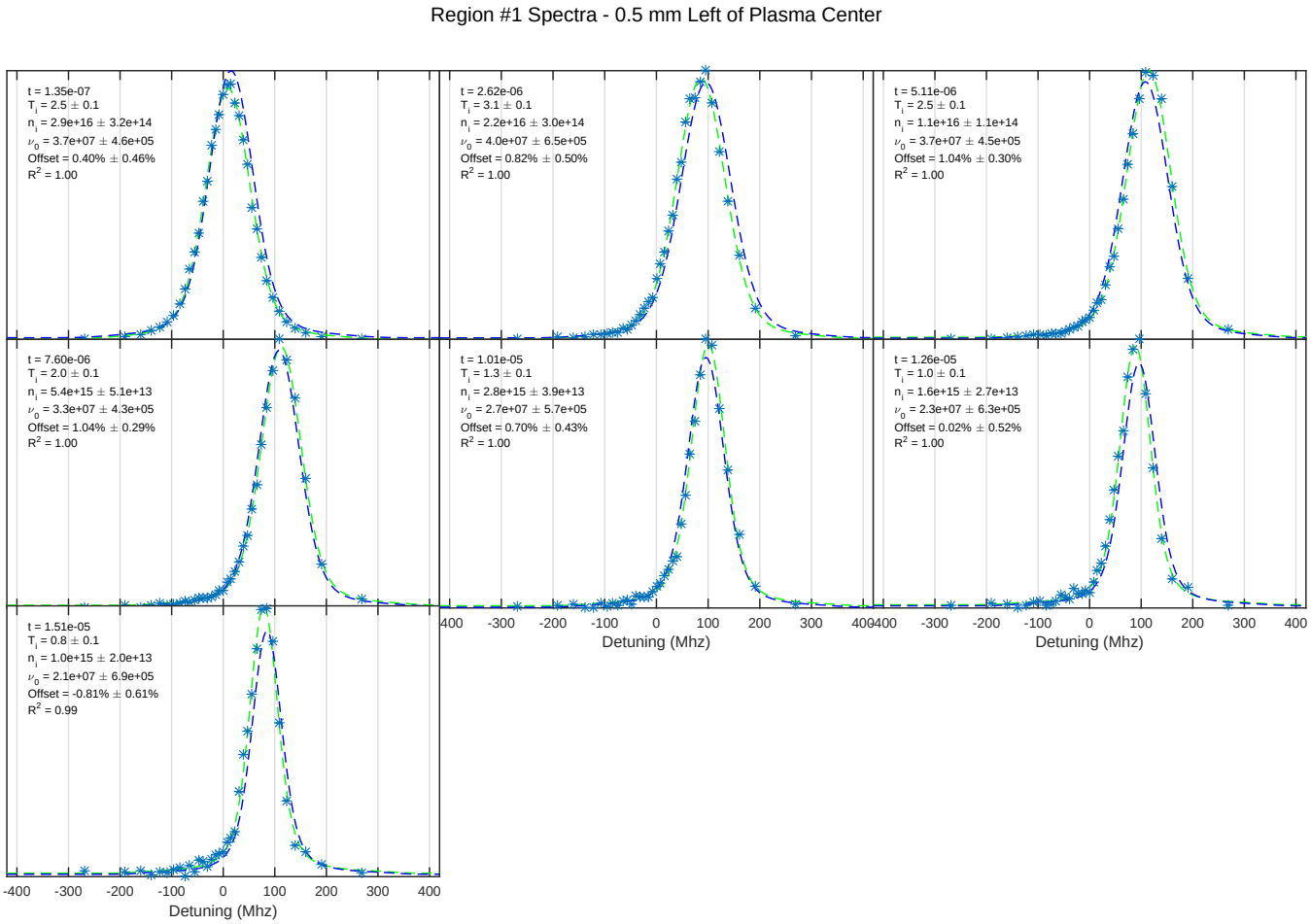

Figure 2.8 : Typical spectrum evolution obtained by ion fluorescence spectroscopy for a region 0.5 mm to the left of plasma center. Notice the evolution of the center frequency, which is negatively proportional to the $\hat{x}$-component of the bulk velocity within the region. This clearly shows the movement of ions to the left, i.e. away from plasma center. The uneven spacing of detunings was intentional in order to improve fit performance of centered spectra, however we see it is not ideal for off-centered spectra. The degree of irregularity has since been reduced.

map of ion temperature, local density and bulk velocity. The results are shown in Fig. 2.12 and represent over 600,000 spectra fits which were completed in about an hour. The example shows a UNP created with a sharp void that results in interesting dynamics in all three parameters, ion density, ion temperature and local spectra shifts

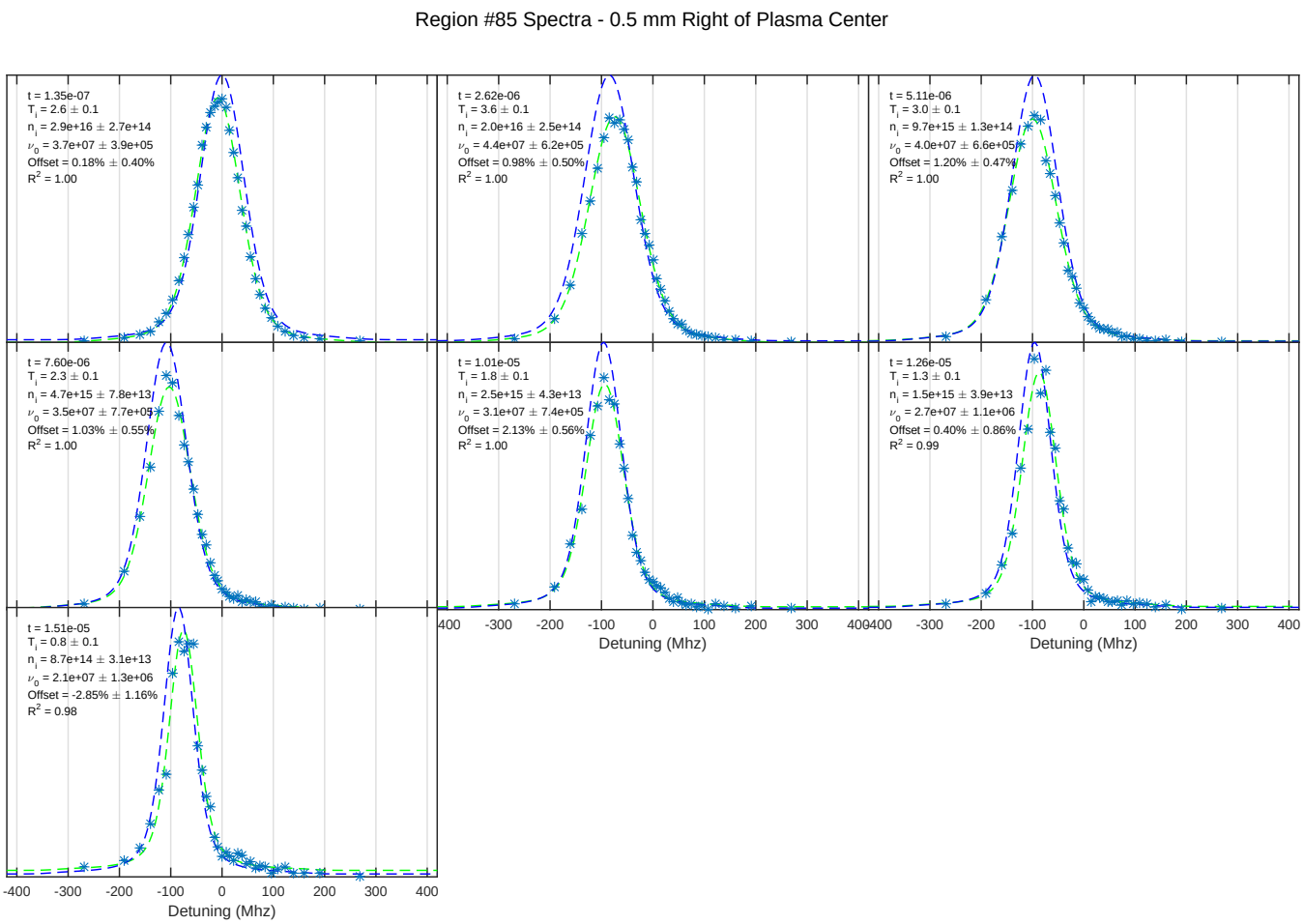

Figure 2.9 : Same as 2.8 except for a region 0.5 mm to the right of plasma center. Notice the down-shifted center frequencies reflecting the right going bulk velocities.

(representing local bulk velocities). The example clearly shows how density features can heat the plasma and disrupt the typical plasma dynamics.

The extension of this technique into making movies of plasma parameter evolution is straight-forward via MATLAB's built-in getframe function. Thus representing a new and exciting tool for multimedia presentation of real experimental results.

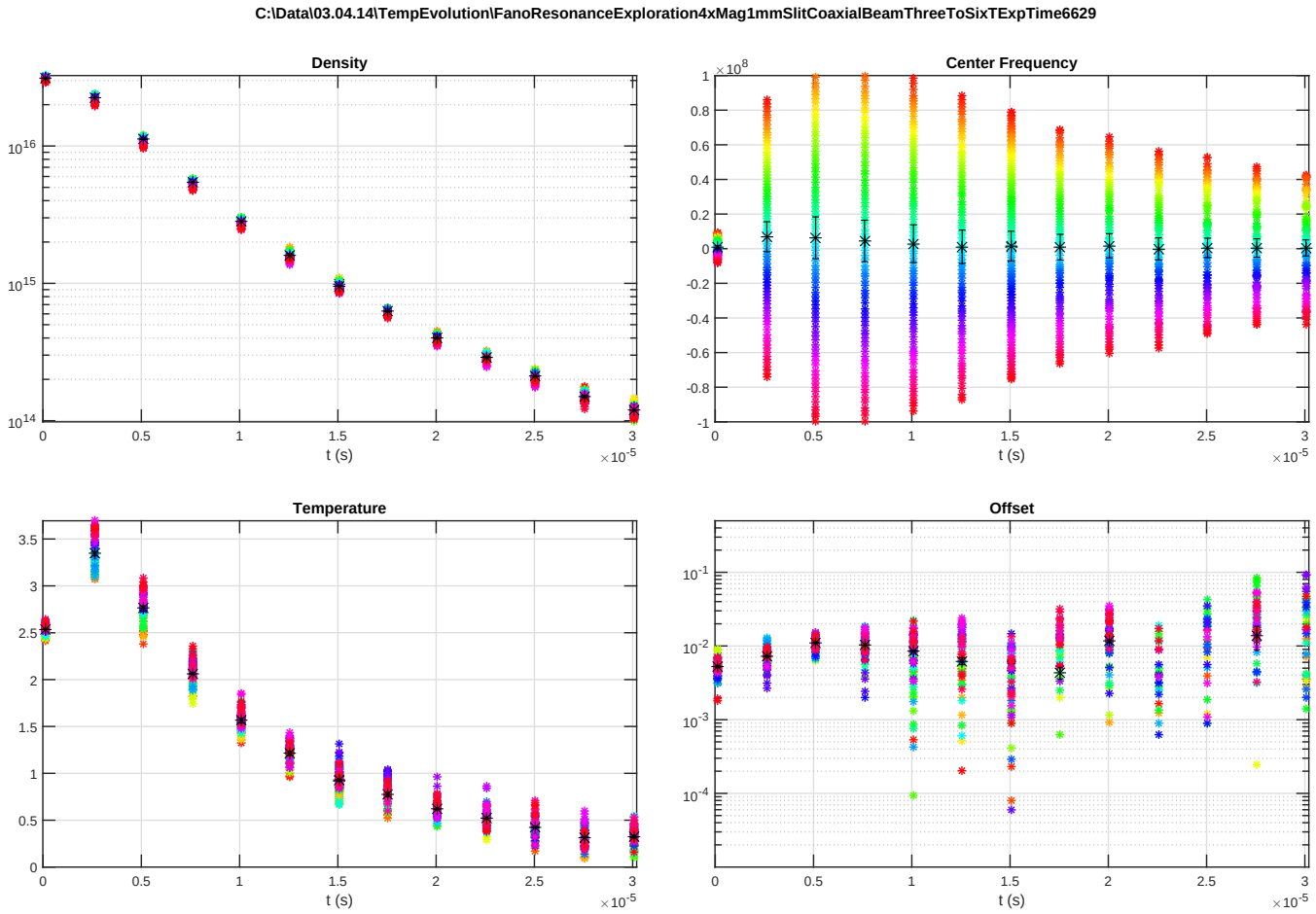

Figure 2.10 : Regional analysis of a UNP with $T_e(0) = 430\,\mathrm{K}$ and $\sigma_0 = 1\,\mathrm{mm}$. Results are plotted versus time and thus display the evolution of ion fluorescence spectra fit parameters. Color reflects the plasma region number which from left to right, goes from red through purple. Each region is 12.6 µm wide. Black markers indicate robust averages taken at each time point. These are the values displayed throughout this thesis. Notice how both the density and temperature decrease as the time evolves and the plasma expands. Center frequencies are negatively proportional to the $\hat{x}$-component of the ion's bulk velocity and their behavior displays the expansion dynamics. Offset is an extra fit parameter to account for any additive offset on the spectra. It is plotted relative to the signal peak.

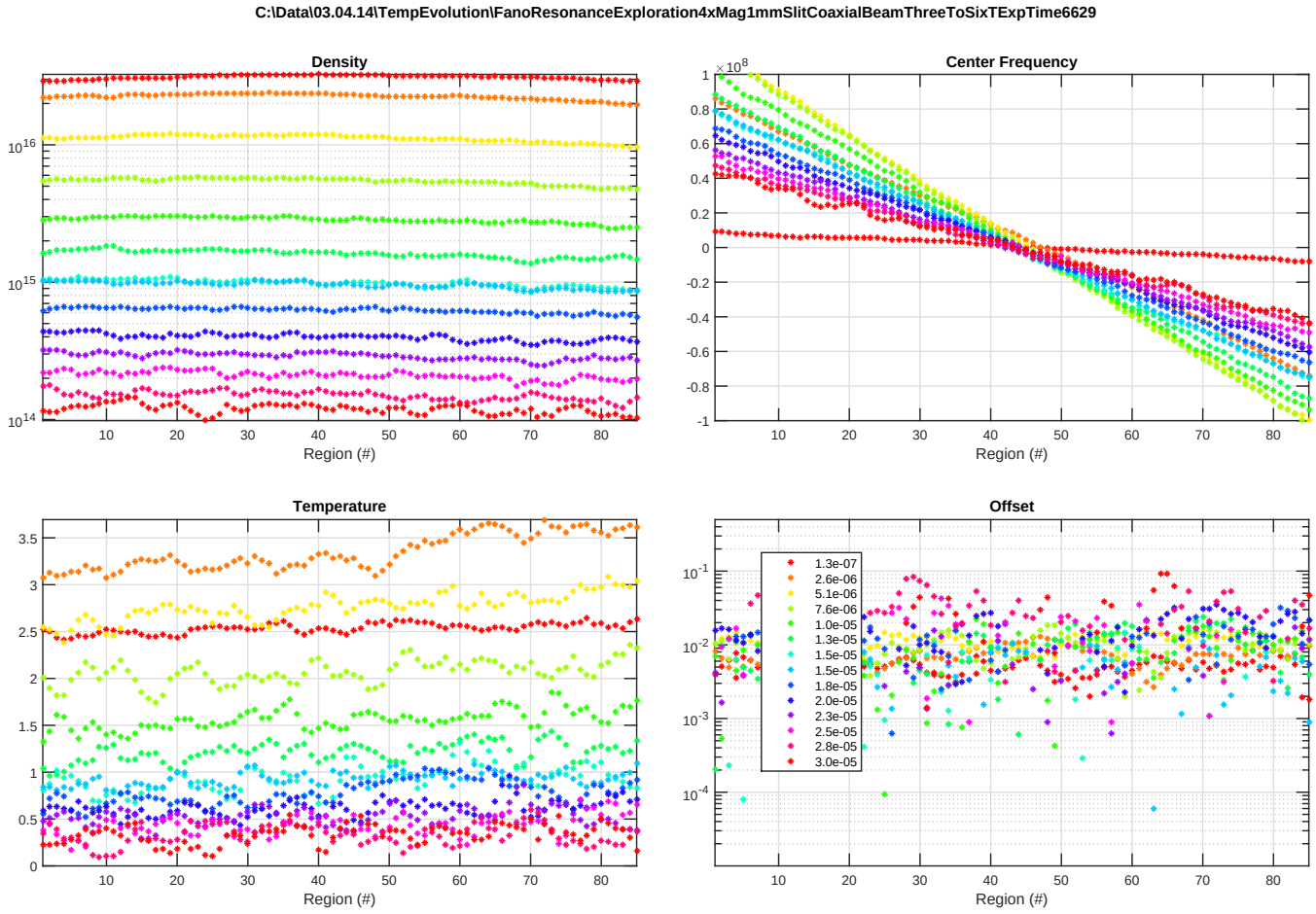

Figure 2.11 : Regional analysis of a UNP with $T_e(0) = 430\,\mathrm{K}$ and $\sigma_0 = 1\,\mathrm{mm}$. Results are plotted versus region number and thus represent a 1D cut (along $\hat{x}$) through the center of the plasma, $\pm\,0.5\,\mathrm{mm}$ from center. Color reflects the plasma evolution time, t, as displayed in the legend. From this perspective we can see features within both the density and temperature profiles. The center frequency plot clearly shows the bulk velocity's linear dependence on x

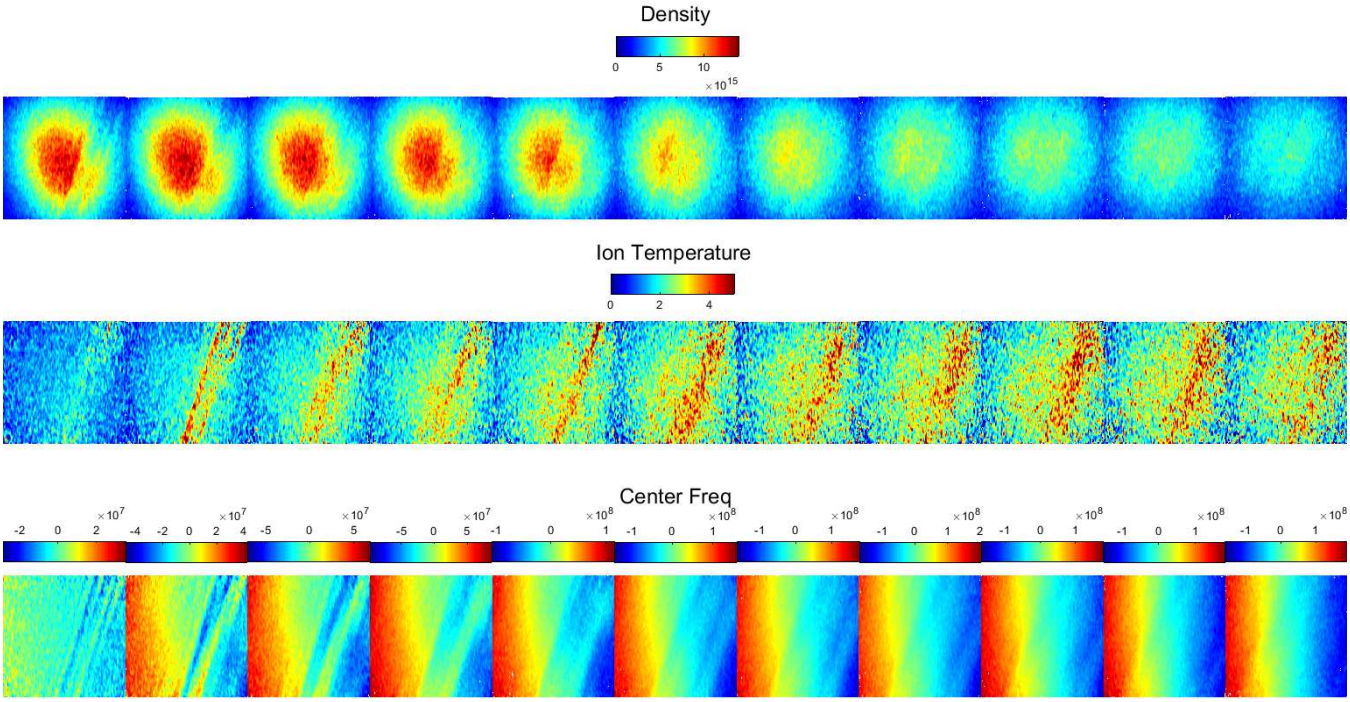

Figure 2.12 : Small region analysis of the entire field of view results in high resolution 2D maps of ion temperature, density and center frequencies. Here time passes from left to right.

2.5 Frequency Calibration

Because our diagnostic is a spectroscopic measurement, it is imperative we know our image beam frequency, ν, with sufficient accuracy. This is accomplished by locking the imaging laser frequency to a stabilized Fabry-Perot transfer cavity. Only 440 MHz from the 422 nm imaging transition one finds two well-known spectral lines in ^{85}Rb. [100, 101] Saturated absorption spectroscopy is performed in a Rb vapor cell and the resulting spectrum, as shown in Fig. 2.13, is fit to the following model,

$$f(V) = A_p(V - V_p)^2 + \frac{A_1}{1 + (\frac{V - V_l + 2V_{sp}}{\Gamma})^2} + \frac{A_2}{1 + (\frac{V - V_l + V_{sp}}{\Gamma})^2} + \frac{A_3}{1 + (\frac{V - V_l}{\Gamma})^2}, \quad (2.19)$$

where V is the output voltage used to control the length of the Fabry-Perot cavity (via a low voltage piezo-electro transducer). The first term represents the Doppler broadened absorption bowl, i.e. a parabola of amplitude A_p with center voltage V_p. The other three terms represent the three Lamb dips (two resonances and one crossover), which are fit to Lorentzian distributions of varying amplitudes, $A_{1,2,3}$, with periodic spacing V_{sp} and similar widths, Γ. Previously each peak had an independent linewidth and the spacing was not forced to be uniform which resulted in three redundant fit parameters and poor fit performance.

We assume the cavity has a linear response and calculate a voltage to detuning conversion factor by comparing V_{sp} to the known value of 58.7 MHz, [102] i.e. $C_{det} \equiv 58.7\,\text{MHz}/V_{sp}$. The typical value of C_{det} is $77\,\text{MHz}\,\text{V}^{-1} \pm 1\,\text{MHz}\,\text{V}^{-1}$. The location of the right peak, V_l, is now an absolute reference for the $^{88}\text{Sr}^+$ resonance frequency only 440 MHz to the blue. This offset is experimentally accomplished by double passing a 220 MHz AOM in a cat's eyes configuration directly before the sat. abs. setup. We also use this fit to measure our imaging laser linewidth, i.e. $\gamma_{laser} \equiv C_{det}\Gamma$ since the natural linewidth of the transition is negligible. Typically $\gamma_{laser} \approx 5.5\,\text{MHz} \pm$

0.5 MHz.

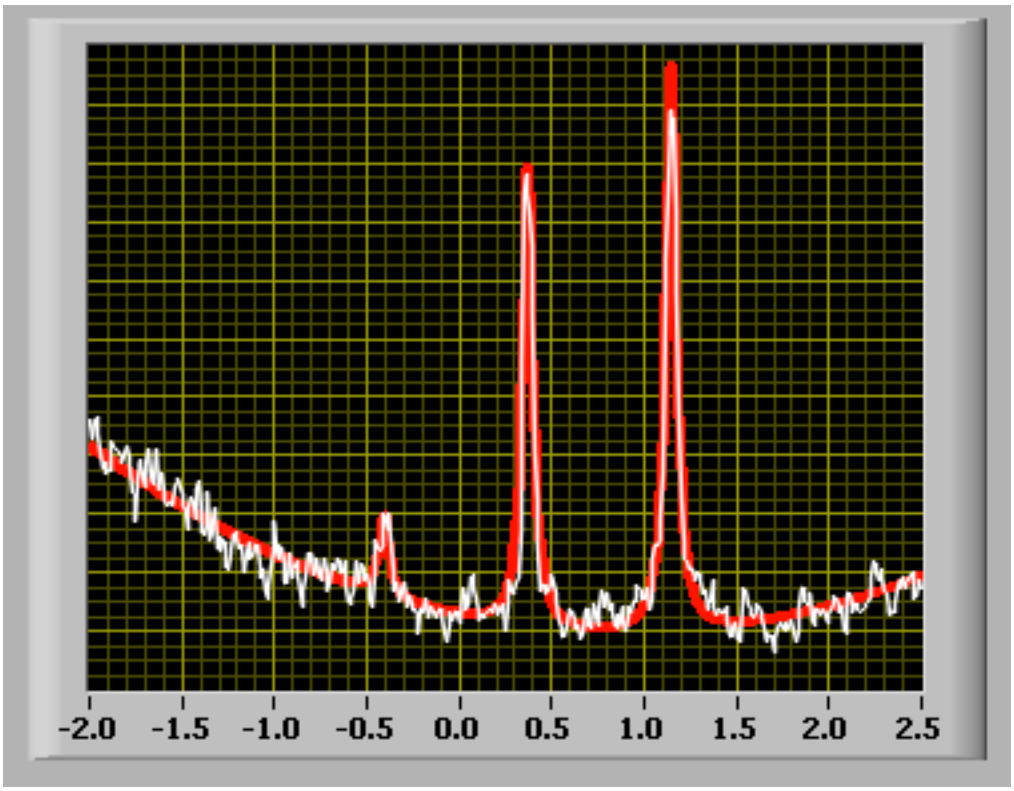

Figure 2.13 : Saturated absorption signal from Rb scan (white) with fit to a triple Lamb dip model, i.e. Eqn. 2.19 (red) plotted versus control voltage, V, allows for calibration of control voltage to imaging beam detuning as well as determination of imaging laser linewidth.

From this information we can now calculate our imaging laser detuning referenced to the ion's primary transition by the following expression, $\nu = C_{det} * (V - V_0)$, where V is the set point voltage from Labview controlling the frequency of the 422 nm laser and V_0 is voltage expected to put the laser on the $^{88}Sr^{+}$ resonance, i.e. $V_0 = V_l + \frac{440\,\mathrm{MHz}}{C_{det}}$.

The assumption of a linear cavity response was reasonable and seemingly accurate based on the goodness of fits to RB scans and the lack of confounding factors however it remained an open uncertainty. To settle this, Trevor Strickler developed a beat note system to characterize the cavity's response. A second 422 nm laser was actively

locked to the rightmost Rb peaks while the imaging laser was scanned using the Fabry-Perot offset voltage, V. Expected detuning was compared to measured detuning using a high bandwidth beat note detection system on the two lasers. The agreement between the beat note measurement and the linear conversion are good to within 1% and therefore do not represent a significant uncertainty in our measurements of density or temperature.

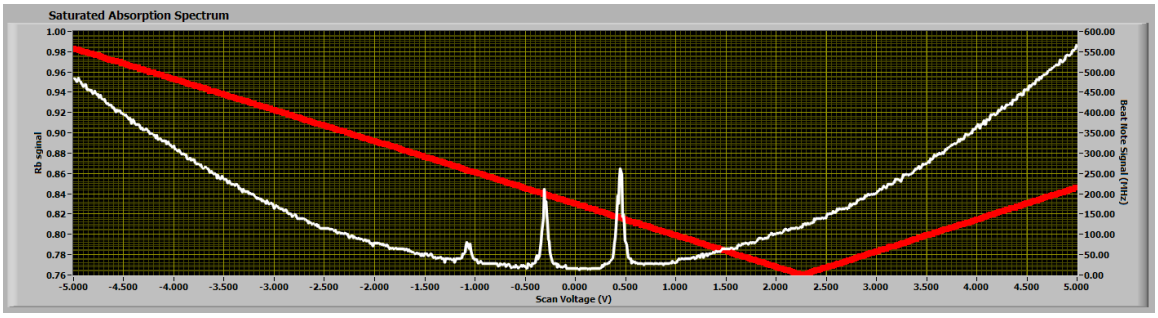

Figure 2.14 : Rb saturated absorption signal (white-left y-axis) including beat note measurement (red-right y-axis) shows highly linear response to imaging beam frequency control voltage, V (x-axis).

Chapter 3

Ultracold Neutral Plasma Dynamics

3.1 Introduction

Ultracold neutral plasma dynamics are complex, interesting and governed by many competing mechanisms, some that cool and others that heat. Energy is continuously transferred between potential and kinetic degrees of freedom, the first of which is an important energy scale by virtue of the plasma being strongly coupled. Also, energy is exchanged by elastic collisions of like and unlike species. Isolated from their environment and ultraclean, UNPs provide an ideal test bed to study these processes.

However study of these phenomena at later times is complicated by the fast expansion of the plasma cloud, which is easily misinterpreted. This thesis details the techniques that alleviate this complication and shows both adiabatic cooling of the ions and electron ion energy transfer for the first time in a ultracold neutral plasma.

3.2 Initial Temperatures

To understand the evolution of something one must start at the beginning, i.e. t_0, the moment of plasma ionization. Initially the liberated electrons are given a small surplus of kinetic energy, the difference between the photon energy and the ionization potential, i.e. $\Delta E_0 = \hbar(\omega_{I1} + \omega_{I2}) - E_{ion}$. This excess energy equilibrates to a global temperature set by the following relation, $3k_B T_e(0)/2 = \Delta E_0$ within the first few plasma oscillation periods, i.e. $\omega_{pe}^{-1} = \sqrt{\frac{m_e \varepsilon_0}{ne^2}}$ ~10 ns. [103, 36] Typical values of ω_{pe}

are given in Fig.3.1 and typical values for $T_e(t = 0)$ are selected between 20 K and 450 K with $\pm$ 5 % uncertainty.

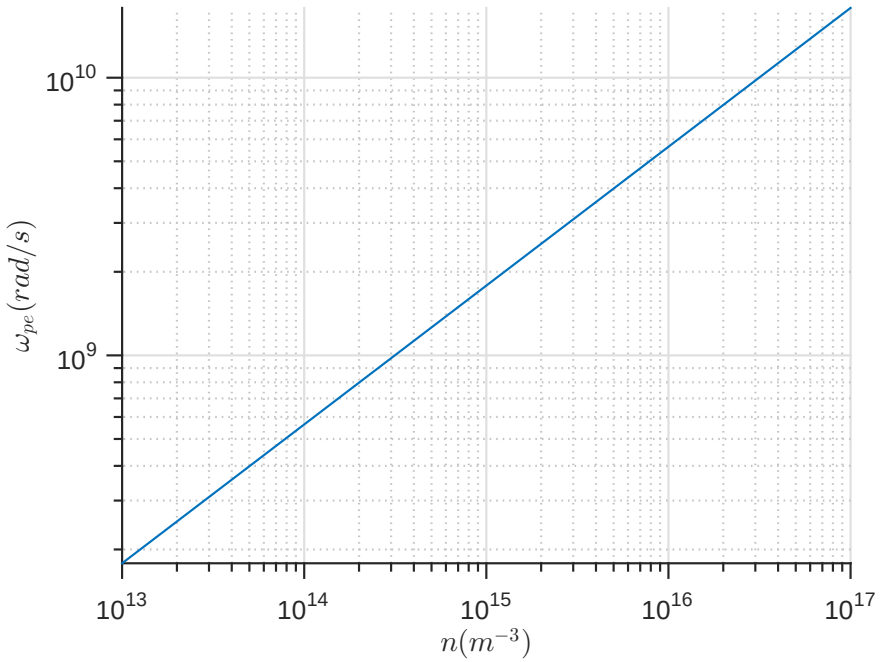

Figure 3.1 : Typical values of ω_{pe}.

On a similar time scale, ω_{pe}^{-1}, some of the electrons will escape the plasma volume and create a space charge that will confine the remaining electrons. This typically results in a nonnuetrality of a few percent or less and is rather insignificant to overall dynamics, for our conditions. [104] However, if densities are low enough (less than $1 \times 10^{14}\,\mathrm{m}^{-3}$) then this electron evaporation can lead to enhanced cooling and modified expansion dynamics. [105]

Meanwhile (by virtue of the tiny electron:ion mass ratio) the ion's kinetic energy is practically undisturbed by the ionization process and they inherit their initial temperature from the laser cooled atoms, $\approx 7\,\mathrm{mK}$ at t_0 [19]. These ultracold temperatures

would lead to a naive calculation of $\Gamma_i(t=0) > 500$! However, the plasma is far from equilibrium and the ions will quickly be heated by equilibrium-seeking processes.

3.3 Non-Equilibrium Ions Dynamics

The initial stages of plasma evolution are driven by the pursuit of thermodynamic equilibrium, which ultimately heats the ions and limits the initial coupling parameter. These fascinating non-equilibrium processes have been studied thoroughly both experimentally [34, 35, 25, 106, 65, 92, 107, 108, 3] and theoretically [48, 53, 38, 103, 109, 110, 111], with recent efforts to understand the effects of electron shielding [108, 112] so here we will only discuss the main points.

3.3.1 Disorder Induced Heating

Although ions in UNP are created at extremely cold temperatures, they are quickly heated by a couple orders of magnitude during what is known as disorder induced heating (DIH), or in more general terms, correlation heating. [110] This is due to the fact that the ions are created with random spatial distribution, which results in some ions that are closer together than average and strong repulsive forces. The ions are accelerated, converting correlation energy (U_{ii}) into kinetic energy and heating to $\sim 1\,\mathrm{K}$, on a time scale of $\omega_{pi}^{-1} = \sqrt{\frac{m_i \varepsilon_0}{ne^2}}$ $\sim$200 ns. Typical values for ω_{pi} are given in Fig. 3.2. Unfortunately disorder induced heating limits Γ_i for UNPs created from randomly distributed atoms and sets the intial equilibrium value of Γ_i to about 2. [113, 114] When we measure T_i at short times immediately after plasma creation we see evolutions like those in figure 3.3. Notice how ion temperatures quickly heat to temperatures on the order of 1 K to 2 K.

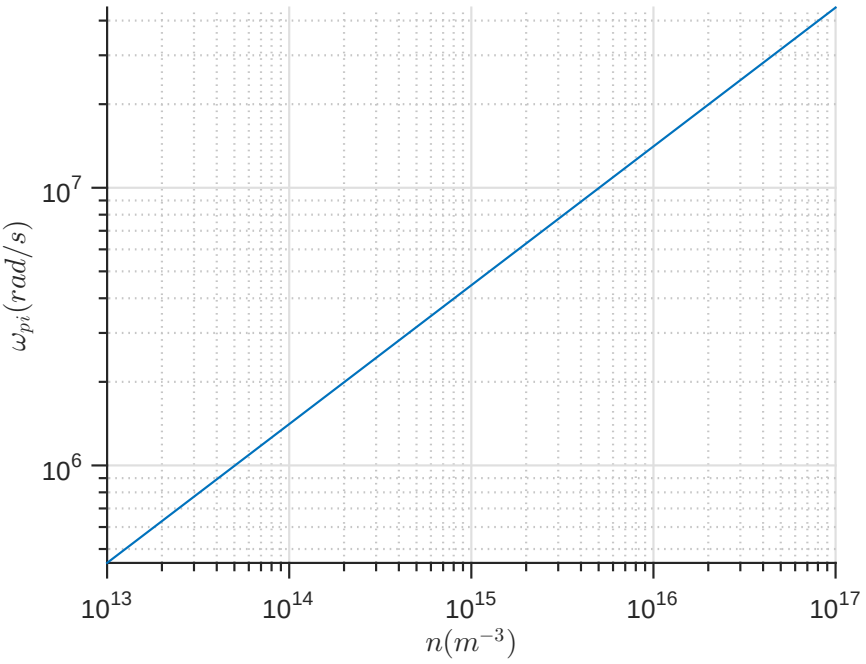

Figure 3.2 : Typical values of ω_{pi} for UNP of ^{88}Sr.

3.3.2 Kinetic Energy Oscillations

One immediately notices that not only do the ions heat up drastically but they then oscillate in kinetic energy. This is because the individual ions will overshoot their potential energy minimum and oscillate, before being damped within a few cycles. This is known as kinetic energy oscillations (KEO) [93] and their frequency is roughly twice ω_{pi}.

3.3.3 DIH Magnitude

Precise calculation of DIH temperatures is imperative to modelling the ensuing ion dynamics and over the years several techniques have been developed. Initially, there is no kinetic energy, but lots of potential; in equilibrium, there is equal kinetic and

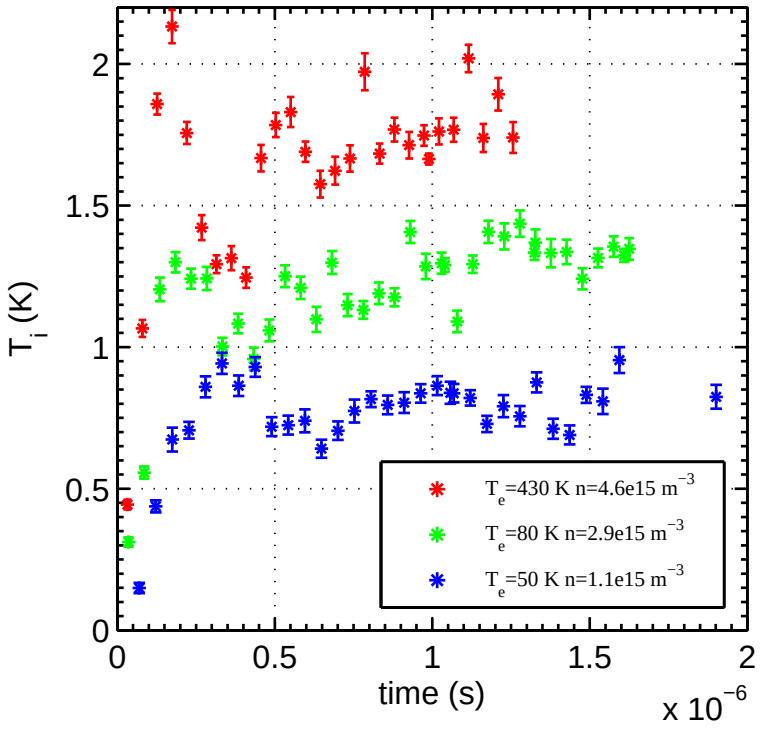

Figure 3.3 : Early time ion temperatures show disorder induced heating and kinetic energy oscillations. Notice the dependence on density in both the magnitude of temperatures as well as the time scale for oscillations.

potential. Hence the problem reduces to finding the difference in potential energy between the two well-defined states: initial total disorder, and final equilibrium at a given density.

Formally, the initially disordered state, with no spatial correlations, is defined as having potential energy equal to zero. The potential energy in the equilibrium state is then negative and equal to a quantity $U_{ii,eq}$, which is the excess potential energy per ion due to correlations at equilibrium for a given density. With careful treatment of correlations and electron screening the equilibrium correlation energy can be written

as, [41]

$$U_{ii,eq}(\kappa,\Gamma) = \frac{e^2}{4\pi\varepsilon_0 a_{ws}}\left[\frac{u}{\Gamma}+\frac{\kappa}{2}\right]. \tag{3.1}$$

Here, u/Γ is a function of the equilibrium Γ and it is often tabulated from molecular dynamics results. [4, 115, 116, 117, 118] We use the results from Ref. [116],

$$u/\Gamma = \left[a(\kappa)\Gamma + b(\kappa)\Gamma^{1/3} + c(\kappa) + d(\kappa)\Gamma^{-1/3}\right]/\Gamma, \tag{3.2}$$

where the fit parameters $a, b, c,$ and d are functions of κ. From the context of Yukawa theory,

$$\kappa = \frac{a_{ws}}{\lambda_D}. \tag{3.3}$$

is the inverse scaled electron screening length, or the average interparticle spacing scaled by the inverse of the Debye shielding length, [3]

$$\lambda_D \equiv \sqrt{\frac{\varepsilon_0 k_B T_e}{e^2 n}}, \tag{3.4}$$

see Fig. 3.4, Fig. 3.5 and Fig. 3.6 for typical values of κ, a_{ws} and λ_D, respectively.

For an otherwise non-changing plasma the conversion of potential energy results in an equilibrium temperature equal to, [41, 111]

$$T_{DIH} \equiv \frac{-2}{3k_b} U_{ii_{eq}}. \tag{3.5}$$

Figure 3.7 shows this value (T_{DIH}) plotted as a function of electron temperature and density. It is found that the DIH temperature depends mainly on density, i.e. $T_{DIH} \propto n_i^{1/3}$ and secondarily on the presence of electron shielding. The latter can lower the DIH temperature due to a softening of the inter-particle potential, unfortunately this was found to have little impact on the resulting Γ_i since the ratio of potential to kinetic energy doesn't change. [108] We can calculate equilibrium values for Γ_i and see that DIH practically sets the initial ion coupling to 2.5 , to 3 , as shown in Fig. 3.8. .

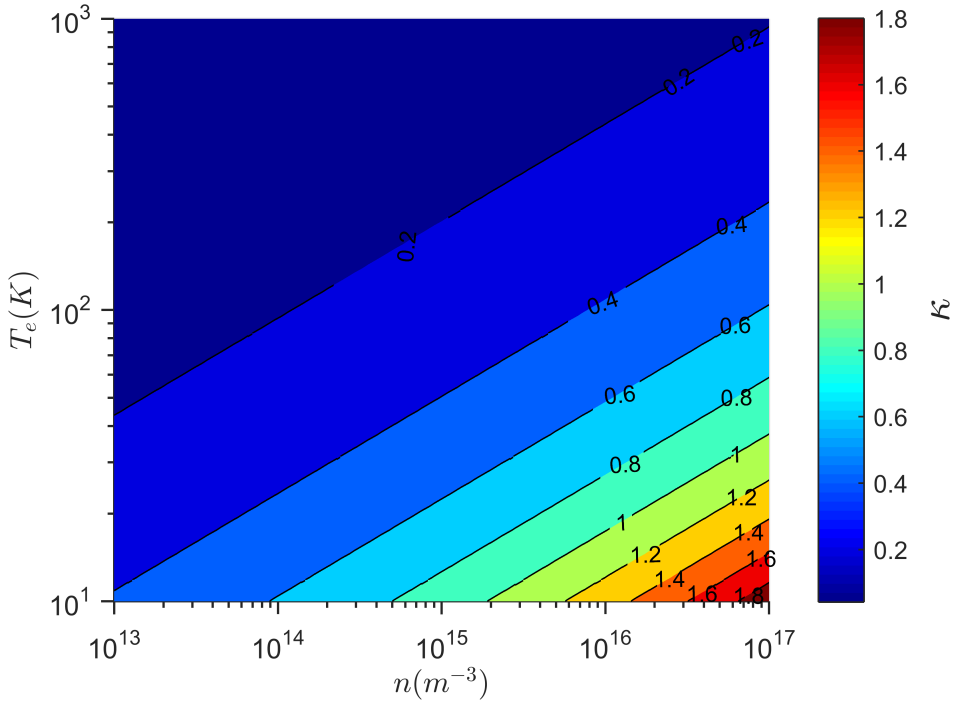

Figure 3.4 : Typical values of κ plotted versus T_e and n, calculated from Eqn. 3.3.

3.3.4 DIH Time Scale

The time between plasma creation and the first peak in ion temperature, which we will call τ_{DIH}, is set by the characteristic time scale for ion motion, i.e. the ion plasma oscillation frequency. [34, 35] For a neutral, singly ionized plasma that frequency is,

$$\omega_{pi} = \sqrt{\frac{ne^2}{m_i \varepsilon_0}}. \tag{3.6}$$

Realizing that the first peak is only one quarter of an ion oscillation,

$$\tau_{DIH} \equiv \frac{2\pi}{4\omega_{pi}}. \tag{3.7}$$

However, in regimes where electron shielding is significant τ_{DIH}, was found to be reduced. This makes sense since the inter-particle potentials will be softened. A phenomenological fit to experimental and simulation data by Bergeson et.al. yields

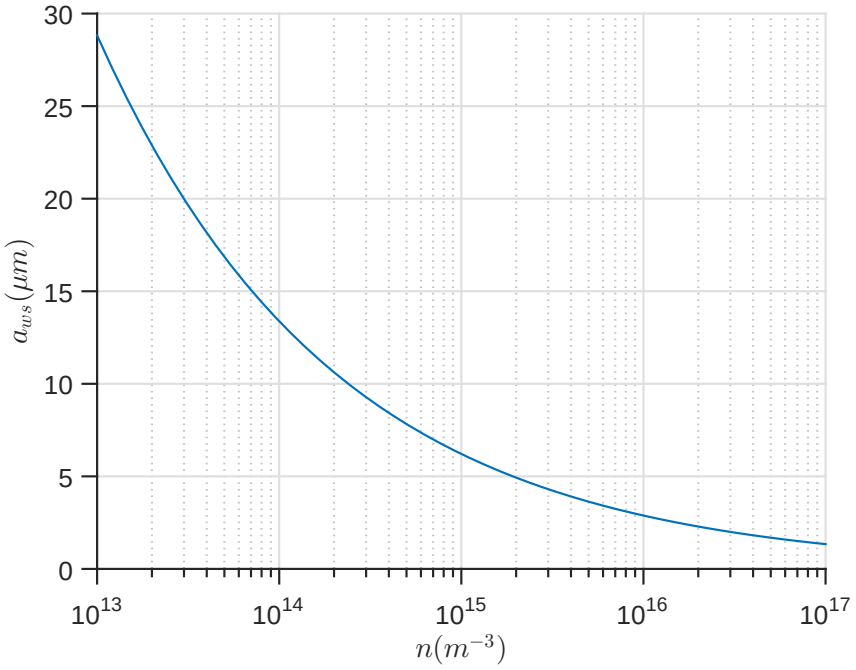

Figure 3.5 : Typical values of a_{ws} plotted versus n.

the following expression for the shielded DIH time, which is valid when $0.3 < \kappa < 1$, [3]

$$\tilde{\tau}_{DIH} = \frac{1.445 + 0.467\kappa(0)}{\omega_{pi}(0)}. \tag{3.8}$$

3.3.5 Scaled KEOs

Scaling kinetic energy oscillations by the aforementioned energy and time scales should result in universal behavior, in absence of electron screening. This is seen experimentally as in Figure 3.9. The measurements overshoot the equilibrium value on the first peak then oscillate below the equilibrium value until equilibrium has been reached. Note, measurements do not oscillate about the equilibrium value and the oscillation frequency is also very close to $2\omega_{pi}$.

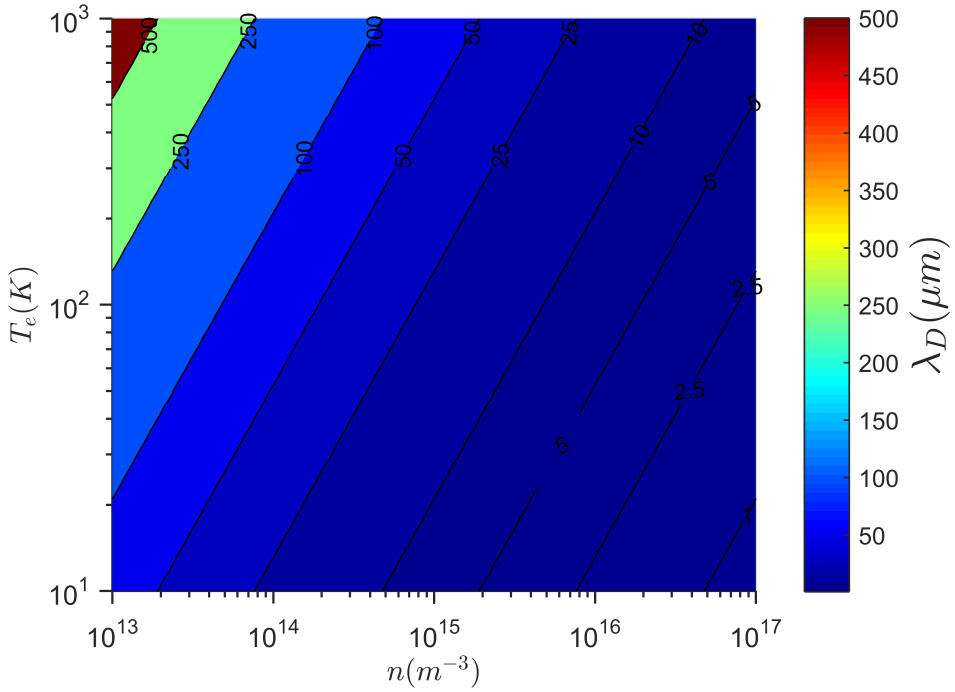

Figure 3.6 : Typical values for λ_D plotted versus T_e and n, calculated from Eqn. 3.4.

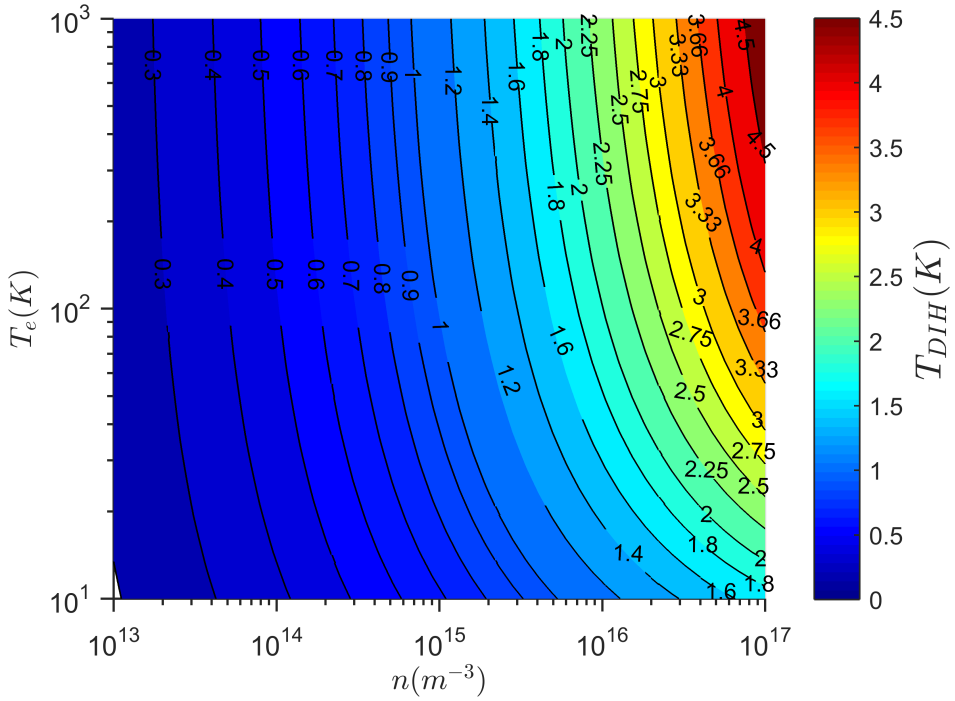

Figure 3.7 : Calculated DIH equilibration temperatures from MD simulations of Yukawa systems

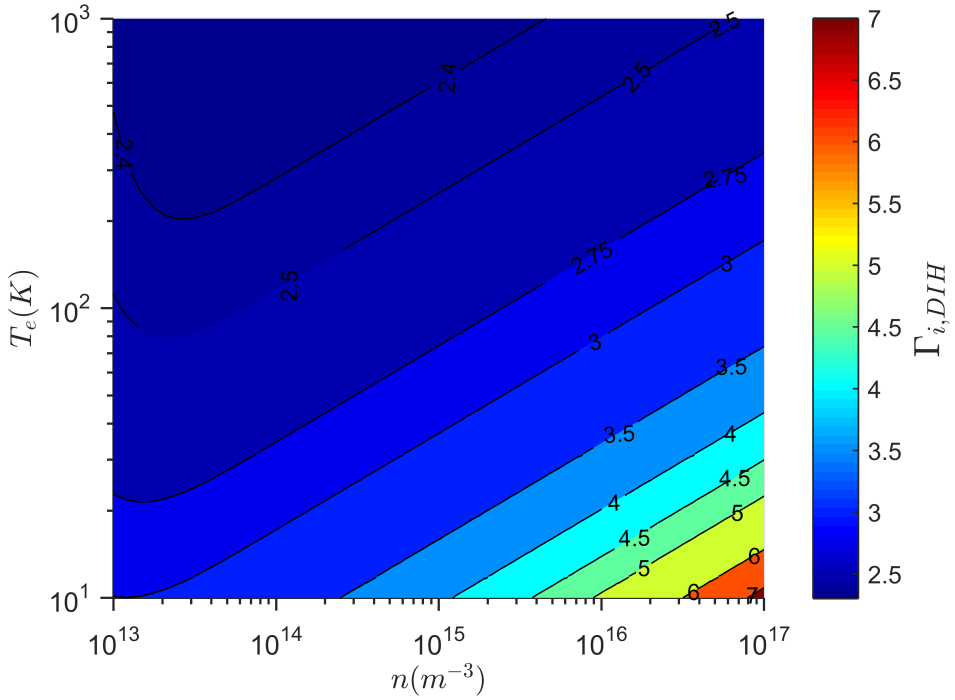

Figure 3.8 : Calculated Γ_i for DIH equilibration temperatures. The seemingly interesting regime of high density low electron temperature is not only experimentally inaccessible for us, but it is precisely the regime of strong electron coupling which presents many complications as discussed in Secs. 3.6 and 4.0.6

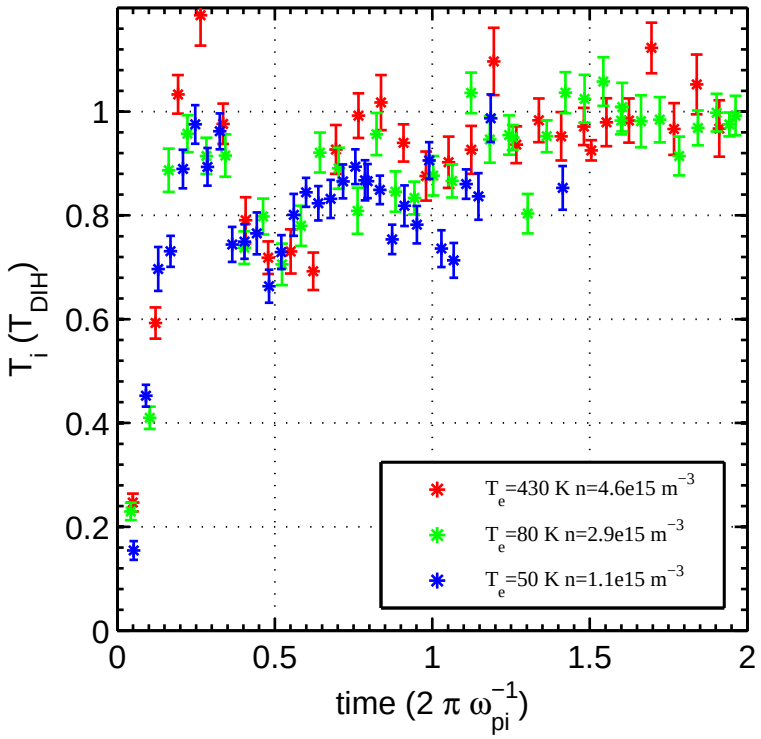

Figure 3.9 : Early time ion temperatures show disorder induced heating and kinetic energy oscillations. This is the same data as Figure 3.3 but here the temperatures has been scaled by the DIH temperature calculated as in Eqn. 3.5 and time has been scaled by the ion plasma oscillation period, i.e. the inverse of Eqn. 3.6.

3.4 Adiabatic Expansion

Macroscopically, the most prominent dynamic of the plasma cloud is it's free expansion into the surrounding vacuum. This takes place over 10 µs timescales and is driven primarily by the electron thermal pressure. Similar to an ideal gas this should result in a cooling of the constituents and indeed long time measurements of ion temperature evolution show dramatic cooling. See Fig. 3.10 for examples of experimental data. Notice how the initial DIH temperature depends primarily on density and the expansion time scale depends inversely on the electron temperature.

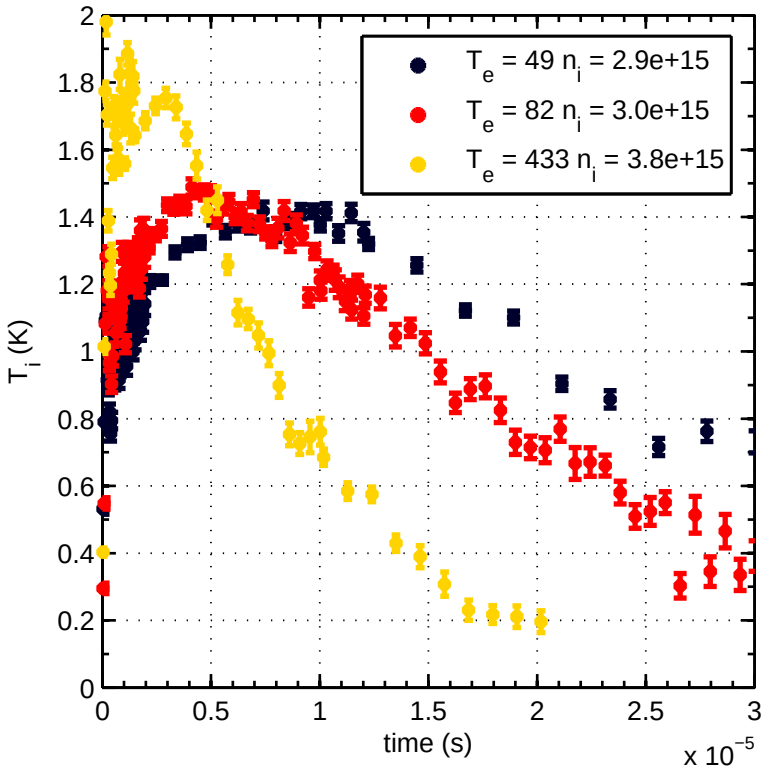

Figure 3.10 : Long time temperature evolution shows the rapid DIH then a decrease from the equilibrium temperatures as the UNP adiabatically expands into the vacuum chamber. The time scale is set by the electron temperature and the cloud size. Here we have varied the electron temperature by nearly an order of magnitude. Initial cloud radius is, σ_0 =1 mm

This expansion can be well described in the case of UNPs by neglecting radiative and collisional processes and using the Vlasov description of a plasma. Assuming quasineutrality and a Gaussian density distribution, UNPs realize a rather unusual exact solution to Vlasov's equation [65]. The size of the cloud evolves as

$$\sigma(t) = \sqrt{\sigma_0^2(1 + t^2/\tau_{exp}^2)} \tag{3.9}$$

where

$$\tau_{exp} = \sqrt{m_i \sigma_0^2 / k_B \left[T_e(0) + T_i(0)\right]}, \tag{3.10}$$

is the characteristic expansion timescale. See Fig. 3.11 for typical values of τ_{exp}.

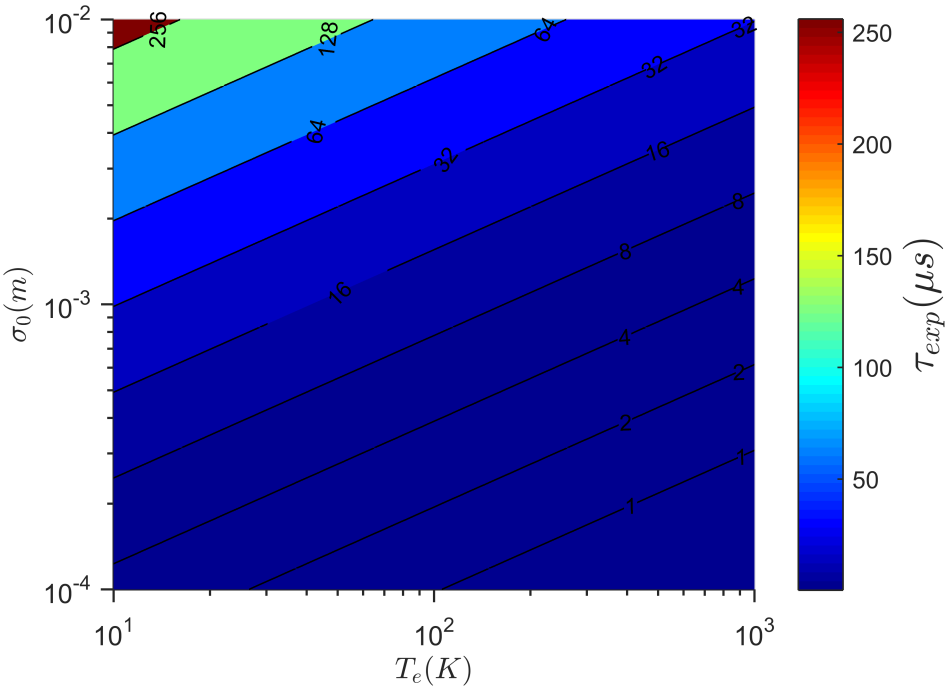

Figure 3.11 : Typical values for τ_{exp} plotted versus $T_e(0)$ and σ_0.

By fitting experimental data to Eqn. 3.9 one can indirectly measure the initial electron temperature. Agreement with expectations is good for weakly coupled

electrons, up to electron temperatures approaching 500 K when the ionizing laser appears to go multimode, obscuring further measurements. At the lowest electron temperatures three-body recombination acts to enhance the expansion and fit electron temperatures are higher than expectations. Expectations are based off saturated absorption calibration of the ionizing laser conducted roughly 10 years ago.

The exact solution of Ref. [65] also shows cooling of both the ions and electrons as described by the following equations,

$$\frac{\partial T_{i,e}(t)}{\partial t} = -2\gamma(t)T_{i,e}(t) \tag{3.11}$$

$$\gamma(t) = \frac{t/\tau_{exp}^2}{1 + t^2/\tau_{exp}^2} \tag{3.12}$$

or

$$T_{i,e}(t) = \frac{T_{i,e}(0)}{\left(1 + t^2/\tau_{exp}^2\right)}. \tag{3.13}$$

The combination of Eqns. 3.9 and 3.13 shows the adiabatic nature of the cooling, i.e. $T_i * \sigma^2 = cons.$ By scaling the previous data by the expansion timescale (τ_{exp}) we see that adiabatic expansion nearly dominates the long time dynamics, e.g. see Figure 3.12. Despite the accompanied decrease in density, it has been shown this cooling results in an increase of Γ_i. [74] However at about $\Gamma_i \sim 10$, the correlations freeze out, because the time scale for the evolution of the correlations becomes much larger than that of the expansion. Also, the electron temperature experiences a lower limit, at which three-body recombination acts to reheat the electrons. This will be discussed in more detail in Sec. 3.6

The expansion γ describes the bulk velocity as well, by the following expression,

$$\mathbf{v}(\mathbf{r}) = \gamma(t)\mathbf{r}. \tag{3.14}$$

The bulk velocity is radially directed and proportional to the radius ($\mathbf{r}$) reflecting the self-similar nature of the expansion. This behavior is clearly evident in regional

analysis results summarized in Fig. 2.11 and Fig. 2.10. Center frequencies obtained from Voigt profile spectral fits are negatively proportional to the x-component of the local bulk velocity,

$$v^x_{bulk} \equiv \mathbf{v}(\mathbf{r}) \cdot \hat{x} = -\lambda_{img}\nu^x_{exp}. \tag{3.15}$$

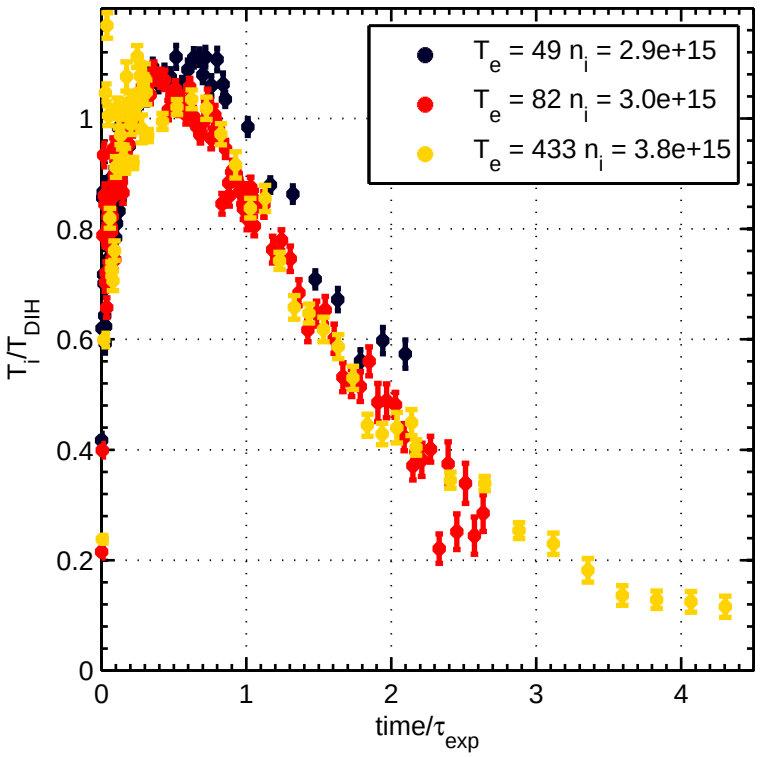

Figure 3.12 : Long time temperature evolution shows decrease from DIH temperatures as the UNP adiabatically expands into the vacuum chamber. Same data as 3.10 but the temperatures have been scaled by T_{DIH} and the times by τ_{exp}.

3.5 Electron Ion Collisions

Due to the large discrepancy in mass between ions and electrons, collisional energy transfer between the two is inefficient and thermalization would take many times the lifetime of our plasmas. This is why collisional energy exchange is typically neglected

in UNP theory. [75] However, if one is concerned with ion temperatures, electron-ion heat exchange must be considered since the ions are typically orders of magnitude colder than electrons.

Historically, collisional rates have been uncertain because the long-range Coulomb force leads to logarithmic divergences. [119, 120, 90] Due to difficulties in isolating the phenomena and the quickly evolving nature of most plasma systems, measurement of the collisional frequency has been an elusive goal of experiment. [121] Molecular dynamics simulation are complicated by tendency of opposite charges to recombine and thus rely on semi-classical potentials or the use of like charges. [78] Only recently have MD simulations been successful in measuring thermalization rates for oppositely charged species using the classical Coulomb interaction. [80]

The thermalization rate is based off the classical Spitzer electron-ion collision frequency which is found by integrating Coulomb collisions over the appropriate range of impact parameters and thermal velocities. This treatment leads to the following expression for the collision rate, which includes the assumptions of singly ionized species, $m_i >> m_e$, and $T_e >> T_i$, [119]

$$\gamma_{EIC} = \frac{4\sqrt{2\pi} n_i e^4 \ln[\Lambda]}{3(4\pi\varepsilon_0)^2 m_e^{1/2} (k_B T_e)^{3/2}}. \tag{3.16}$$

The Coulomb logarithm, $\ln[\Lambda]$, is defined as the natural log of the ratio of maximum to minimum impact parameters, b_{max} and b_{min}, respectively.

$$\ln[\Lambda] \equiv \ln\left[\frac{b_{max}}{b_{min}}\right]. \tag{3.17}$$

For weakly coupled electrons, i.e. $\Gamma_e << 1$, the maximum impact parameter is approximately the Debye shielding length, i.e. the extent of $\vec{E}$-fields within the plasma. The minimum impact parameter is estimated as the distance of closest

approach for electron-ion collisions,

$$R_c \equiv \frac{e^2}{4\pi\varepsilon_0 k_B T_e}, \tag{3.18}$$

also known as the Landau length. This leads a Coulomb logarithm of the following form,

$$\ln[\Lambda] \equiv \ln\left[\frac{C\lambda_D}{R_c}\right], \tag{3.19}$$

where C is a constant somewhere between $1-3$ depending on various levels of estimation [119, 122] and approximation [123, 124, 125].

However, more sophisticated theories have since agreed that $C = 0.765$ [126, 127] as verified in recent molecular dynamics simulations [80] Deviations of the Coulomb logarithm from this formula due to strong coupling are minimal within our typical regime. [128] Regardless we use an expression for the Coulomb logarithm developed from MD simulation results that is valid up to $\Gamma_e \approx 10$ [80]

$$\ln[\Lambda] \approx \ln\left[1 + 0.7\lambda_D/R_c\right]. \tag{3.20}$$

To gain intuition for the collisional frequency it is straightforward to recast γ_{EIC} as a function of various plasma quantities,

$$\gamma_{EIC} = \sqrt{\frac{2}{3\pi}}\Gamma_e^{3/2}\omega_{pe}\ln[\Lambda]. \tag{3.21}$$

As clearly seen and expected, other than a numerical factor, the electron plasma frequency sets the time scale for collisional exchange of momentum. It's important to note this is the time scale for momentum loss and not energy exchange. To find the latter, one must employ conservation of energy which leads to an ion heating density of, [129, 130]

$$Q_i = 3\frac{m_e}{m_i}\gamma_{EIC} n_e T_e. \tag{3.22}$$

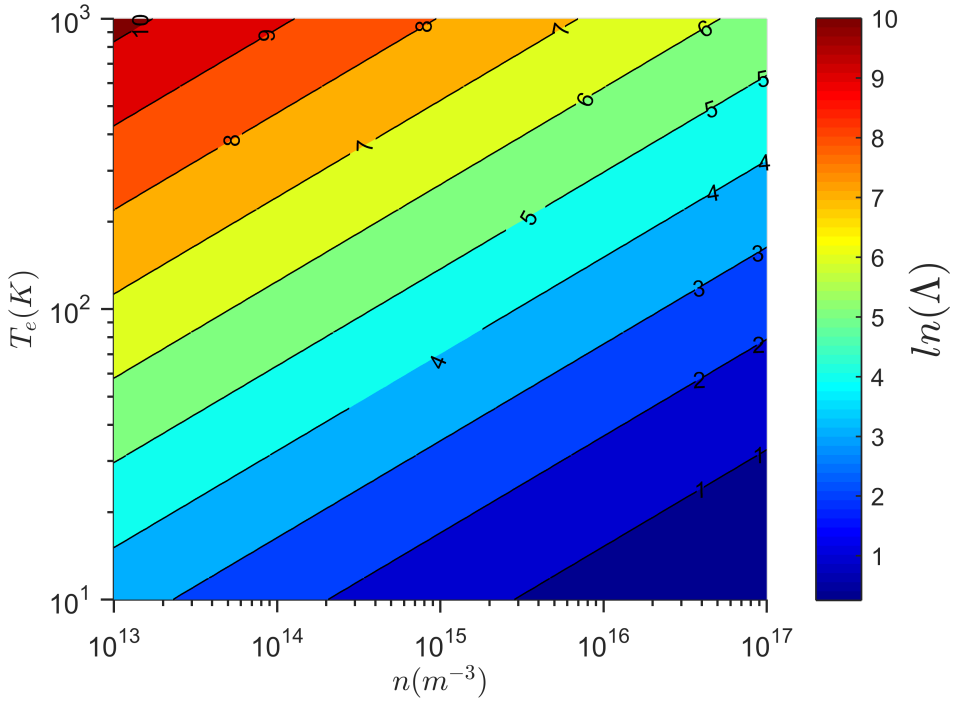

Figure 3.13 : Typical values for ln[Λ] plotted versus T_e and n, calculated with Eqn. 3.20.

Which results in the following expression for ion heating due to collisions with electrons,

$$\frac{3}{2}n_i\frac{dT_i}{dt} = Q_i = 3\frac{m_e}{m_i}\gamma_{EIC}n_eT_e \tag{3.23}$$

or

$$\frac{dT_i}{dt} = 2\frac{m_e}{m_i}\gamma_{EIC}T_e \tag{3.24}$$

Typical values for this heating rate are plotted in Fig. 3.14 and are on the order of 10s of mK μs^{-1}. Notice how heating is less effective at higher T_e due to the diminishing Rutherford cross section.

From Eqn. 3.24 we define the thermalization time scale as,

$$\tau_{EIC} \equiv \left[2\frac{m_e}{m_i}\gamma_{EIC}\right]^{-1} \tag{3.25}$$

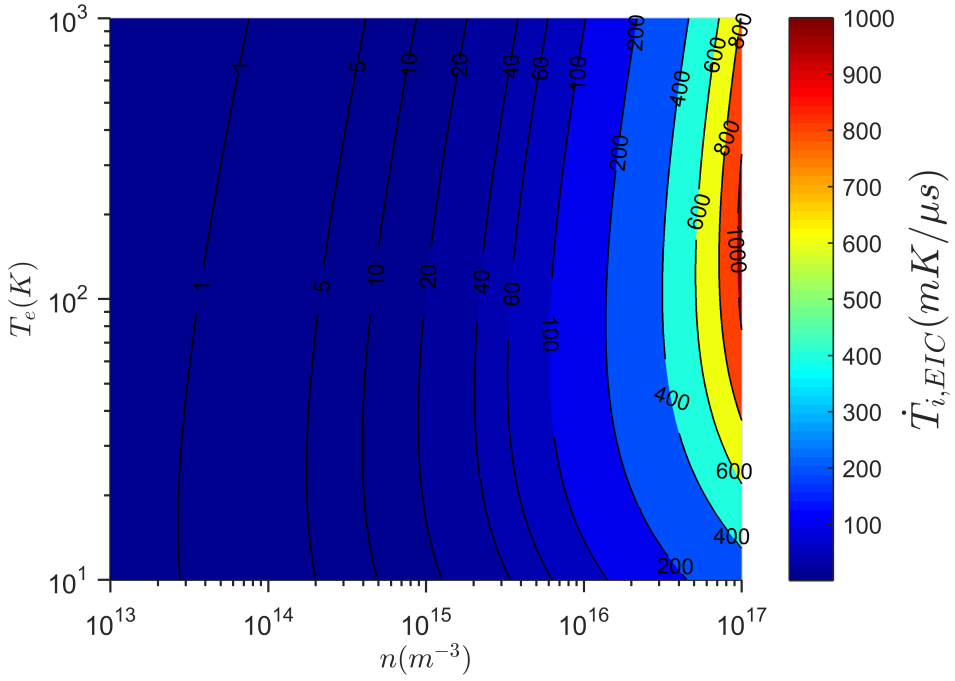

Figure 3.14 : Typical values for $\frac{dT_i}{dt}$ due to electron-ion heating plotted versus T_e and n, calculated with Eqn. 3.24 assuming a constant density and T_e.

Typical values for τ_{EIC} are shown in Fig. 3.15. Take note, these values are calculated for an otherwise non-changing plasma and do not account for the decreasing density and T_e due to plasma expansion. Regardless, in all typical regimes the thermalization time is much greater than τ_{exp} indicating that the plasma expansion will quickly quench electron-ion thermalization.

To approximate the combined effects of electron-ion collisions and adiabatic expansion. One can consider various helpful scalings of the heating process that help gain insight into the interplay of the opposing effects. For instance, the total amount of heat transferred within the first τ_{exp} has been plotted in 3.16. These data can be scaled by T_{DIH} for a relative measure of ion heating compared to initial temperatures.. These plots do not account for the changing plasma conditions during the first τ_{exp} and are upper bounds at best. More accurate results using the full model

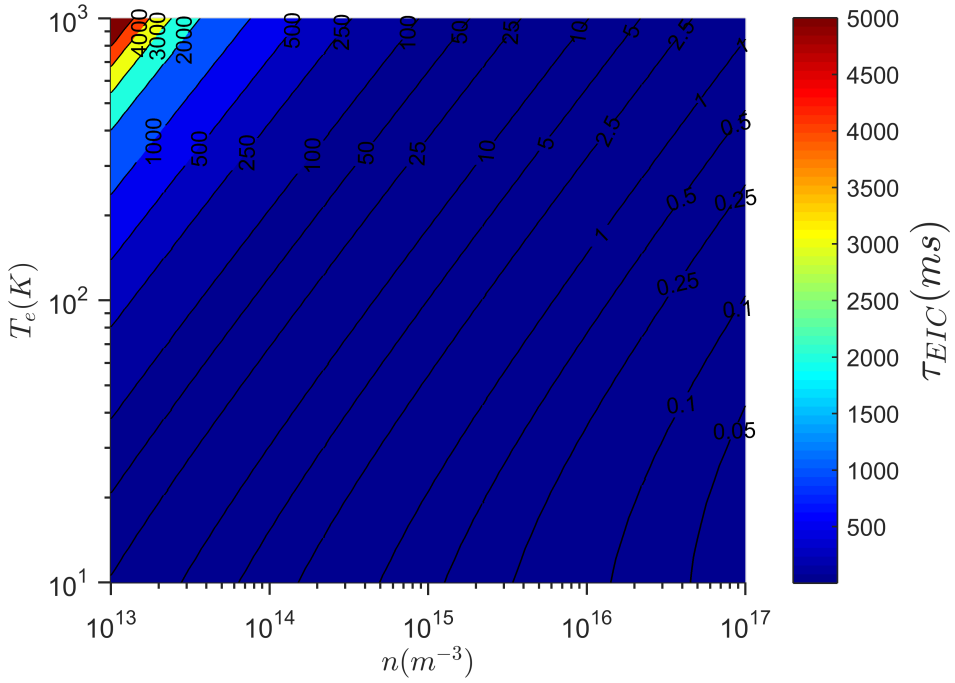

Figure 3.15 : Typical values for τ_{EIC} plotted versus T_e and n, calculated with Eqn. 3.25.

presented within are shown in Sec. 4.0.5.

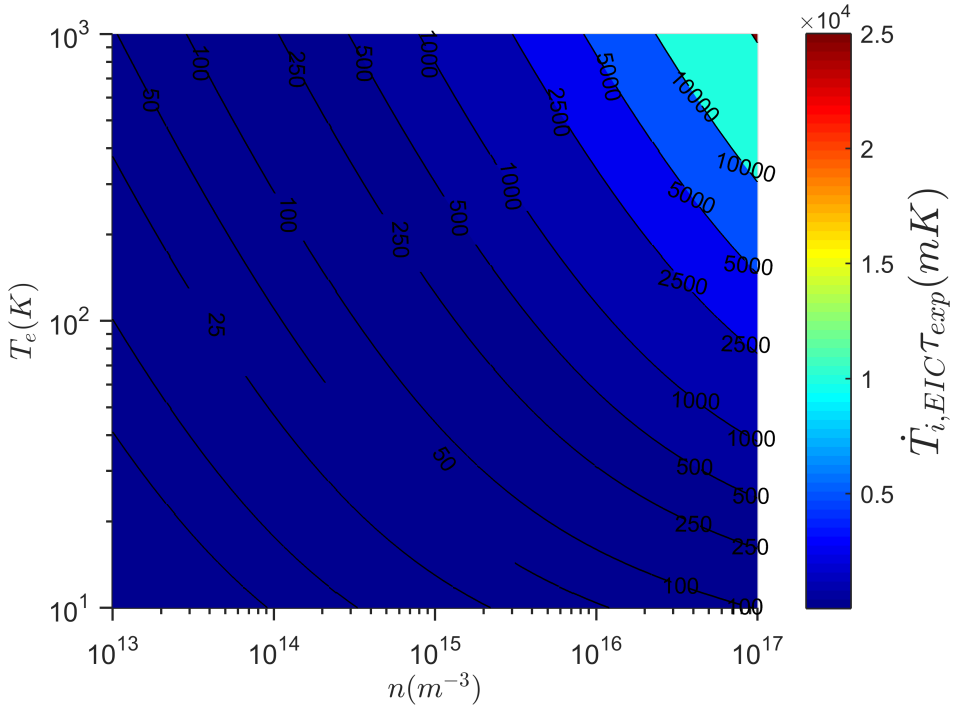

Figure 3.16 : Total temperature gained by ions due to ion-electron collisions over a time equal to τ_{exp} for a 1 mm ^{88}Sr UNP. Note, this figure does not account for changing the plasma conditions due to the global expansion.

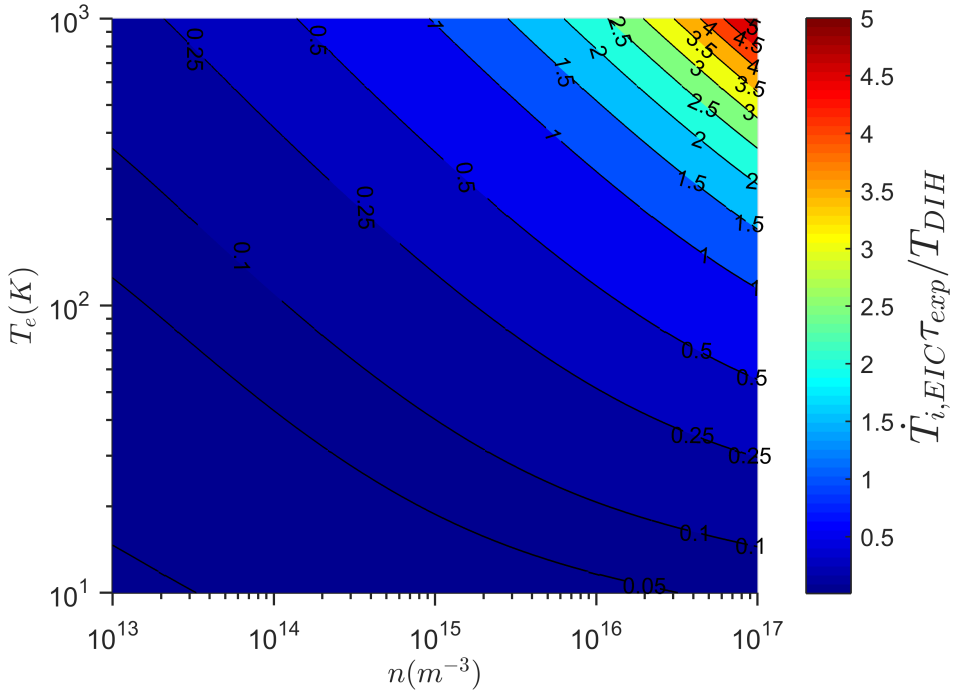

Figure 3.17 : Similar to Fig. 3.16 except normalized by initial disorder induced heating temperatures.

3.6 Three-body Recombination

At low enough collision energies, electrons and ions within the plasma can recombine to form Rydberg atoms, with a second electron carrying away the excess kinetic energy. This process of three body recombination (TBR) will lower the plasma density while heating the electrons. As a UNP expands and the electron temperature drops one can easily reach a regime in which three-body recombination (TBR) becomes significant, this happens at about $\Gamma_e \sim 0.1$. [31, 131, 132, 133] Since the TBR rate has a strong dependence on ion temperature, $A_{TBR} \propto T_i^{-9/2}$, [134] and Γ_e has a relatively weak dependence, $\Gamma_e \propto T_i^{-1}$ any further electron cooling that would attempt to increase Γ_e beyond 0.1 results in marked increase of TBR and thus Γ_e has an effective ceiling. This was shown to self-limit at or about $\Gamma_e \sim 0.2$. [109] For the data presented in this thesis $\Gamma_e \lesssim 0.1$ so this effect is mostly insignificant, nonetheless, the machinery for handling the onset of TBR approximately is presented is Sec. 4.0.4

Chapter 4

Numerical Modeling of UNP Dynamics

In this chapter we present a numerical model describing many parameters of a UNP's evolution, including cloud size and both electron and ion temperatures. While most of the pieces have been considered before individually, this work represents a new synthesis of several theories into an accurate description of long time UNP dynamics.

4.0.1 Modeling Disorder Induced Heating and Kinetic Energy Oscillations

Modeling the initial stage of UNP evolution is complicated by the lack of both thermodynamic equilibrium and a closed form description for the dynamics. Currently the only way to predict KEO dynamics is by use of molecular dynamics simulations. This leaves one with two obvious approaches, of which we take both; approximation and direct comparison with simulation results.

Approximating DIH

In many cases the early time details of KEOs can be overlooked and the DIH process can be approximated as a monotonic relaxation towards equilibrium. We follow the treatment in Ref. [53] which evolves the potential energy due to correlations from it's initial value of zero to the equilibrium value ($U_{ii,eq}$) discussed in Sec. 3.1, using one quarter of the inverse ion plasma freq as the time scale and a linear approximation

for it's evolution,

$$\frac{dU_{ii}}{dt} = -\frac{U_{ii} - U_{ii_{eq}}}{\tau_{DIH}}. \tag{4.1}$$

Note, here we use a slightly different time scale then that proposed in Ref. [53], ours is $2\pi/4 \approx 1.5$ times longer and results in a fit that bisects the oscillations a little more evenly. Multiplying our timescale by an additional factor of three brings the approximation nearly to T_{DIH} by the time of the first peak in temperature. Since this treatment fails to describe the oscillatory nature of DIH, the specific timescale is somewhat arbitrary.

The release of correlation energy can be related to the ion temperature as,

$$\frac{dT_i}{dt} = \frac{2}{3k_B}\frac{U_{ii} - U_{ii_{eq}}}{\tau_{DIH}}, \tag{4.2}$$

assuming the lack of any other factors affecting it, which is a reasonable assumption on times much less than the plasma expansion time, τ_{exp}. Comparison of Eqn. 4.2 with experimental data can be seen in Fig. 4.1. We see that this treatment gives proper equilibrium temperatures at about the time the oscillations damp out but clearly does not describe KEOs. Agreement is slightly worse at lower electron temperatures; preliminary results from other projects within the lab appear to show a slower equilibrium than perhaps expected, presumably due to electron shielding. Further study is being conducted and will be published in the near future.

Ultimately, the lack of oscillations in this treatment causes complications for non-linear fitting routines, the primary tool of our analysis. The results are sensitive to aliasing effects, if an insufficient number of points are taken per oscillation period. Even with infinite temporal resolution, this model is not best in the least-squares sense. While the least-squares issue could be solved by finding the appropriate exponential time scale as a function of Γ_e, aliasing effects are practically unavoidable

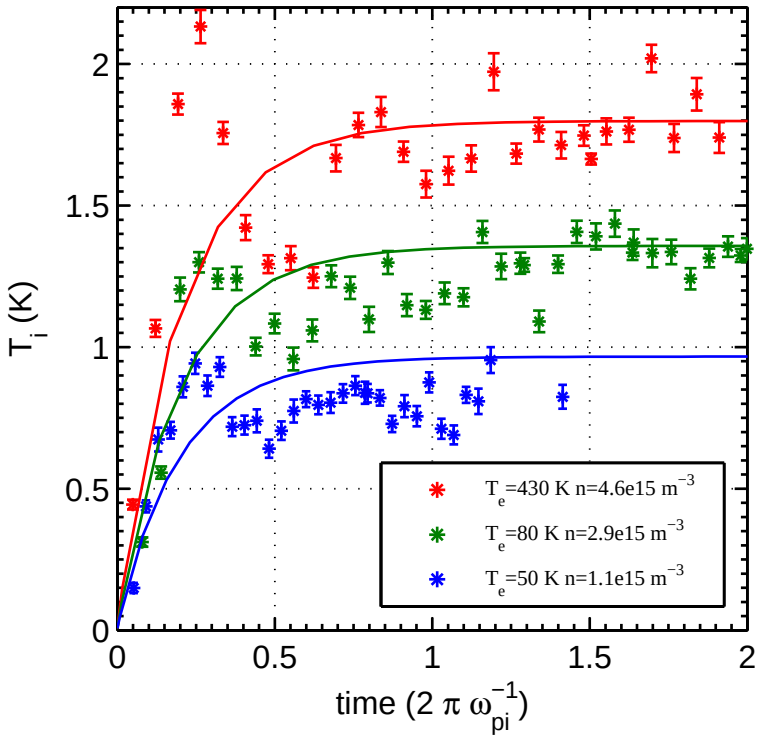

Figure 4.1 : Linear approximation of DIH (i.e. Eqn. 4.2) compared to early time experimental data for a range of densities and electron temperatures. Qualitative agreement is good however the model clearly lacks kinetic energy oscillations.

without taking very detailed early time data, which is otherwise usually unnecessary. Whenever possible it is recommended to exclude the first two plasma oscillation times from the data that is used to fit the long-time model. After fit results are calculated, the early time measurements can be visually inspected for agreement and should be similar to Fig. 4.1

Molecular Dynamics Simulation

We recently obtained results of MD simulations of equilibrating UNPs from Thomas Pohl at the Max Planck Institute for Complex Systems in Dresden, Germany. With

careful consideration these can be directly compared to experimental results and represent the best description available for kinetic energy oscillations. In this simulation, electrons are considered as a neutralizing background and screening is accounted for via the ions' evolution under Yukawa potentials,

$$U_{ii}^{Y}(r) = \frac{1}{4\pi\varepsilon_0}\frac{e^2 \exp^{-\frac{r}{\lambda_D}}}{r}, \tag{4.3}$$

which is simply the bare Coulomb potential exponentially attenuated over a characteristic length scale equal to the Debye length.

In order to accurately compare with experimental data we process the simulation results in the same way we do experimental data. Velocity distributions are constructed from the raw data and convolved with a Lorentzian representing the laser and natural ion linewidths to generate a simulated LIF spectrum. These spectra are then fit to Voigt profiles in order to measure an effective temperature. While this will result in comparable numbers the reader should be reminded the ions are not in thermodynamic equilibrium and do not have a well defined temperature. Further implications will be discussed in Sec. 4.1.1. Regardless of these technicalities, effective temperatures from the simulation agree well with experimental data when density is a fit parameter, see Fig. 4.2. The density obtained from this technique agrees with calibrations based off absorption imaging however the uncertainty is reduced by roughly a factor of four, from 20% to 5%. The details of the fitting technique were studied thoroughly by Thomas Langin and are to be detailed in his master's thesis as well as an upcoming publication.

However the agreement is not perfect. The initial rise in temperature and the first oscillation are very well described, but as time passes the agreement deteriorates slightly. This is likely due to a couple effects not considered in the simulation, namely collisional energy transfer between ions and electrons as well as the expansion of the

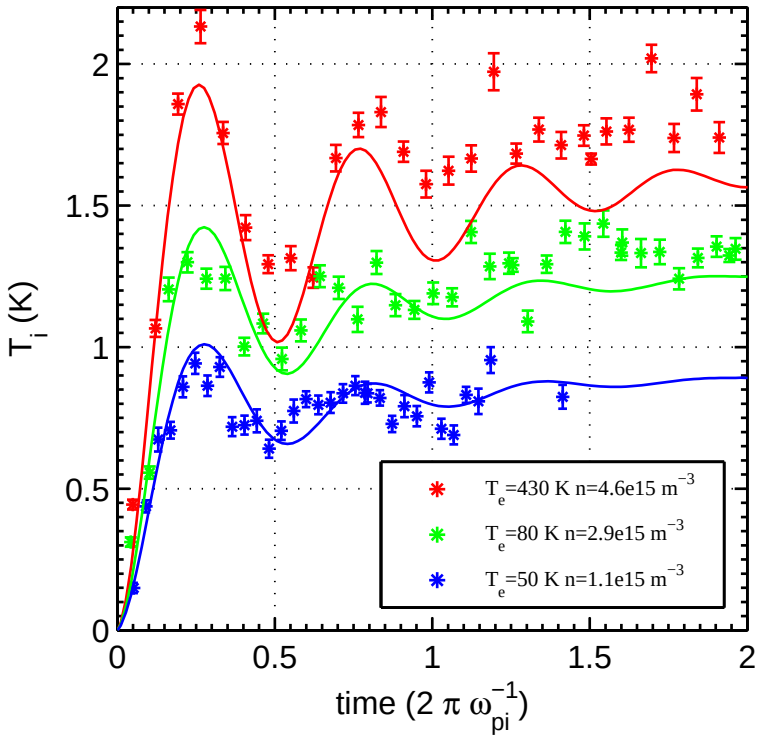

Figure 4.2 : Molecular dynamics simulation of kinetic energy oscillations compared to experimental data. Early time ion temperature measurements agree well with results from MD simulations of equilibrating Yukawa plasmas. Here density is a single fit parameter which agrees with calibration by absorption. Discrepancies tend to increase as time passes hinting at longer time scale dynamics.

UNP cloud. In some regimes, the effects of EICs and/or adiabatic cooling can be significant before the ions have reached local thermal equilibrium. Particularly, at low densities when the KEOs are slower or at low T_e where EICs are most significant. To address this we simply *ad hoc* adjust the simulation results by two terms, one accounting for each effect. We integrate heating due to EICs and simply add that amount of heat to the simulation results. Then we adjust for adiabatic cooling using

the factor we saw earlier in Eqn. 3.13, i.e.

$$T^{\star}_{i,sim}(t) = \frac{T_{i,sim}(t) + \int_0^t d\tau \gamma_{EIC}(\tau) T_e(\tau)}{1 + t^2/\tau^2_{exp}}. \tag{4.4}$$

In appropriate regimes this improves the agreement with experimental results as seen in Fig. 4.3.

These fits have been used to verify calibration obtained from ion absorption imaging and the two methods agree within their relative uncertainties. When KEO data are available for a particular dataset, the density values from the MD simulation fits are used to calculate plasma parameters, such as expected temperature evolution. When KEO data are not available, density values are obtained from calibrated fluorescence. The calibration is consistent and reliable based on comparison of the two methods, however calibration accuracy relies on optimal experimental alignment as well as accurate knowledge of the plasma cloud shape and imaging beam intensity profile.

4.0.2 Adiabatic Expansion

Fortunately a detailed numerical model of UNP dynamics already exists, [38] although we will show how it is incomplete, it represents a tremendous effort and numerous accomplishments towards understanding these systems. Copied from Ref. [38],

$$\frac{\partial \sigma^2(t)}{\partial t} = 2\gamma(t)\sigma^2(t) \tag{4.5}$$

$$\frac{\partial T_{e,i}(t)}{\partial t} = -2\gamma(t) T_{e,i}(t) \tag{4.6}$$

$$\frac{\partial \gamma(t)}{\partial t} = \frac{k_B T_e(t) + k_B T_i(t)}{m_i \sigma^2(t)} - \gamma^2(t) \tag{4.7}$$

describes the evolution of the cloud size and constituent temperatures parametrized by expansion γ. Equations 3.9 through 3.14 represent an exact solution to this set of

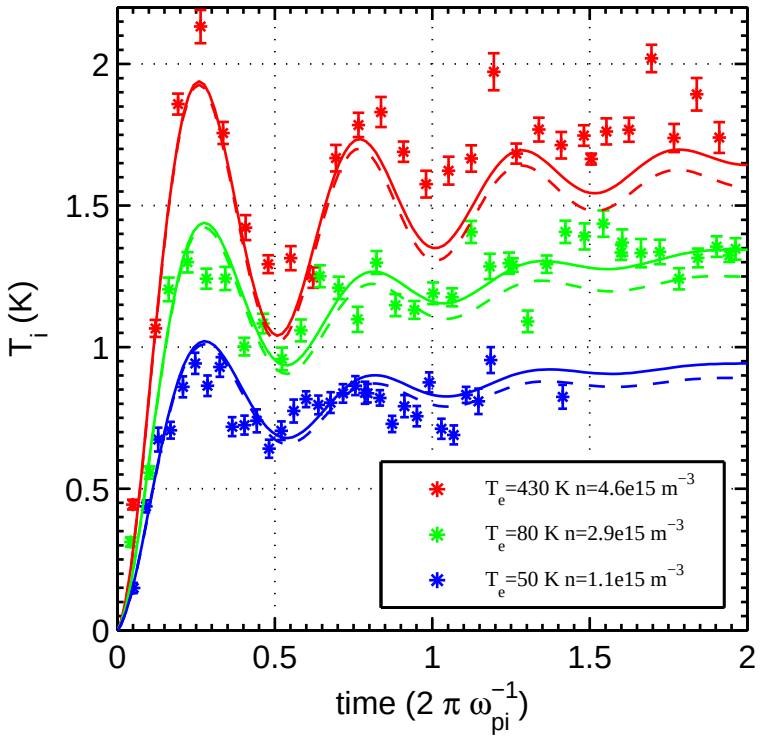

Figure 4.3 : Molecular dynamics simulation of kinetic energy oscillations adjusted for EIC and adiabatic cooling compared to experimental data. Adjusting molecular dynamics results for EICs and adiabatic cooling enhances agreement slightly. Solid lines are the adjusted simulation results and dashed lines are the raw unadjusted MD results. The remaining discrepancy in the T_E =430 K data will be addressed later.

differential equations. These equations are found from the Vlasov approximation to a kinetic treatment (i.e. a vanishing collision term), assuming quasineutrality, separate thermal equilibrium for ions and electrons, and a Gaussian density distribution. At this level of treatment DIH is incorporated by setting $T_i(0) = T_{DIH}$ which implies that this model will not accurately describe the early time dynamics of DIH and KEOs. This prompted the development of a more sophisticated model, which is given in the following section.

Including Correlations

Fortunately again, Pohl et. al. [53] expanded this model to included the effects of correlations. Resulting in the following set of differential equations:

$$\frac{\partial \sigma^2(t)}{\partial t} = 2\gamma(t)\sigma^2(t) \tag{4.8}$$

$$\frac{\partial \gamma(t)}{\partial t} = \frac{k_B T_e(t) + k_B T_i(t) + \frac{1}{3}U_{ii}(t)}{m_i \sigma^2(t)} - \gamma^2(t) \tag{4.9}$$

$$\frac{\partial U_{ii}(t)}{\partial t} = -\frac{U_{ii}(t) - U_{ii,eq}(t)}{\tau_{DIH}} \tag{4.10}$$

$$\frac{\partial T_e(t)}{\partial t} = -2\gamma(t)T_e(t) \tag{4.11}$$

$$\frac{\partial T_i(t)}{\partial t} = -2\gamma(t)T_i(t) - \frac{2}{3}\left[\gamma U_{ii}(t) + \frac{\partial U_{ii}(t)}{\partial t}\right]. \tag{4.12}$$

These equations are found from a kinetic treatment for the evolution of the one-particle distribution function for ions and elections retaining a term describing ion-ion correlations as a collision term. Quasi-neutrality, separate ion and electron thermal equilibrium, and a Gaussian density distribution are assumed. $U_{ii}(t)$ is the same correlation energy discussed earlier and it's inclusion now brings the process of DIH into the model and identifies a small cooling due to decreasing density and diminishing spatial structure, in essence reverse DIH. We know that DIH is a result of the release of correlation energy and increases primarily as a function of density. It follows that as the cloud expands that the falling density would then reabsorb correlation energy as the nearest neighbor potential energy decreases. This effect is on the order of $\approx$ 50 mK or less and although it's essentially negligible for most of out parameter space it is already included in the model by virtue of how DIH is accounted for, i.e. it's simply a drop in $U_{ii_{eq}}$. On the other hand, this effect is very important to models of recent results with UCNPs formed from high-density molecular beams. [135]

Inherent in the traditional interpretation of Eq. 4.10, however, is an assumption

of global thermal equilibrium for the ions that is not well-justified. The equilibrium correlation energy depends on the local density, and disorder-induced heating only leads to local thermal equilibrium. The characteristic timescale for global ion thermal equilibration τ_{therm} is set by the thermal conductivity for the strongly coupled ions, which can be approximated as $\lambda \approx nk_B\omega_{pi}a_{ws}^2$. [136] Temperature equilibration between the ions in two regions of volume V, interface area A, and separation d is $\sim c_V V d/\lambda A$, where $c_V = 3nk_B/2$ is the ion heat capacity per volume. Taking all length scales as the plasma size σ, this yields $\tau_{therm} \approx \sigma^2/\omega_{pi}a_{ws}^2$, which is on the order of 10^{-3} s for a typical UNP - much longer than other dynamic timescales for the plasma.

This creates a significant complication for a rigorous description of the plasma, but we take advantage of the extremely long timescale for ion global equilibration to make a significant approximation to describe our data. We restrict our analysis to a central region of the plasma in which the average density is 96% of the peak density. We consider Eq. 4.10 as describing an effective temperature for local thermal equilibribrium within this region. While previous treatments [53] have approximated $U_{ii,eq}(t)$ as an average over the equilibrium correlation energy in the entire plasma, we take it as the correlation energy for the measured plasma density, which is the average density of our region of interest. Several additional factors make Eq. 4.10 a reasonable approximation for the local ion conditions. The actual error introduced with this approximation is small because the temperature after local equilibration $\sim T_{DIH}$ varies slowly with density. Also, the self-similar plasma expansion leads to the same relative change in volume and adiabatic cooling in all regions of the plasma. Finally, the plasma expansion, which controls the adiabatic cooling dynamics, is dominated by the electron temperature for our conditions and is relatively insensitive to the ion

temperature.

4.0.3 Including Electron Ion Heating

Starting with Pohl's model including correlations we add a collisional term to transfer energy between species.

$$\frac{\partial \sigma^2(t)}{\partial t} = 2\gamma(t)\sigma^2(t) \tag{4.13}$$

$$\frac{\partial \gamma(t)}{\partial t} = \frac{k_B T_e(t) + k_B T_i(t) + \frac{1}{3}U_{ii}(t)}{m_i \sigma^2(t)} - \gamma^2(t) \tag{4.14}$$

$$\frac{\partial U_{ii}(t)}{\partial t} = -\frac{U_{ii}(t) - U_{ii,eq}(t)}{\tau_{DIH}} \tag{4.15}$$

$$\frac{\partial T_i(t)}{\partial t} = -2\gamma(t)T_i(t) - \frac{2}{3}\left[\gamma U_{ii}(t) + \frac{\partial U_{ii}(t)}{\partial t}\right] + \frac{T_e(t) - T_i(t)}{\tau_{EIC}} \tag{4.16}$$

$$\frac{\partial T_e(t)}{\partial t} = -2\gamma(t)T_e(t) - \frac{T_e(t) - T_i(t)}{\tau_{EIC}}. \tag{4.17}$$

4.0.4 Including Three-body Recombination

We can also approximate TBR by turning off adiabatic electron cooling when $\Gamma_e > 0.2$. To model this effect in a simplistic manner one can artificially turn off electron adiabatic cooling when $\Gamma_e > 0.2$ by solving

$$\frac{\partial \Gamma_e(t)}{\partial t} = 0, \tag{4.18}$$

which leads to

$$\frac{\partial T_e(t)}{\partial t} = -\gamma(t)T_e(t), \tag{4.19}$$

as shown in Appendix A.1. Therefore by inclusion of the logical function

$$\mathcal{F}(\Gamma_e) = \begin{cases} 1, & \text{if } \Gamma_e > 0.2, \\ 0, & \text{otherwise.} \end{cases} \tag{4.20}$$

we can conditionally turn off the adiabatic electron cooling term at a Γ_e ceiling with the following modification,

$$-2\gamma(t)T_e(t) \rightarrow -\left[2-\mathcal{F}(\Gamma_e)\right]\gamma(t)T_e(t). \tag{4.21}$$

However, very little data discussed in this thesis crosses into the region with $\Gamma_e > 0.2$.

4.0.5 Complete Model

Combining all the terms shown in this chapter we present our revised UNP dynamics model,

$$\frac{\partial\sigma^2(t)}{\partial t} = 2\gamma(t)\sigma^2(t) \tag{4.22}$$

$$\frac{\partial\gamma(t)}{\partial t} = \frac{k_B T_e(t) + k_B T_i(t) + \frac{1}{3}U_{ii}(t)}{m_i\sigma^2(t)} - \gamma^2(t) \tag{4.23}$$

$$\frac{\partial U_{ii}(t)}{\partial t} = -\frac{U_{ii}(t) - U_{ii,eq}(t)}{\tau_{DIH}} \tag{4.24}$$

$$\frac{\partial T_i(t)}{\partial t} = -2\gamma(t)T_i(t) - \frac{2}{3}\left[\gamma U_{ii}(t) + \frac{\partial U_{ii}(t)}{\partial t}\right] + \frac{T_e(t) - T_i(t)}{\tau_{EIC}} \tag{4.25}$$

$$\frac{\partial T_e(t)}{\partial t} = -\left[2-\mathcal{F}(\Gamma_e)\right]\gamma(t)T_e(t) - \frac{T_e(t) - T_i(t)}{\tau_{EIC}}. \tag{4.26}$$

Comparison of UNP Model with Experimental Data

We can now compare this with experimental data as in Fig. 4.4. The insets show early time data fit to MD results in order to determine density and the main plots show long time evolution for various initial densities and electron temperatures. Dashed lines are the results of Eqns. 4.13 through Eqn. 4.17 (i.e. model with correlations, without EICs), which clearly miss a significant amount of ion heating. Solid lines are the results of Eqns. 4.22 through Eqn. 4.26 which shows much better aggreement with experimental data. The agreement is good although there is clearly a bit of additional heat that appears around τ_{exp}. Discrepancies on the order of 200 mK to

400 mK are typically shown, as in Fig. 4.5. The unaccounted for energy seems to increase with electron temperature and density. Arguments for the source of this heat are given in Chapter 5.

Density evolutions measured over the same data sets show the effect of adiabatic expansion on plasma densities. After a few τ_{exp} have transpired, the plasma densities become too low for reasonable data collection rates. Some of the latest time points presented took several hours each to collect enough statistics. That explains the significant errorbars at late times.

Electron Temperature Evolution

We can also look at the expected evolution of the electron temperature as calculated by the complete model. The results from the same six datasets of Fig. 4.4 are shown in Fig. 4.7. They clearly show a rapid decrease in electron temperature due to adiabatic expansion. Comparison of the results with EICs turned off to the full model (not shown) indicate that EICs have very little effect on electron temperature evolution in our system, insignificant given the uncertainty in initial T_e.

With knowledge of the evolving electron temperature we can now calculate the expected evolution of Γ_e as shown in Fig. 4.8. Using experimentally obtained densities, we observe dramatic increase in the electron's Coulomb coupling parameter. For the lowest electron temperatures studied here, T_e =25 K the coupling parameter approaches 0.2, the value at which TBR becomes significant. On the other hand at the highest electron temperatures, T_e =430 K coupling parameters are clearly in the weakly coupled regime. Both regimes of strongly-coupled and weakly-coupled electrons are easily accessible using ultracold neutral plasmas and these do not represent the highest nor the lowest values attainable.

Observed Ion Heating Due to Electron-Ion Collisions

In general Coulomb collisions are less effective as the relative velocities between species increases and this is evident by the decreased contribution from EICs at higher T_e (Fig. 4.4 bottom row vs. top row). Despite transferring more energy per collision for a large electron-ion temperature differential, the reduction in the Rutherford cross section reduces the overall thermalization rate. We also see that electron-ion heating is less effective for lower densities (Fig. 4.4 left column vs. right column). This is due the associated reduction in the collision rate.

The interplay of these trends with the plasma expansion begs the question of what regime results in the most and least electron-ion heating? Ultimately low initial electron temperatures, high densities and large plasmas allow maximal heating from EICs. These conditions increase the collision rate and the time ($\sim \tau_{exp}$) before the density drops and collisions become negligible. In Fig. 4.4(b), electron-ion thermalization contributes about 0.5 K and doubles the ion temperature at later times. For the opposite extreme of the accessible regime of these parameters in UNPs, the effect is very small, like in Fig. 4.4(e).

We can now revisit the early estimates of total ion heating due to EICs that we saw in Sec. 3.5. Ion temperatures, calculated at $t = \tau_{exp}$ have been plotted in Fig. 4.9 without electron ion heating and in Fig. 4.10 with electron ion heating. For these plots we have used the typical plasma size of $\sigma_0 = 1\,\text{mm}$. Notice how electron-ion heating is most significant at low T_e and high n.

4.0.6 Evolution of Γ_i

One major motivation of this study is to set the stage for future studies on techniques to achieve higher coupling of the ion species. We know that adiabatic expansion is

predicted to increase coupling strength but do we see this experimentally? Does the extra ion heat effect potential coupling strengths? What parameters yield the best increase in Γ_i?

In Ref. [74] it was predicted that expansion of the plasma will increase Γ_i and that this increase in Γ_i accurately reflects the corresponding pair correlation function up to $\Gamma_i \approx 10$. At this point the correlations essentially freeze out as the time-scale for their evolution is decreased relative to the expansion time scale. This reversal of time scales represents a violation of the Bogoliubov condition and open Pandora's box for interesting studies. Ref. [74] shows that although calculated value of Γ_i continues to increase further, it is no longer reflective of correlations within the ions or their thermodynamic properties.

With measurements of ion temperature and density evolution it is possible to calculate the evolution of Γ_i, the results are shown in Fig. 4.11 for the same datasets that were presented in Fig. 4.4. Notice how DIH sets the initial Γ_i to somewhere within the range of 2-3 regardless of initial conditions. The decrease in coupling over the first τ_{exp} is due to EICs and any unaccounted for heat that drives the coupling parameter even lower. Expected simulation results are plotted as dashed lines, both with EICs and without. After a few τ_{exp} have transpired the coupling parameter typically starts to increase. Maximum values of $\Gamma_i = 6 \pm 1$ are found at $t = 3.5\tau_{exp}$ for a UNP with $T_e(0) = 80\,\mathrm{K}$, $n_0 = 1.3\,\mathrm{mm}$ and $\sigma_0 = 1\,\mathrm{mm}$. There is no reason to believe the coupling parameter does not keep increasing for any of these datasets. However at these very late times the dramatically decreased density results in very poor SNR, even with several hours of data accumulation at a single time point. Efforts to improve the collection efficiency of the imaging system could prove useful in this case. Otherwise extended data collection times are the brute force solution to

searching for higher Γ_i.

Expected evolution of Γ_i can be explored more fully using results from the full numerical model. Fig. 4.12 shows the expected Γ_i without including electron-ion collisions. The increase in coupling for higher density and lower T_e reflects the equilibrium Γ_i as plotted in Fig. 3.8. The inclusion of electron-ion collisions greatly changes the landscape of the coupling parameter as shown in Fig. 4.13. Notice how there is now an optimum density of $1 \times 10^{14}\,\mathrm{m}^{-3}$ to $1 \times 10^{15}\,\mathrm{m}^{-3}$, dependent on electron temperature, that results in maximum ion coupling. At higher densities, electron-ion heating limits the ion coupling strength. At later expansion times, the most significant difference is further suppression of coupling at the highest densities due to electron-ion heating (see Fig. 4.14 for $t = 2\tau_{exp}$ and Fig. 4.15 for $t = 4\tau_{exp}$). This is due to a longer time for effective electron-ion heating before the dropping densities effectively turn off collisions. This quenching of electron-ion heating due to expansion also explains why larger, slower clouds (see Fig. 4.16) have a lower optimal density then smaller, faster clouds (see Fig. 4.17).

Reference [112] offers an intriguing discussion on the effects of strong electron shielding on the coupling parameter and even questions it's usefulness within the regime of $\kappa \geq 1$. For the regimes studied within this work, $0.15 \leq \kappa \leq 0.5$, the traditional Γ_i should be a reasonable parameter. Ultracold neutral plasmas provide yet another opportunity to study interesting crossover physics.

Some references mention a shielded coupling parameter, which includes a Yukawa like softening of the interparticle potential via the following expression,

$$\tilde{\Gamma}_i = \frac{1}{4\pi\varepsilon_0}\frac{e^2 e^{-\kappa}}{a_{ws} k_B T_i}. \tag{4.27}$$

However this expression is not accurate in the weakly coupled limit. [112] Nonetheless the value is plotted along with it's predicted evolution for illustrative purposes.

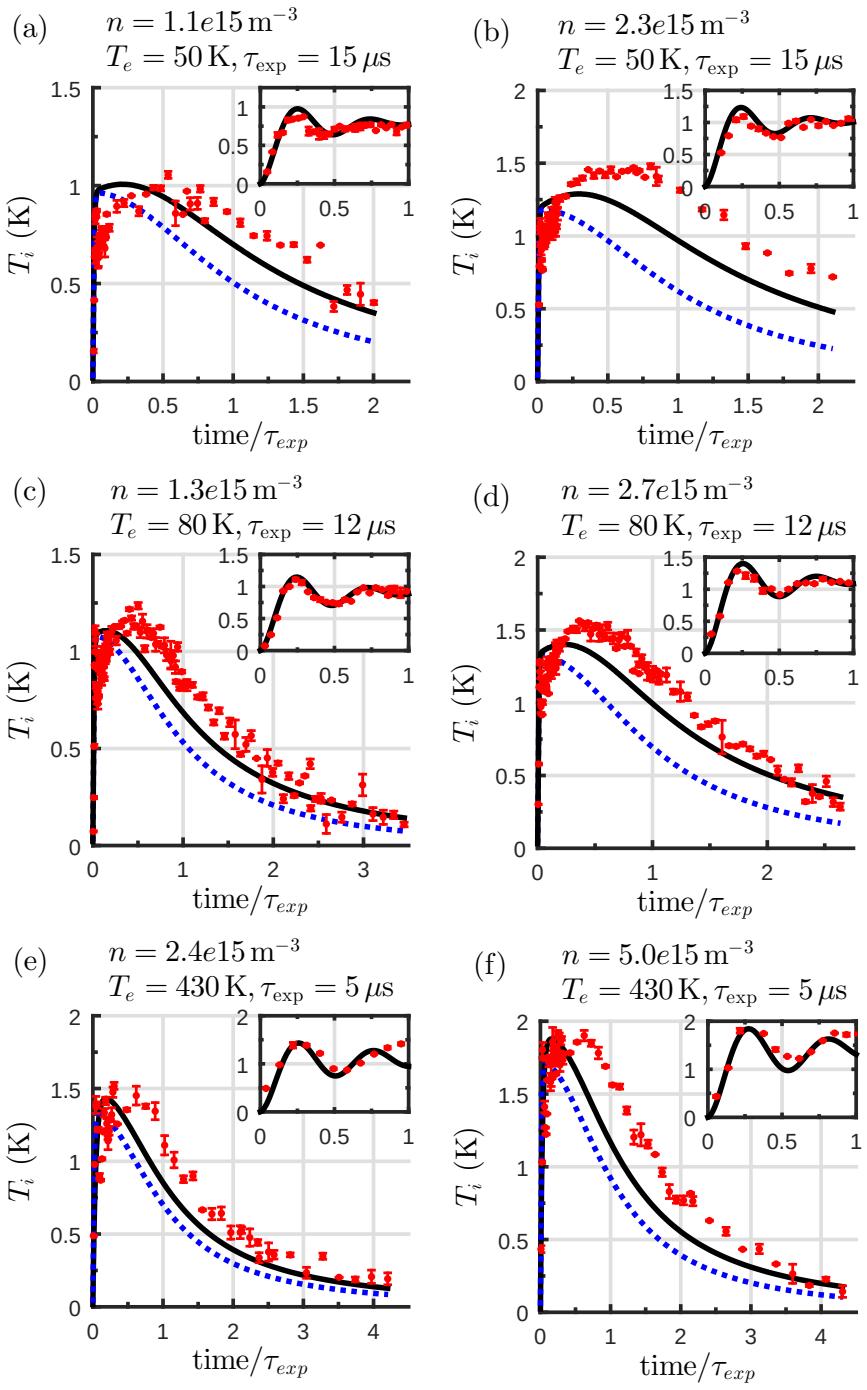

Figure 4.4 : Experimental ion temperature measurements compared to numerical models of UNP dynamics. Dashed lines are results of 4.8 through 4.12 and clearly miss a significant amount of energy when compared to experimental data points. The solid lines represent the inclusion of electron ion collisional heating (solution to Eqns.4.22 through 4.26) and clearly do a better job describing data across all regimes. The insets show fits of early time data fit to MD simulations which are used to determine density.

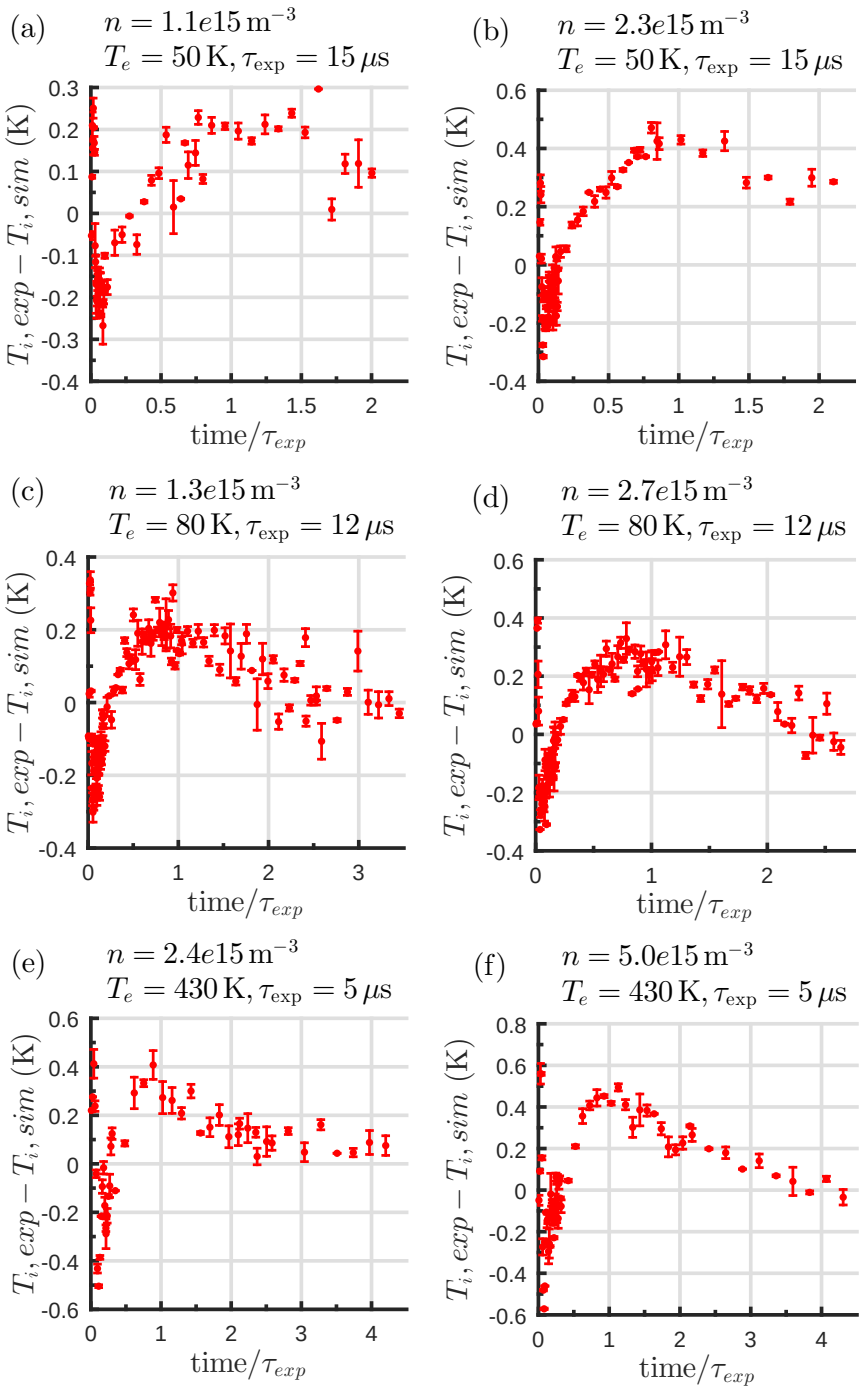

Figure 4.5 : Excess temperature observed in the ions when compared to full numerical model, Eqns.4.22 through 4.26. Discrepancies on the order of 200 mK to 400 mK are typical. Higher density seems to increase the extra energy.

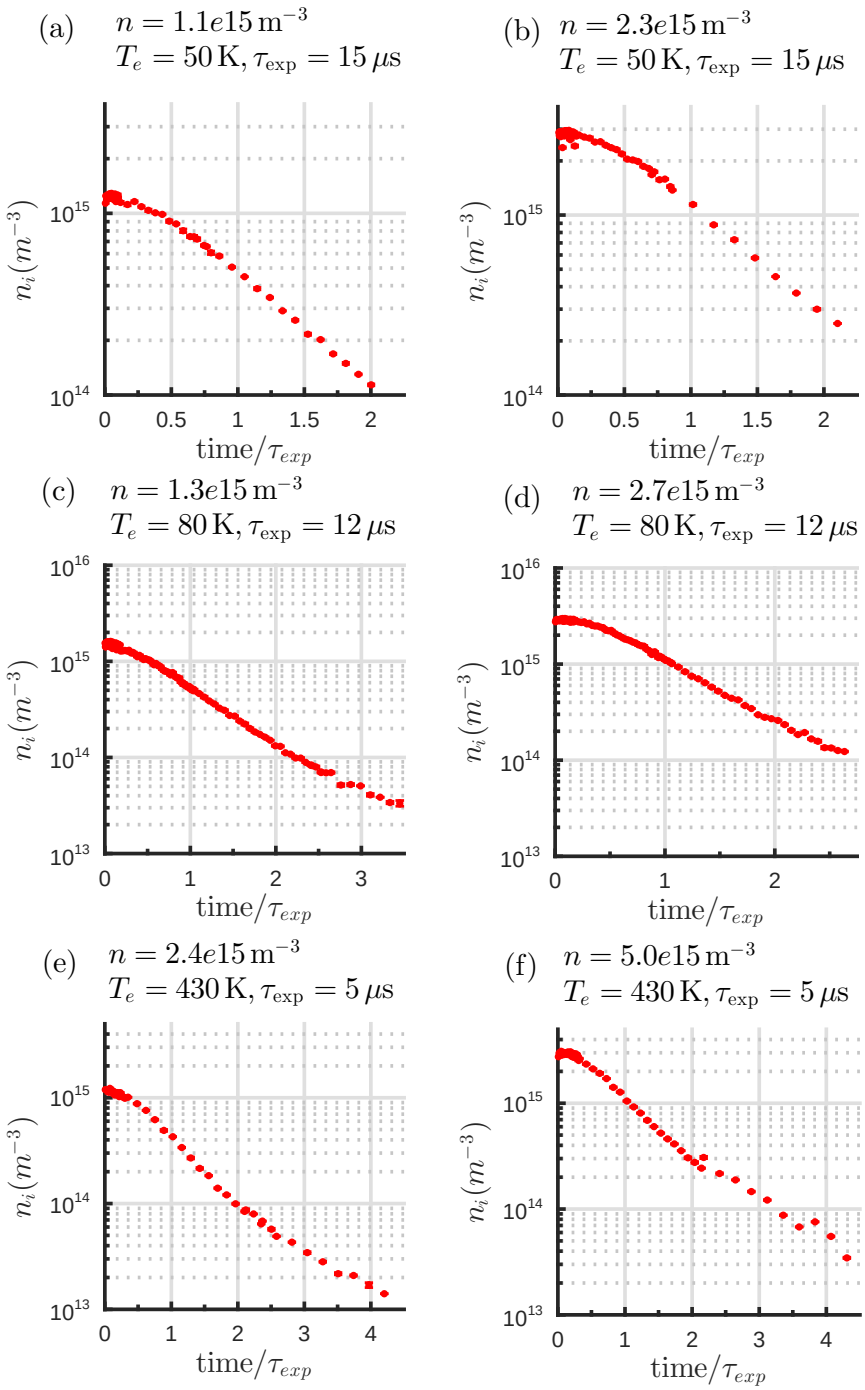

Figure 4.6 : Measured density evolution for data presented in Fig. 4.4. Within a few expansion timescales, densities plummet by orders of magnitude, to levels which begin to become experimentally challenging, i.e. $n_i < 10^{13}$ m^{-3}.

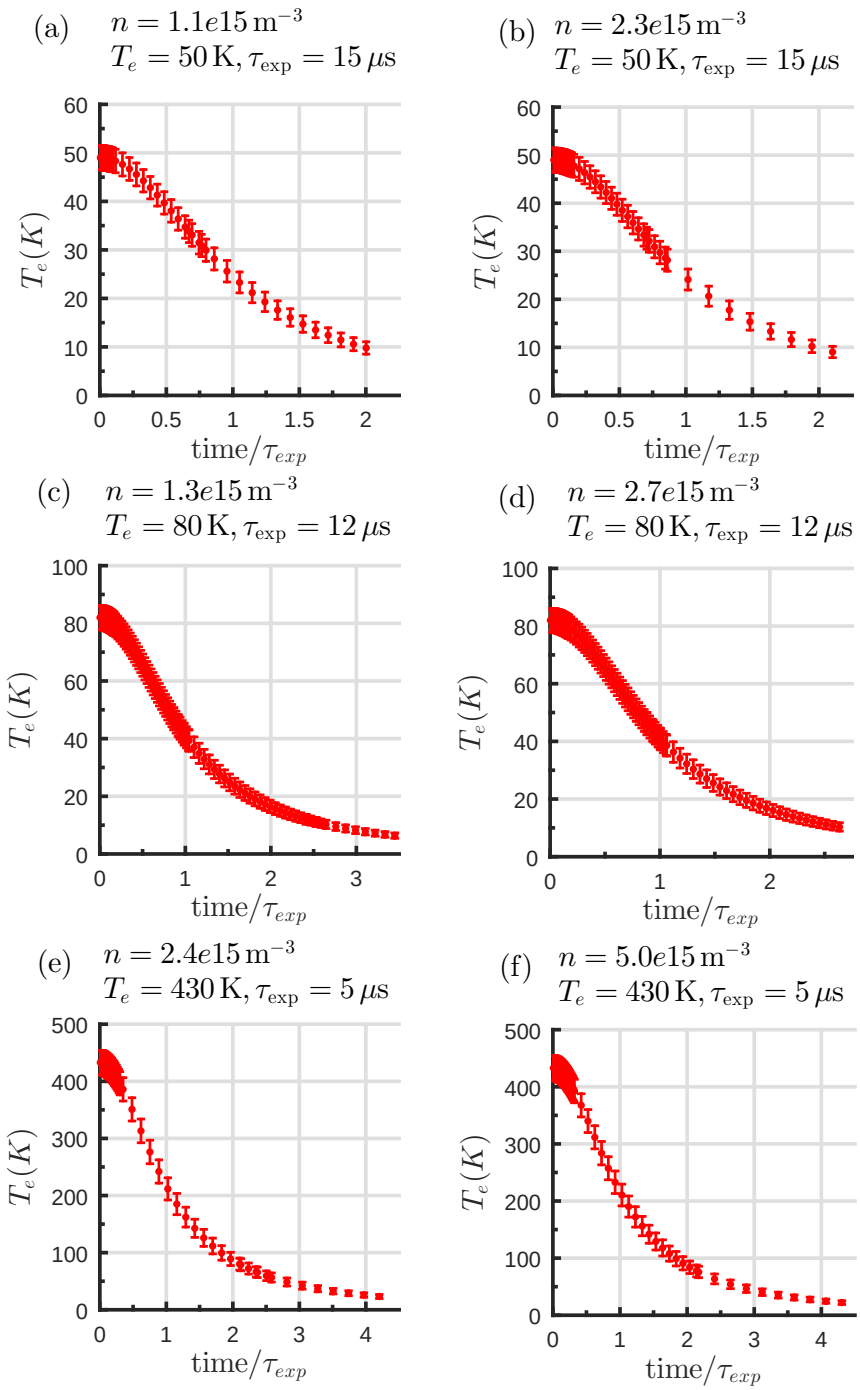

Figure 4.7 : Calculated electron temperature evolution for data presented in Fig. 4.4.

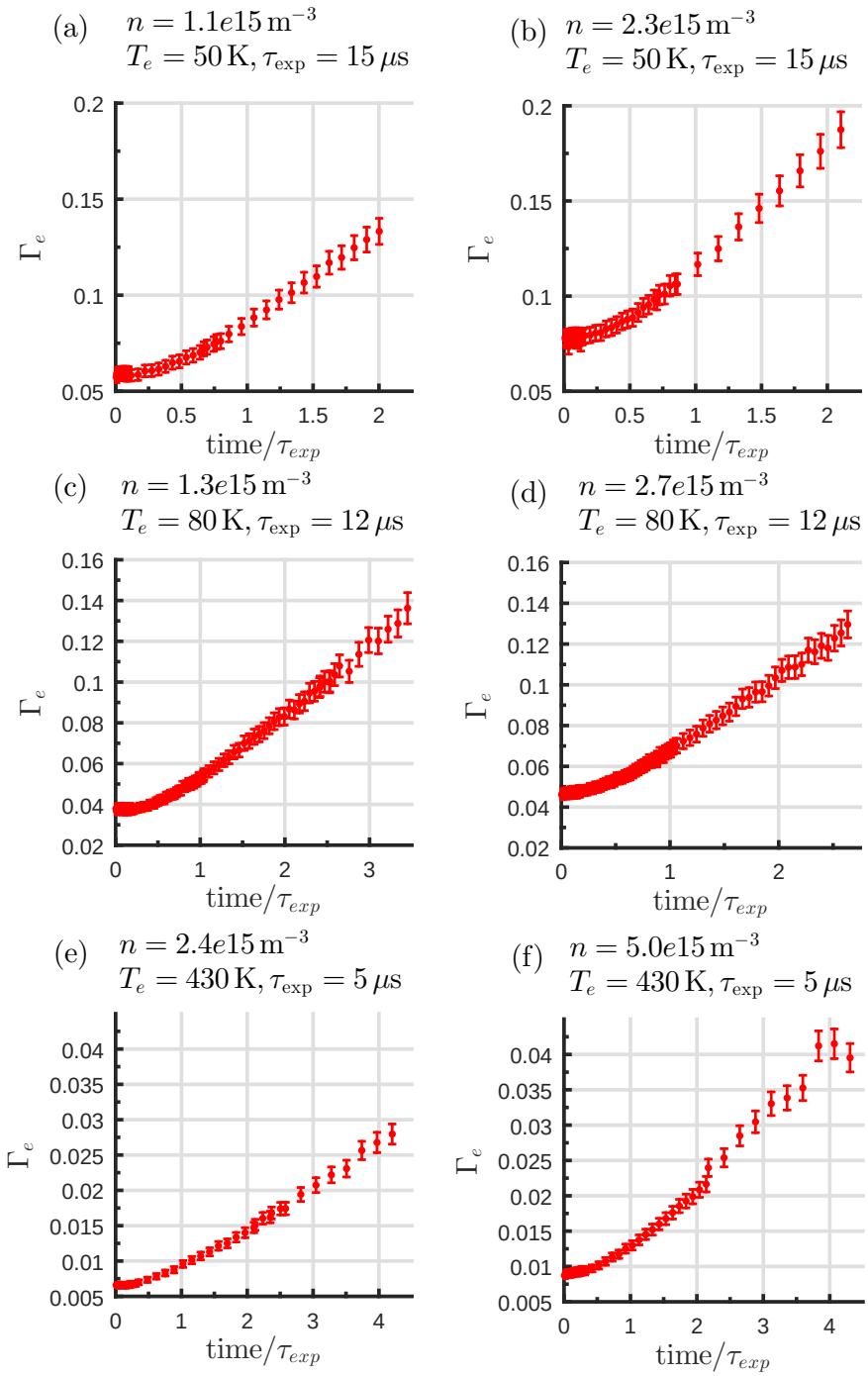

Figure 4.8 : Calculated Γ_e for data presented in Fig. 4.4. Both strongly coupled regimes (top row) and weakly coupled regimes (bottom row) are easily accessible through experimental studies of UNPs. The results do not represent either limit of accessible values for Γ_e

.

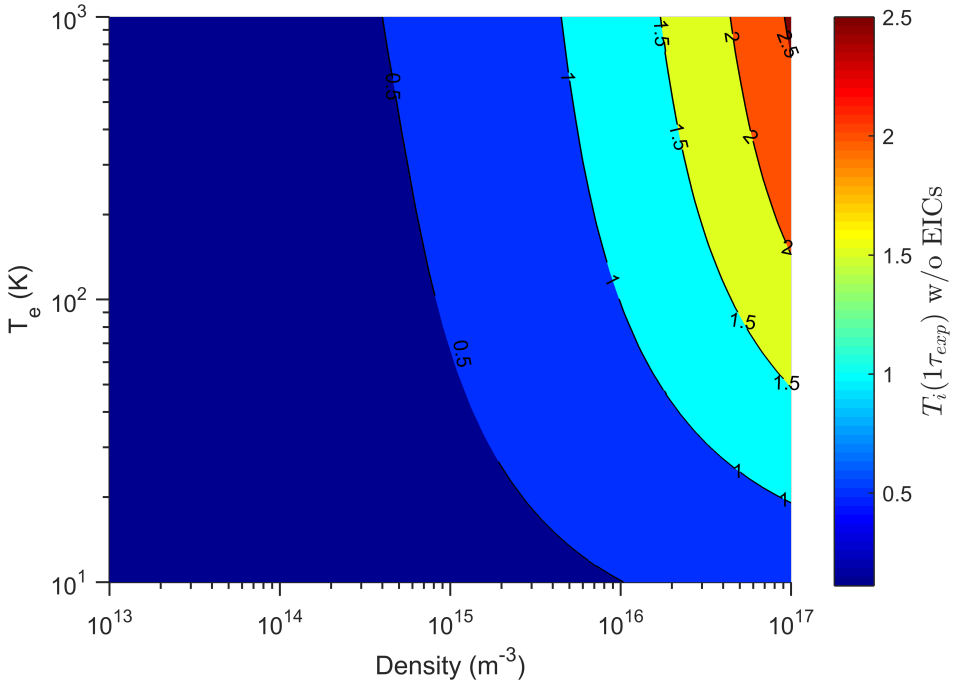

Figure 4.9 : Calculated ion temperature values after the first τ_{exp}, without electron-ion thermalization, i.e. Eqns. 4.22 through 4.26 without the EIC term, $\frac{T_e(t)-T_i(t)}{\tau_{EIC}}$.

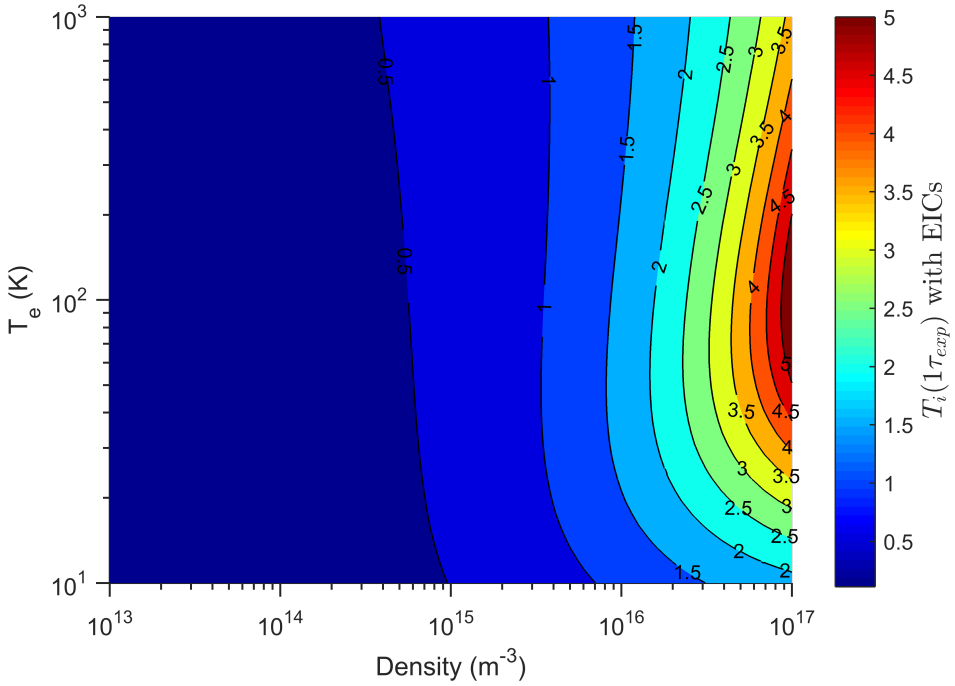

Figure 4.10 : Calculated ion temperature values after the first τ_{exp}, with electron-ion thermalization, i.e. Eqns. 4.22 through 4.26.

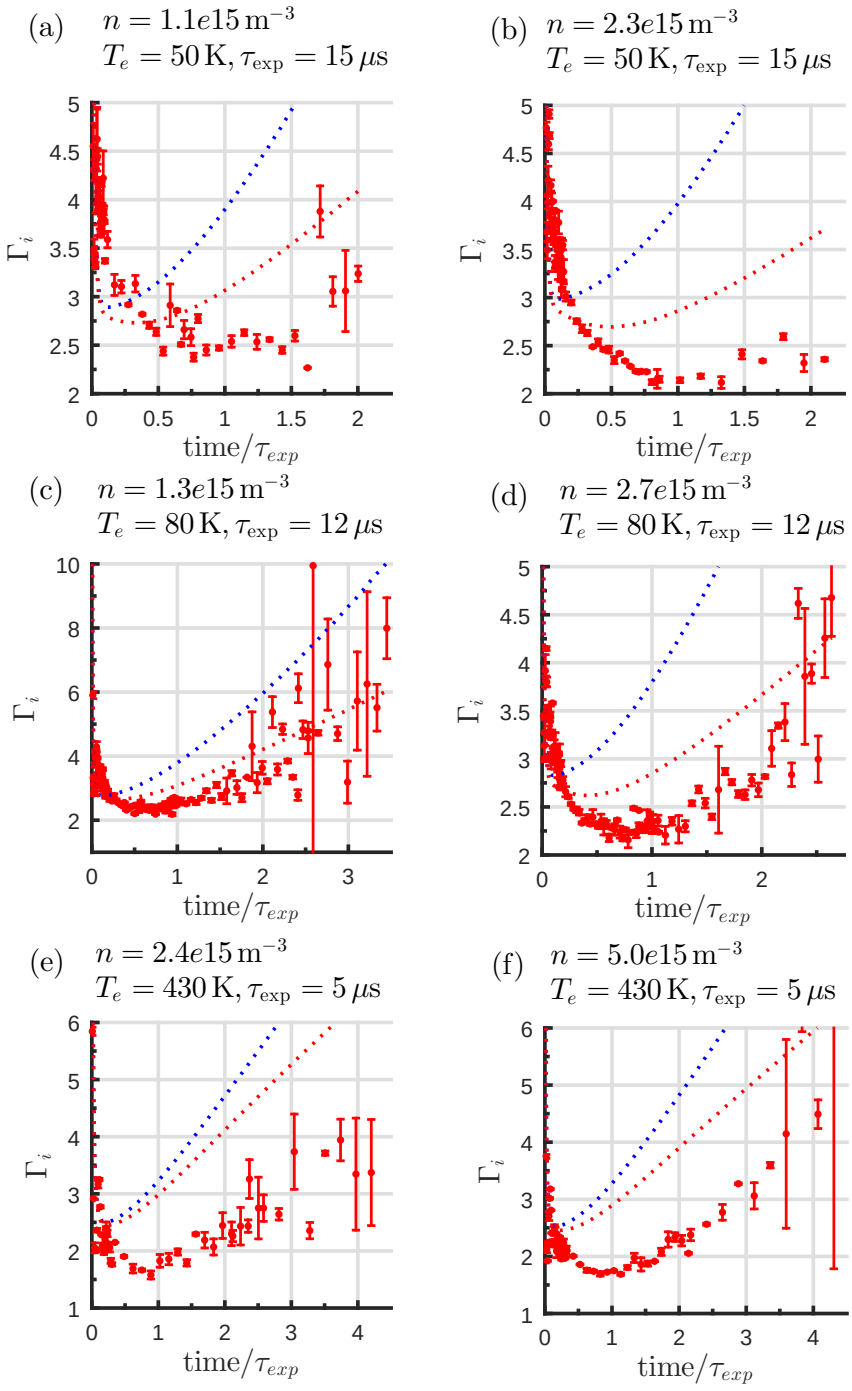

Figure 4.11 : Calculated Γ_i for data presented in Fig. 4.4. Dashed lines show expected evolutions calculated with and without EICs, (red and blue dashed line, respectively) The remaining discrepancy from experimental values is attributed to extra ion heating unaccounted for in our model.

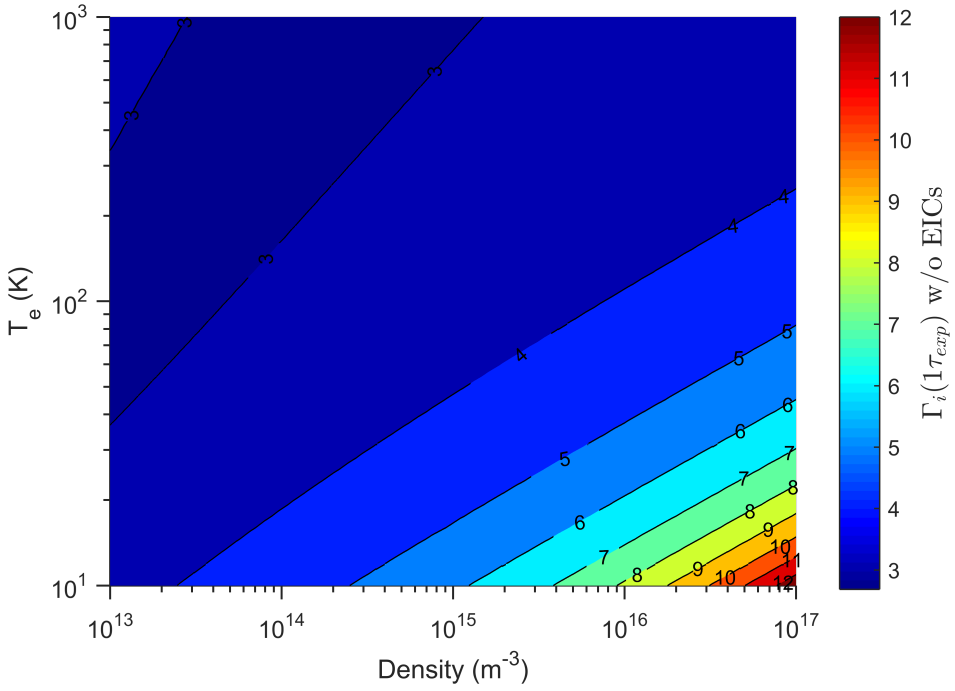

Figure 4.12 : Ion coupling parameter values after the first τ_{exp}. Results are calculated via Eqns. 4.22 through 4.26 without the EIC term, $\frac{T_e(t)-T_i(t)}{\tau_{EIC}}$.

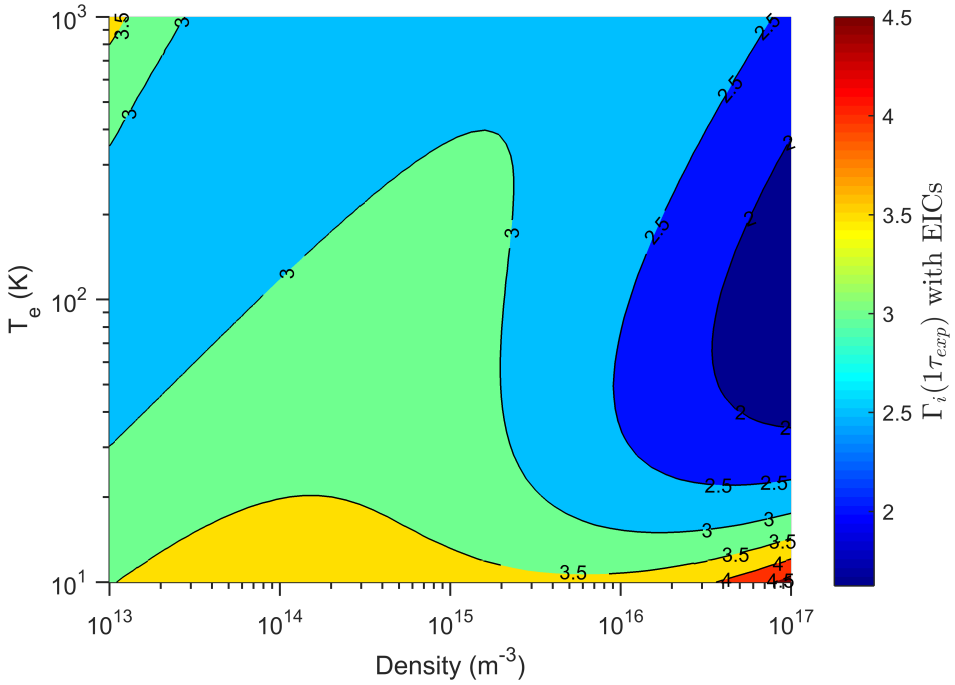

Figure 4.13 : Ion coupling parameter values after the first τ_{exp}. Results are calculated via Eqns. 4.22 through 4.26. The optimal density is a result of suppressed coupling due to electron-ion heating at higher densities.

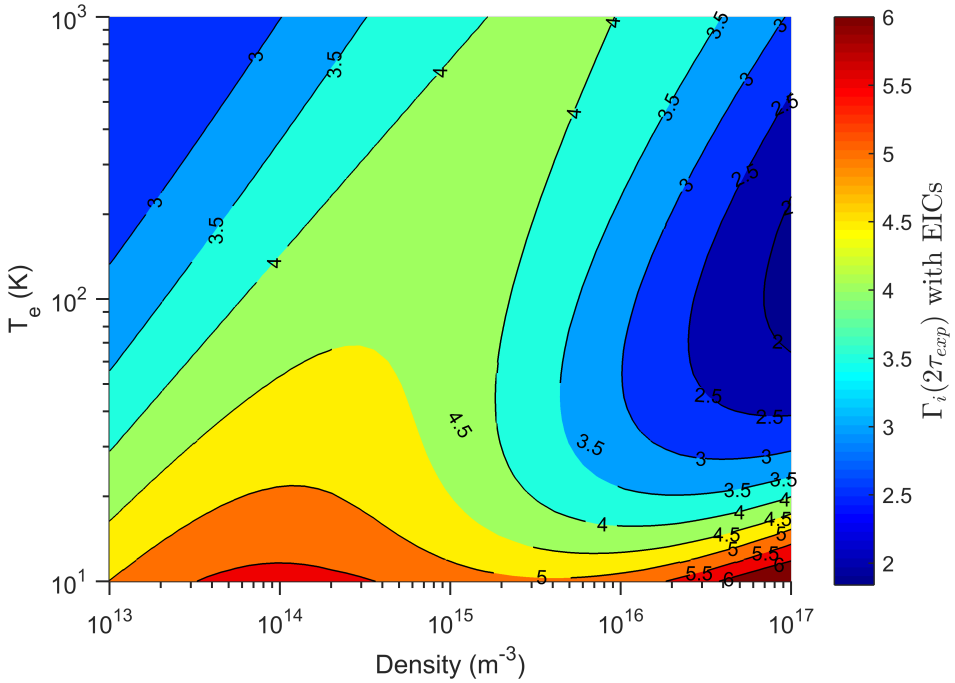

Figure 4.14 : Ion coupling parameter values at $t = 2\tau_{exp}$. Further suppression is visible at the highest densities. High initial density results in longer timescales for electron-ion heating before dropping densities quench collisions.

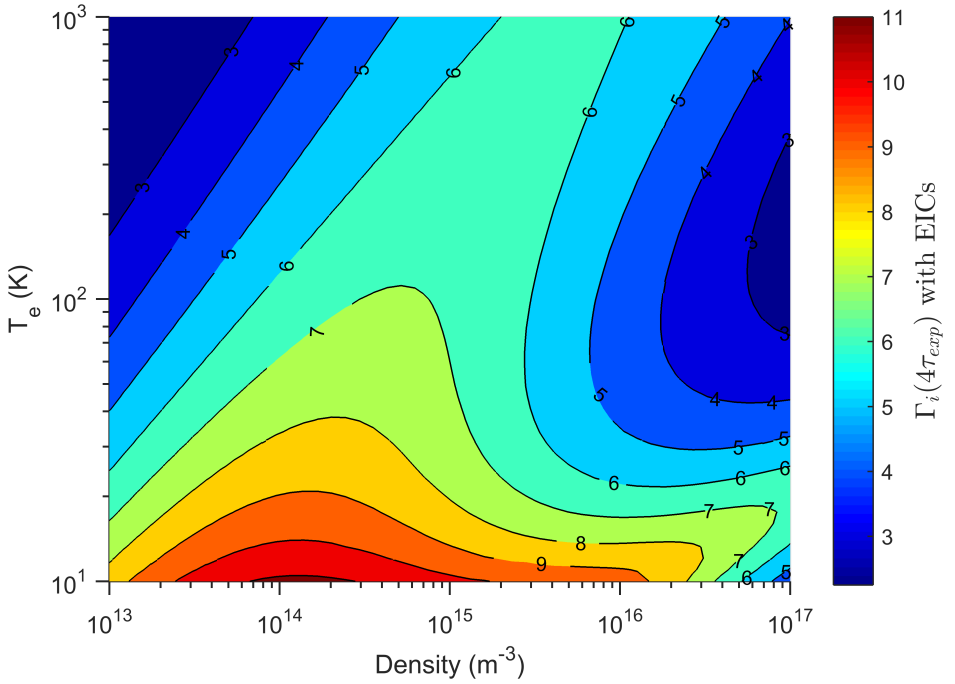

Figure 4.15 : Ion coupling parameter values at $t = 4\tau_{exp}$.

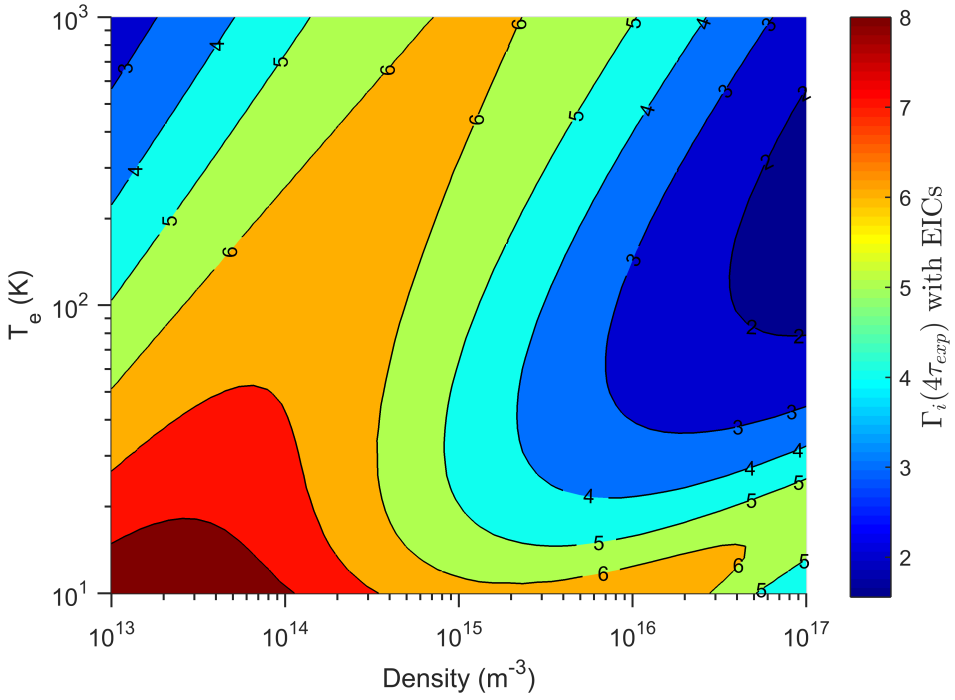

Figure 4.16 : Ion coupling parameter values at $t = 4\tau_{exp}$ for 2 mm cloud.

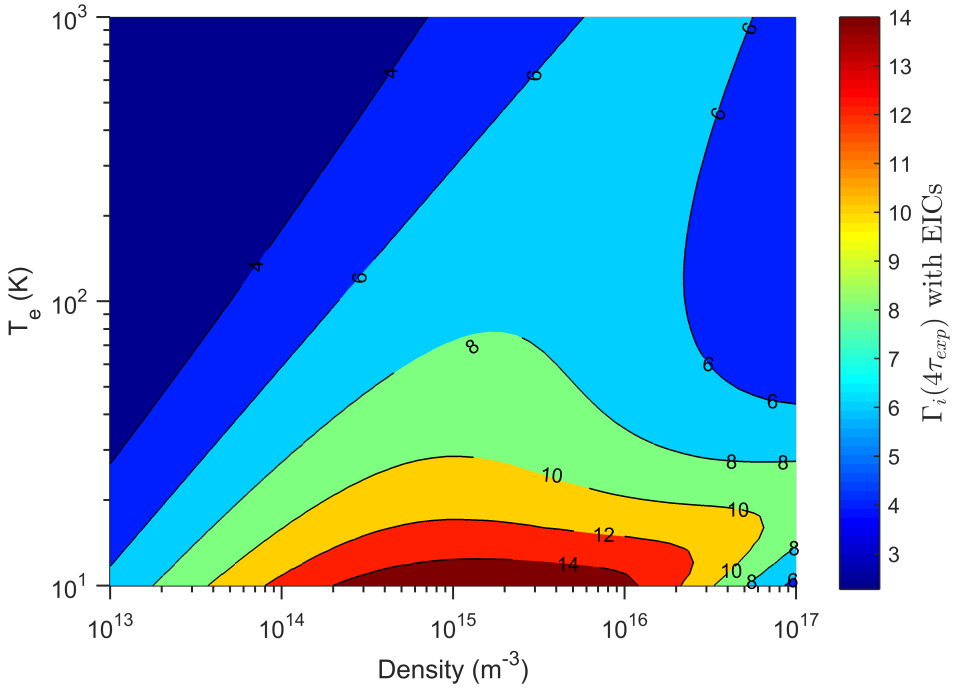

Figure 4.17 : Ion coupling parameter values at $t = 4\tau_{exp}$ for 0.5 mm cloud.

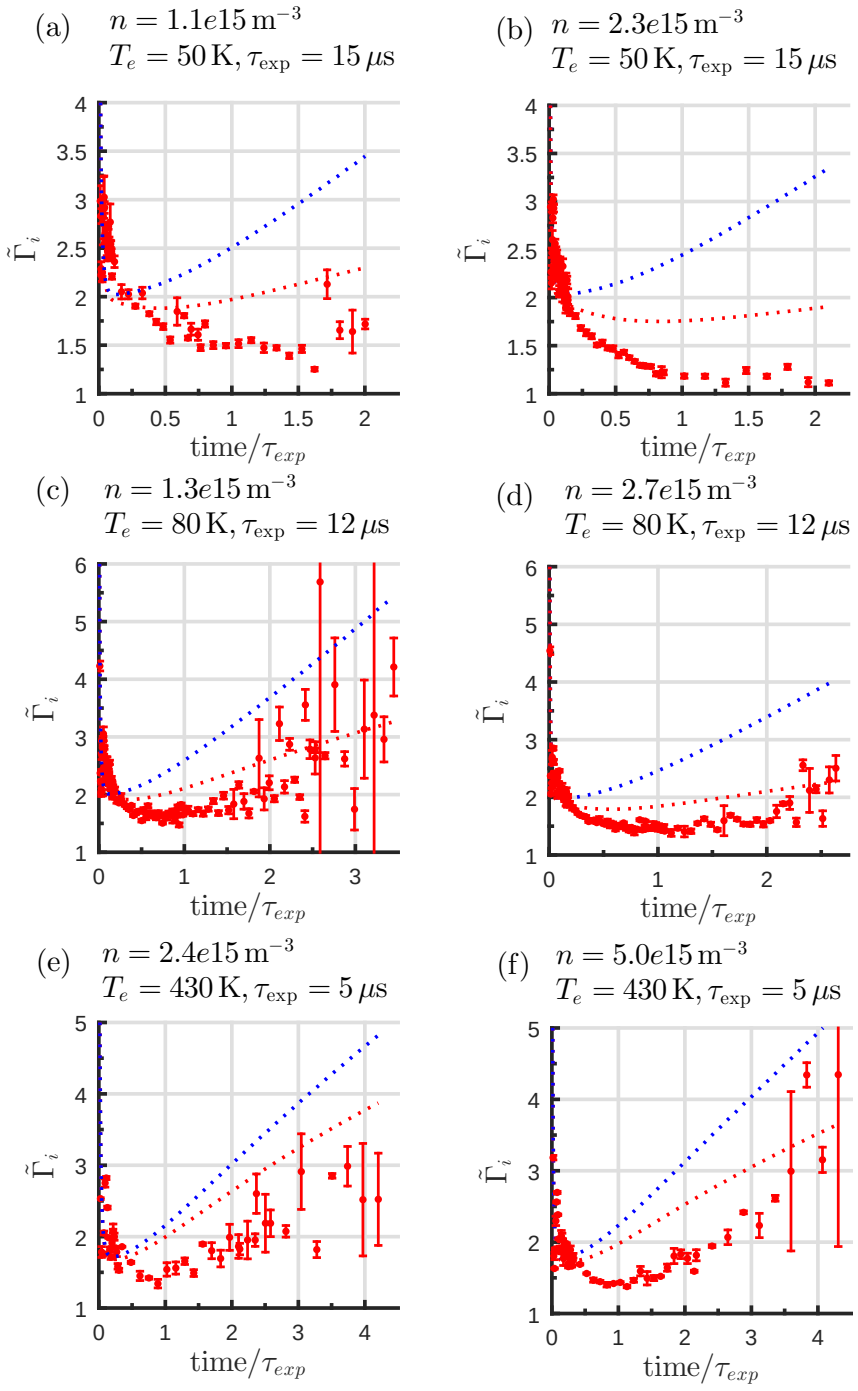

Figure 4.18 : Calculated $\tilde{\Gamma}_i$ for data presented in Fig. 4.4. Dashed lines show expected evolutions calculated with and without EICs, (red and blue dashed line, respectively) The remaining discrepancy from experimental values is attributed to extra ion heating unaccounted for in our model.

4.1 Calibrating Density with Ion Temperature Evolution

In Sec. 2.4.1 methods for calibrating density measured with fluorescence against absorption measurements were discussed. It was shown how the technique inevitably involves assumptions regarding the size/shape of the plasma and imaging beam and therefore can easily suffer from significant systematic uncertainty. With a better understanding of ion dynamics we can now perform density calibration based off the ion temperature evolution. The main advantages of this approach are that calibration can be performed concurrently with data collection, i.e. no more switching from fluorescence to absorption imaging. The calibration is accomplished only on the illuminated volume of plasma and thus size/shape assumptions can be avoided by using sheet fluorescence. Ultimately this results in faster and more accurate results. However one must be very careful to avoid plasma effects or analysis techniques that can effect temperature measurements (i.e. anomalous heating). We must also be mindful of the lack of thermal equilibrium since strictly speaking the ions do not have a well-defined temperature at this early stage. These caveats will be discussed in the following sections.

4.1.1 Regional Density compared to T_{DIH}

Historically the equilibrium DIH temperature was considered the most robust means of measuring or calibrating density since its magnitude depends primarily on density (albeit weakly, i.e. $T_{DIH} \propto n^{1/3}$) and secondarily on electron temperature (which is well known in our experiments). While technically true, there were aspects of the thermalization that were unknown until recently. It was thought that kinetic energy oscillations represented oscillations about the equilibrium value, however detailed molecular dynamics simulations show that both ion RMS kinetic energy and

measurements via Voigt profile fitting are typically lower then the DIH equilibrium temperature until the oscillations have completely damped, with the exception of the first peak which typically overshoots by about 10%. This initial stage of UNP evolution is very complex as the system evolves between states of very high potential energy/minimal correlations and maximum correlations, thus this quality of the oscillations is not obvious *a priori*. However it is clearly demonstrated in Fig. 4.19 from Ref. [2], in which it is evident the peaks of the oscillations skim the equilibrium value. Similar qualitative results are seen in experiments with UNP ions, see Fig. 4.1.

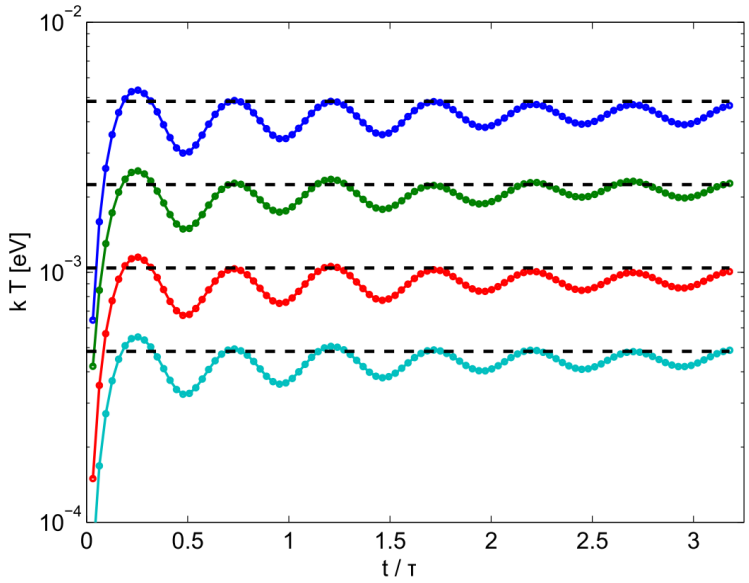

Figure 4.19 : Kinetic energy oscillations in RMS from tree code simulations of equilibrating zero temperature electrons show that electron temperatures oscillate such that the equilibrium temperature (shown by dashed line) skims the top of the KEOs. $\rho_i = 1 \times 10^{20}\,\mathrm{m}^{-3}$, $1 \times 10^{19}\,\mathrm{m}^{-3}$, $1 \times 10^{18}\,\mathrm{m}^{-3}$ and $1 \times 10^{17}\,\mathrm{m}^{-3}$ (from top to bottom). Notice how the lack of a screening species qualitatively effects the dynamics. Copied from [2]

Another caveat exposed by molecular dynamics simulations is that the method

of fitting spectra to Voigt profiles underestimates the true RMS spread in velocities, see Fig. 4.20. This is due to the lack of thermal equilibrium which the Voigt profile assumes. As shown in the lower portion of Fig. 4.20 high energy ions in the wing of the distribution are not well described by Voigt profile fits and result in effective temperatures which do not accurately reflect the RMS kinetic energy.

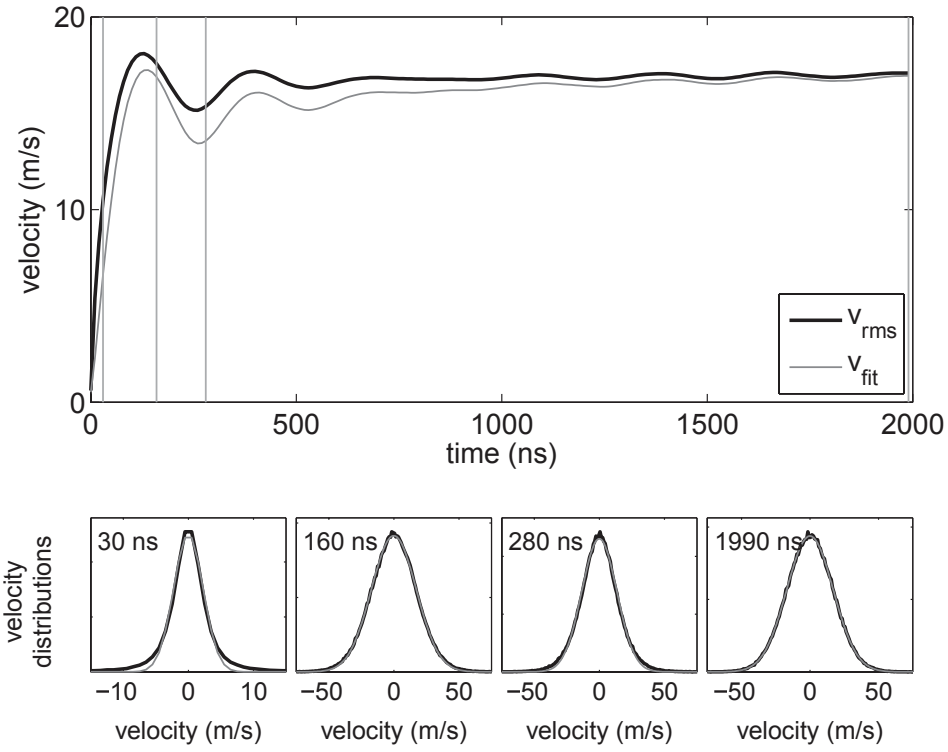

Figure 4.20 : Molecular dynamics simulation of disorder induced heating for an UNP with $n_i = 4e16$ m^{-3} and $T_e = 60$ K. The dark grey line represents the true rms spread of ion velocities while the grey line is a fit to the velocity distribution using a Voigt profile. The discrepancy between the two can be attributed to the fact the ions are not in thermal equilibrium. The lower panes show details of the velocity distribution at four time points indicated by vertical grey lines in the upper panel. The actual velocity distributions are shown in black and corresponding Voigt fits in grey, notice the deviations in the wings due to high energy ions, particularly before the DIH peak and during the subsequent troughs of the KEOs. Copied from [3])

4.1.2 Determining Regional Density from Kinetic Energy Oscillation Frequency, $2\omega_{KEO}$

Another possible technique for calibration is to exploit the oscillation frequency of kinetic energy oscillations. Frequency based calibration offers several advantages. Determining the absolute value of the kinetic energy requires assumptions about the proper fitting function for the ion velocity distribution function and a calibration of the laser detuning control voltage, inevitably introducing uncertainty. However, the timescale of relative changes in temperature can be determined without such assumptions and therefore the time scale of any oscillation is calibration insensitive. Also, time is perhaps the most precise experimental parameter we have. Since the experiment is now triggered by an external clock, t_0 is absolutely stable to 10 ns, see Sec. D.2.1 for more detail.

Upon creation, ion temperatures soar from 7 mK to about 1 K and then oscillate for a few cycles. Without electron shielding this frequency is simply twice the ion plasma oscillation frequency, or equivalently the initial rapid heating time is one quarter period of a ion plasma oscillation. With reliable 1 ns resolution this frequency can be accurately measured and related back to the initial density through the ion plasma frequency,

$$\omega_{pi}(t) = \sqrt{\frac{n(t)e^2}{m_i\epsilon_0}}. \tag{4.28}$$

We did not use this calibration method extensively because we acquired the MD simulations, which offer a complete description of KEO dynamics. However comparison with ω_{pi} offers a fast and simply method of calibration that can be performed with live images (i.e. without taking full spectra or any post-processing). Assuming a constant density, any increase in spectral width necessarily lowers the on resonance

signal. By observing the on-resonance signal level and stepping through early plasma evolution one could quickly determine the time between t_0 and the first peak in temperature (first minimum in on resonant signal) at τ_{DIH}. Then τ_{DIH} can be relate to a density via Eqn. 3.7 or Eqn. 3.8, as appropriate. Dialing in a certain density is a task faced by the experimenter quite often, this technique offers a quick and reliable method to do so.

4.1.3 Fitting KEOs to MD Simulation Results

These preceding ideas were only briefly explored since soon thereafter we acquired results from MD simulations of equilibrating homogeneous one-component Yukawa plasmas, which allow full comparison to experimental equilibration data. This allows fitting of early time temperature evolution to a plasma density with about 5% uncertainty, see figure 4.2. Further details from a full characterization of this technique are to be published in the near future.

Chapter 5

Anomalous Heating

5.1 Introduction

Despite numerous improvements in the measurement techniques and models for ion temperature evolution, there appears to still be extra ion energy which is not described by the model described thus far (e.g. see Fig. 4.4). The extra energy is typically on order of a few hundred millikelvin and appears at or about $t = \tau_{exp}$. There are numerous potential sources that can be considered. Perhaps the measurement is incorrectly interpreting expansion energy as thermal energy, (Sec. 5.2) or perhaps there is additional energy unaccounted for in the present model, (Sec. 5.3).

5.2 Mixing of Expansion Velocity

The technique for measuring the ion temperature relies on the ability to analyze a region of the plasma over which the Doppler shift due to bulk velocity is constant. Otherwise variation in the bulk velocity within the region will be misinterpreted as thermal motion resulting in broadening of the spectra, which leads to higher temperature measurements. This could happen if the region size is too big, camera gatewidth is too long or if our imaging system does not have sufficient resolution.

5.2.1 Region Size and Camera Gatewidth Effects

Recall that bulk velocity is described by $\mathbf{v}(\mathbf{r}, t) = \gamma(t)\mathbf{r}$. By virtue of the Doppler shift we are only sensitive to component of velocity parallel to the fluorescence beam's k-vector. Which in this work is the $\hat{x}$-component, i.e. $v_x(x, t) = \gamma(t) * x$, with $\hat{x}$ defined as parallel to the imaging beam's k-vector. We see that in order to minimize the spread in bulk velocity within a region we need to minimize it's size in the $\hat{x}$ direction but there are no explicit limitations for the $\hat{y}$ direction. The functional limitation on the size in $\hat{y}$ is related to study-specific tolerances for averaging over varying densities as well as deviations from the ideal expansion model due to non-Guassian distributions.

To approximate the effect of apparent heating due to expansion velocity, we consider how the local hydrodynamic velocity varies over a distance δx and during time δt (representing region width and camera gatewidth respectively). We start by taking the total derivative of the expansion velocity.

$$\mathrm{d}v_x(x, t) = x\frac{\partial\gamma(t)}{\partial t}\delta t + \gamma(t)\delta x, \tag{5.1}$$

where

$$\frac{\partial\gamma(t)}{\partial t} = \frac{1}{\tau^2\left(1 + \frac{t^2}{\tau^2}\right)} - \frac{2t^2}{\tau^4\left(1 + \frac{t^2}{\tau^2}\right)^2}. \tag{5.2}$$

The first term of Eqn. 5.1 reaches it's maximum value at $t = 0$, while the second term is zero at $t = 0$. The second term reaches it's maximum at $t = \tau$, at which the first term is zero. Therefore it suffices to consider each term independently.

We proceed with the first term of Eqn. 5.1 which represents broadening due to camera gatewidth. At $t = 0$ it reaches it's maximum value of $x\tau^{-2}\delta t$. For the work in this thesis, we analyzed a central region of the plasma with dimensions of 1 mm by 1 mm, thus the maximum $x = 0.5\,\mathrm{mm}$ and the smallest typical $\tau = 5\,\mu\mathrm{s}$. For a

typical short gatewidth of $\delta t = 100\,\mathrm{ns}$ we find $\mathrm{d}v_x(x,t) = 2\,\mathrm{m\,s^{-1}}$. Converting this to temperature units, i.e.

$$\Delta T_i = \frac{m_i}{k_B}(\mathrm{d}v_x)^2, \tag{5.3}$$

we calculate up to $\approx 40\,\mathrm{mK}$ of apparent heating. This is almost significant for typical plasma parameters and indicates that gatewidths should be no longer than 100 ns and that unless gatewidths are smaller, or τ_{exp} is longer, temperature measurements are only accurate within about $\pm$ 0.5 mm of the center of the cloud.

We now consider the second term of Eqn. 5.1, i.e. the broadening due to finite region size which maximizes at $t = \tau$ to a value of $(2\tau)^{-1}\delta x$. Again we use the minimum τ of 5 µs and a single pixel width of $\delta x = 13\,\mu\mathrm{m}$ which yields a maximum apparent heating of 18 mK. For these parameter, we find the effect to be practically negligible. However at only 1x magnification with 4x4 binning this can lead to broadening of $\approx$ 300 mK which is very significant compared to typical ion temperatures.

This estimated spread in bulk velocities within a region can be should be comparable to the difference in center frequencies of neighboring regions. For this analysis regions are one pixel wide in $\hat{x}$ (4x4 binning and 4x magnification gives pixel size of 13 µm) and 0.5 mm tall in $\hat{y}$, $T_e = 430\,\mathrm{K}$ and the characteristic radius is σ =0.9 mm, resulting in a $\tau_{exp} = 5\,\mu\mathrm{s}$. These parameters represent the fastest expansion we typically deal with and thus provide a good upper bound. The results show an average neighboring region frequency shift of about 2.7 MHz, see Fig. 5.1.

Relating the previously calculated velocity width due to region size to a frequency width through the Doppler shift

$$\Delta\nu = \Delta v_x/\lambda_{img} \tag{5.4}$$

we calculate a maximum 3 MHz shift in neighboring regions at $t = \tau_{exp}$.

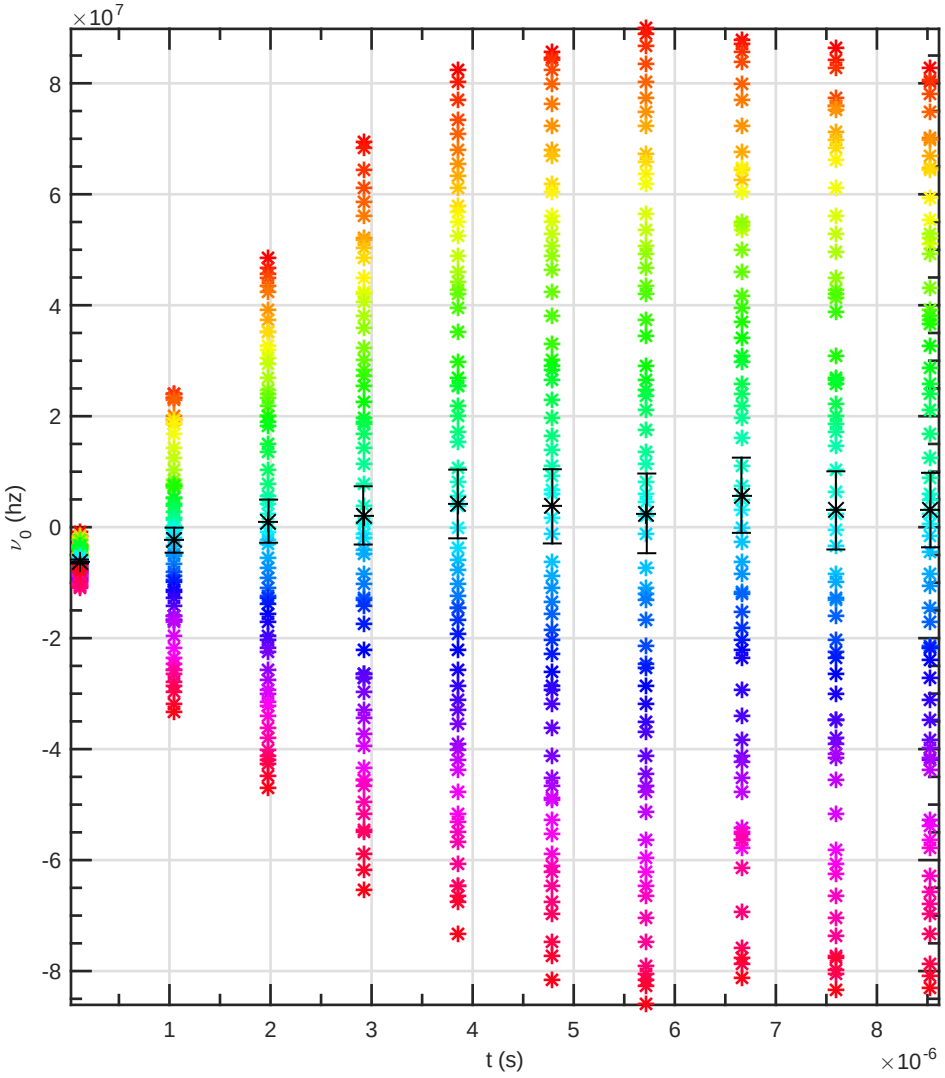

Figure 5.1 : Center frequencies of LIF spectra for neighboring regions in an UNP of T_e = 430 K and the characteristic radius is σ =0.9 mm. Average spacing is about 2.7 MHz for a single pixel region width of 13 µm

.

While a single pixel wide region offers the smallest broadening, it also results in the lowest SNR, which sometimes might not be acceptable. So what happens if we increase the region width more than a single pixel wide? The results are shown in

Fig. 5.2. As expected, wider regions result in higher measured temperatures, and the broadening is most significant at $t = \tau_{exp}$. At that time, 3 pixel wide regions results in 30 mK of broadening, 5 pixels wide regions results in 60 mK of broadening, 7 pixels wide regions results in 100 mK of broadening, and 15 pixels wide regions results in 300 mK of broadening. The measured broadenings are smaller then estimated above which is like a result of the Gaussian kernel used to collect regional information, i.e. the signal towards the edges of the region is downweighted compared to the central pixel.

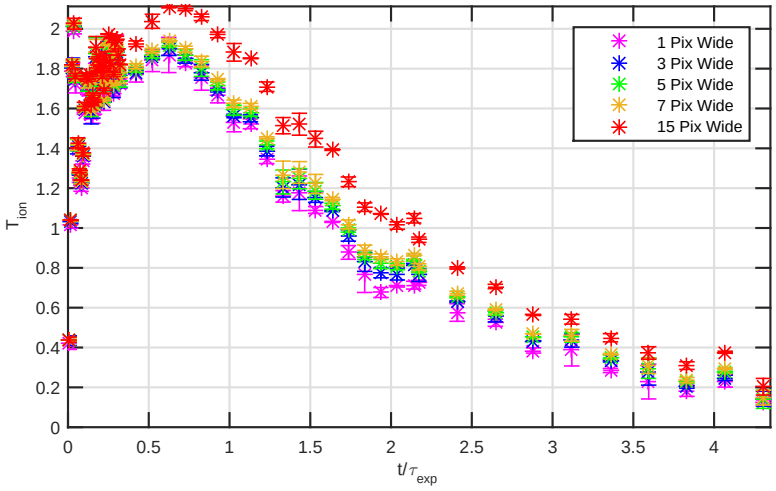

Figure 5.2 : Increasing the region width results in spectral broadening and higher measured temperatures. Here $T_e = 430\,\mathrm{K}$, $n_0 = 2 \times 10^{15}\,\mathrm{m}^{-3}$ and $\tau_{exp} = 5\,\mu\mathrm{s}$. These parameters represent the fastest expansion for our typical regime and thus reflect the greatest potential broadening.

.

5.2.2 Imaging System Resolution

Thus far we have assumed ideal resolution for our imaging system, however that's hardly the case for any real optical system. Though most CCD based cameras offer

100% contrast up the Nyquist frequency (one cycle equals two pixels), an ICCD has limitations imposed by the built in intensifier, that limit the minimum feature size to about 4 pixels, or $\sim 50\,\mu m$ for our camera (Princeton Instruments PI-MAX2). Comparatively, the imaging optics (relay and camera lenses) have demonstrated diffraction limited performance, i.e. sub-$6\,\mu m$ and will be considered ideal.

Sheet Fluorescence

Without a sheet-like truncation to the imaging beam we are sensitive to a variety of potential effects that obscure temperature measurements. For instance, restricting the fluorescence illumination volume restricts the volume over which the expansion needs to be well behaved. Without sheet fluorescence we are even more sensitive to non-ideal expansion due to any non-Guassian nature of the ion distribution. Furthermore signal is collected outside of the focal plane and experiences greater blurring than within the imaging plane. Overall these effects lead to grossly anomalous temperature measurements as seen in Fig. 5.3.

Magnification

By magnifying the signal spatially before it enters the ICCD, the relative size of the ICCD intrinsic blurring is reduced and region size broadendin should be reduced. Comparison scans were taken for similar UNPs at 1x and 4x magnification. The results are shown in Fig. 5.4 and clearly show increased temperatures in the case of 1x imaging.

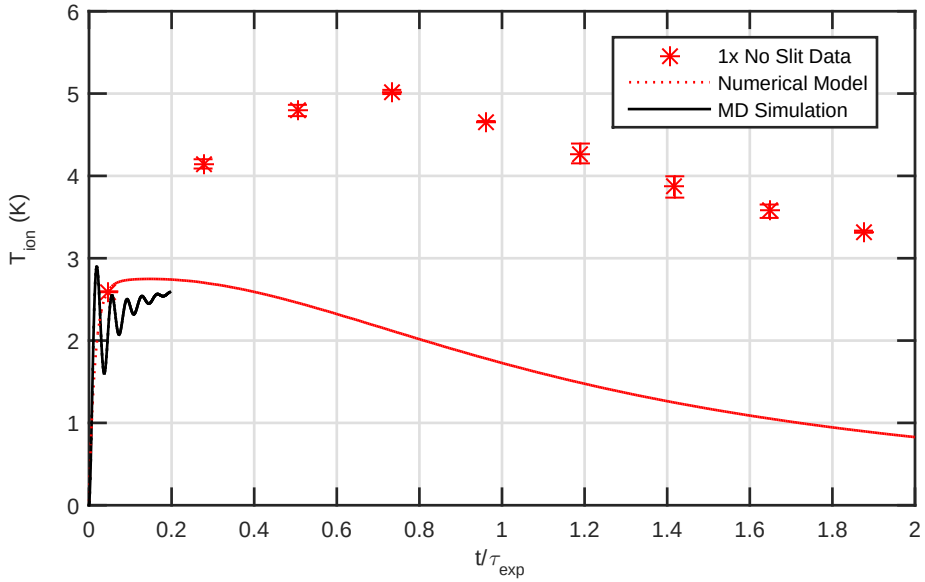

Figure 5.3 : Data taken at 1x magnification and without truncating the imaging beam into a thin sheet. Large temperature discrepancies on order 5 K are observed.

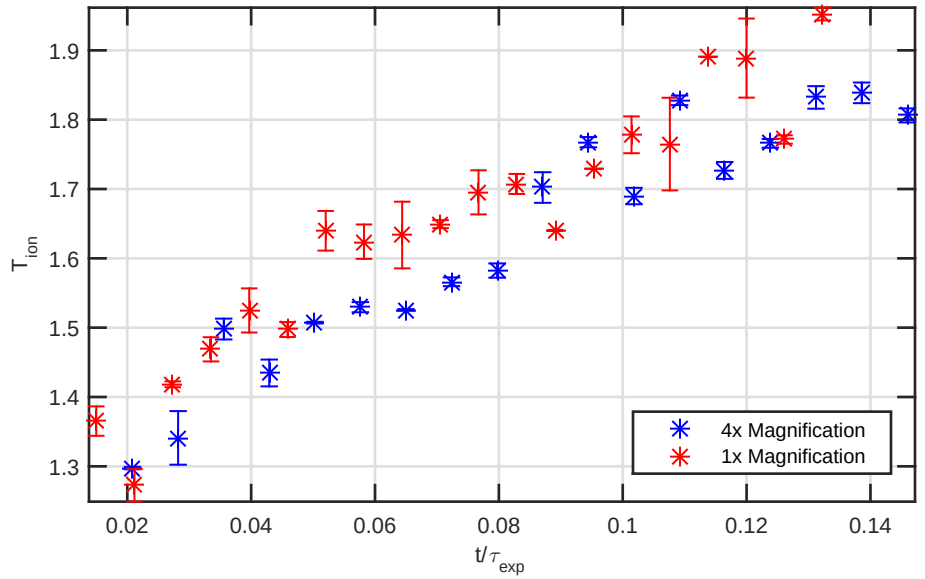

Figure 5.4 : Comparison of datasets for similar UNPs taken at different magnifications show extra heating in the case of non magnified images. Unfortunately the plasma does not evolve far in these scans but the difference is clear and repeatable. Presumably the discrepancy should increase as plasma expansion accelerates.

Point Spread Function

Typically characterization of blurring is accomplished by imaging a known simple geometric object. If the object is a point, a line or an edge, the resulting image is known as either a point, line or edge spread function (PSF, LSF or ESF). Of these, the PSF is the most fundamental and completely characterizes the imaging system performance. By thinking of any arbitrary image as a collection of blurred point sources it is evident how, with knowledge of the PSF, one can deconvolve the image to calculate the original object without blurring. This is a relatively standard digital image processing technique employed in satellite imaging and astronomy [137]. Strictly speaking, the PSF is a function of both the object space and image plane position, however, our imaging optics are practically aberration free and we limit the object space illumination region by truncating the imaging beam so that the PSF is considered constant over the field of view.

To measure the full resolution PSF we imaged (with 1x1 binning, yielding 13 µm pixel size) the output facet of a fiber optic (≈ 6 µm spot), which can be approximated as a point source (verified by imaging with 6 µm pixel size, Nyquist limited CCD). Assuming the PSF to be radially symmetrical it was post-processed in order to minimize the noise in the measurement. The peak pixel was defined as the origin and the image was averaged with numerous rotated versions of itself as well as mirrored images of the rotations. Rotations were from 0° to 360° with 0.1° increments. The PSF is then normalized so that the 2D integral of itself is identical to unity. The end result is shown in Fig. 5.2.2. The center pixel contains only about 10% of the signal, while about 5% blurs into each of pixels to the top bottom left and right, and about 2% blurs into diagonally neighboring pixels. The extreme corners of the image (outside the extent of the signal) average to zero as expected.

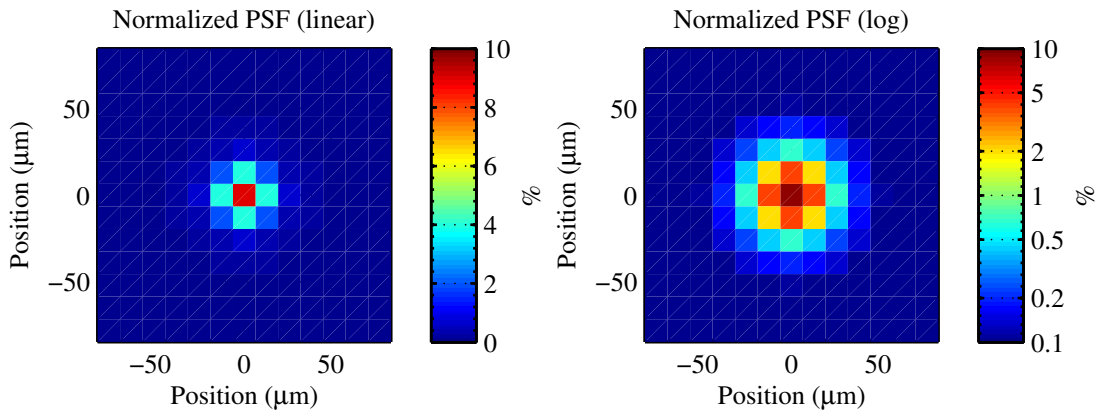

Figure 5.5 : Central peak of experimentally obtained and post processed PI-MAX2 ICCD's PSF.

To see details of the PSF which are obscured by a full-range colormap we plot the signal versus radius on a log plot, see Fig. 5.2.2, in which we present both filtered and unfilter signals. Here, the signal is normalized differently, i.e. the peak value is one. The extent of the PSF can be seen much clearer.

Although it is sharply peaked, i.e. 5 pixels away from center contains less than 0.1% of the signal, there is still measurable signal of about 0.01% at over 20 pixels away! The absolute extent of discernible signal spreads over ± 100 pixels at the 0.003 % level, that's ± 1.3 mm! This is evident by scaling the colorbar to see signal at the 0.001% level as in Fig. 5.7. We have already seen how mixing velocities of over just a few pixels can result in dramatic broadening and effective heating of 100s of mK thus this unavoidable blurring is potentially a concern.

In order to extract only the useful signal from the measurement the PSF is truncated at ± 128 pixels (as in Fig. 5.7) and windowed. We use a 2D Tunkey window which is shown in Fig. 5.8. Windowing functions are typically used to reduce artifacts in fast-fourier transforms of transient signals which result from imposing periodic

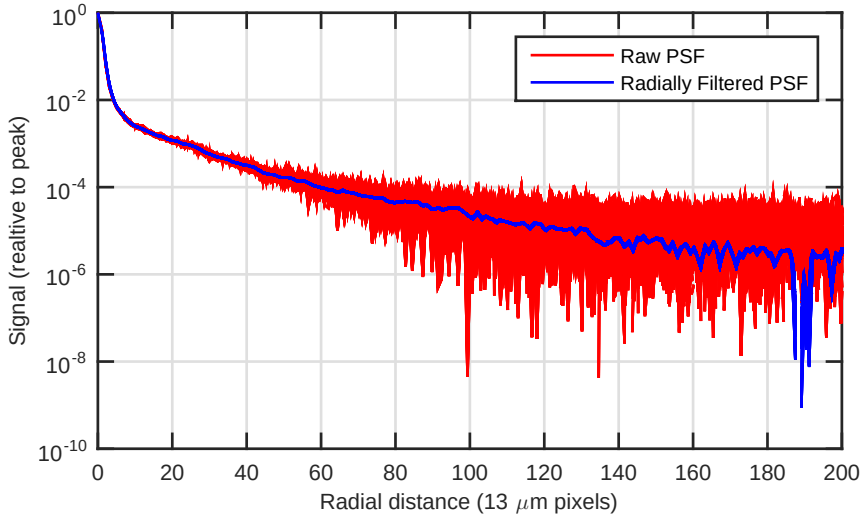

Figure 5.6 : Log plot of PSF amplitude versus radius shows far reaching extent of PSF. Rotationally filtering the signal greatly increase the SNR of the measured PSF.

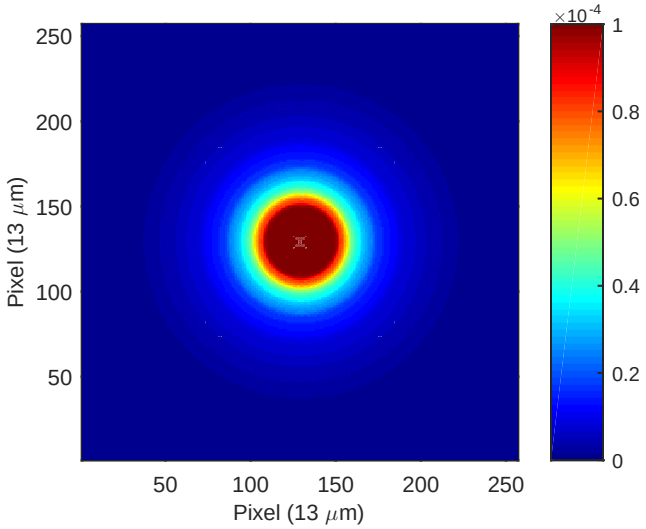

Figure 5.7 : PSF with compressed colormap highlights extent of PSF out to about $\pm$ 100 pixels

boundary conditions. Here it's just a convenient function by which we pixelwise multiple the measured signal. The results of the truncated and windowed PSF are shown

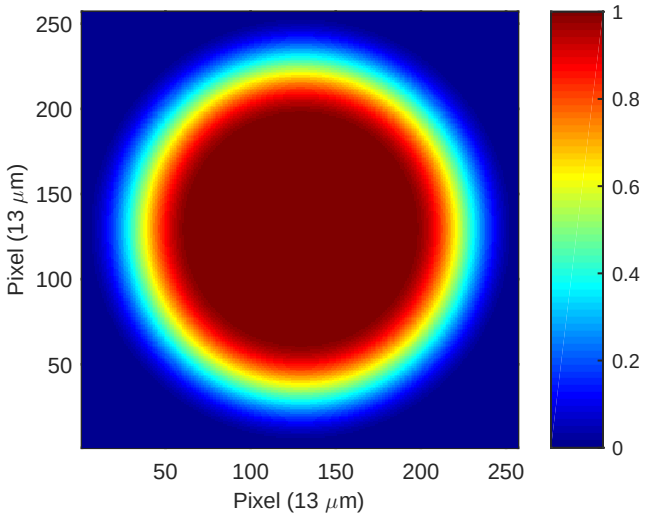

Figure 5.8 : Rotationally symmetric 2D Tunkey window used to truncate the measured PSF.

in Fig. 5.9. Notice how the central peak has not been effected however the edges of the signal now approach zero as expected.

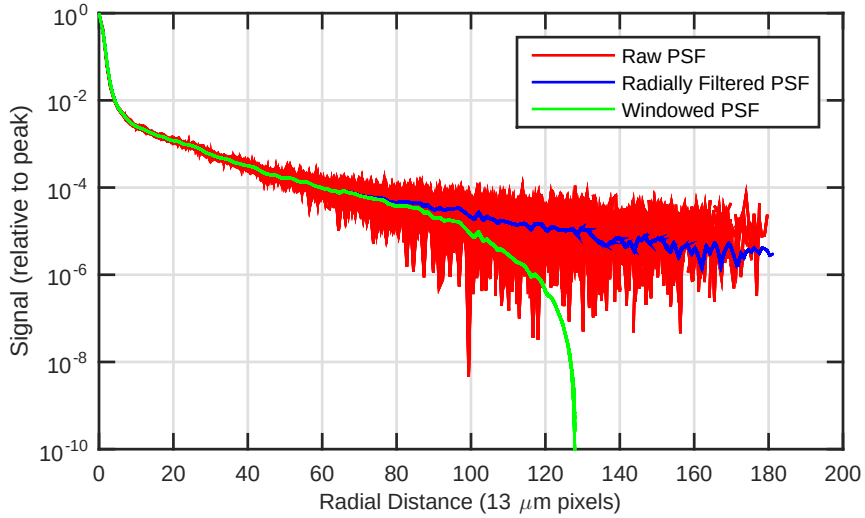

Figure 5.9 : Results of windowing the PSF, notice how the peak is uneffected while the edge of the signal tapers off towards zero.

This averaged PSF can be used to unblurr each image as soon as it is read in by our analysis program. To do this we use the Wiener filter algorithm built into MATLAB, i.e. the deconvwnr function. Set additive noise to zero for proper functioning.

The results on experimental temperatures are too drastic for data presented within this thesis and so they are presented without deconvolution. Temperatures were found to be reduced by the technique, but by up to 1 K leading to nonsensical results. This over-reduction in temperature hints at an over-reduction in blurring which could be explained if the wings of the spectra are lost within the noise generated by the deconvolution process. This could also be a result of nonlinearities in the blurring of the camera which make low level fluorescence blurring much lass significant than with high signal level PSF benchmarking. Since the blurring is primarily attributed to phosphor blooming this is a viable concern. Perhaps the discrepancy reflects the fact that the PSF was captured with 1x1 binning and 1x magnification while data was taken at 4x4 binning with 4x magnification. Although these aspects were considered (like in Sec. C.2) we found better results without using the deconvolution. We expect with further characterization this technique could prove useful. Particularly in pursuit of high resolution sculpted ultracold neutral plasmas where camera blurring could mask the onset of shocks or high-frequency ion plasma oscillations. [138].

5.3 Anomalous Ion Energy

Based on the previous estimations, with proper experimental control mixing of expansion energy into temperature measurements should be avoidable. Perhaps there is actually extra kinetic energy not considered in the presented model, there are many potential sources.

5.3.1 Density Perturbations

One of the most interesting prospects for studying ultracold neutral plasmas is reaching stronger coupling via lower temperatures. Therefore there has been continual concern regarding additional energy imparted to the plasma due to perturbations in the initial plasma density. These density modulations would induce ion motion adding to ion kinetic energy and heating the ions through Landau damping and/or collisions. [22] During ion hole and IAW experiments we see marked heating as the features propagate through regions [23, 24], thus supporting this concern. These unwanted density modulations could be inherited from any stage of the plasma creation process, i.e the patterns might originate from a non-Guassian MOT density distribution and/or non-uniform ionization.

MOT Atom Distribution

Recently there have been refinements to the apparatus resulting in higher MOT densities $n_{atom} \sim 10 \times 10^{16}\,\mathrm{m}^{-3}$. At these higher densities it is evident that the atomic density distribution has deviations from a 3D Gaussian on the order of 10 %, especially immediately after releasing the atoms. If these modulations are inherited by the plasma then this establishes ion acoustic waves (IAW) which will contribute to ion kinetic energy and ultimately ion temperature through damping and velocity changing collisions. It is well known that during the free expansion of an ultracold gas, density inhomogeneities are softened due to the ballistic nature of the expansion. Which begs the question, will longer MOT expansion times (t_{MOT}) lead to less anomalous heating?

In order to test this concern we measured ion temperature evolutions for a range of MOT expansion times 10 µs to 1000 µs, which inevitably varies the plasma size,

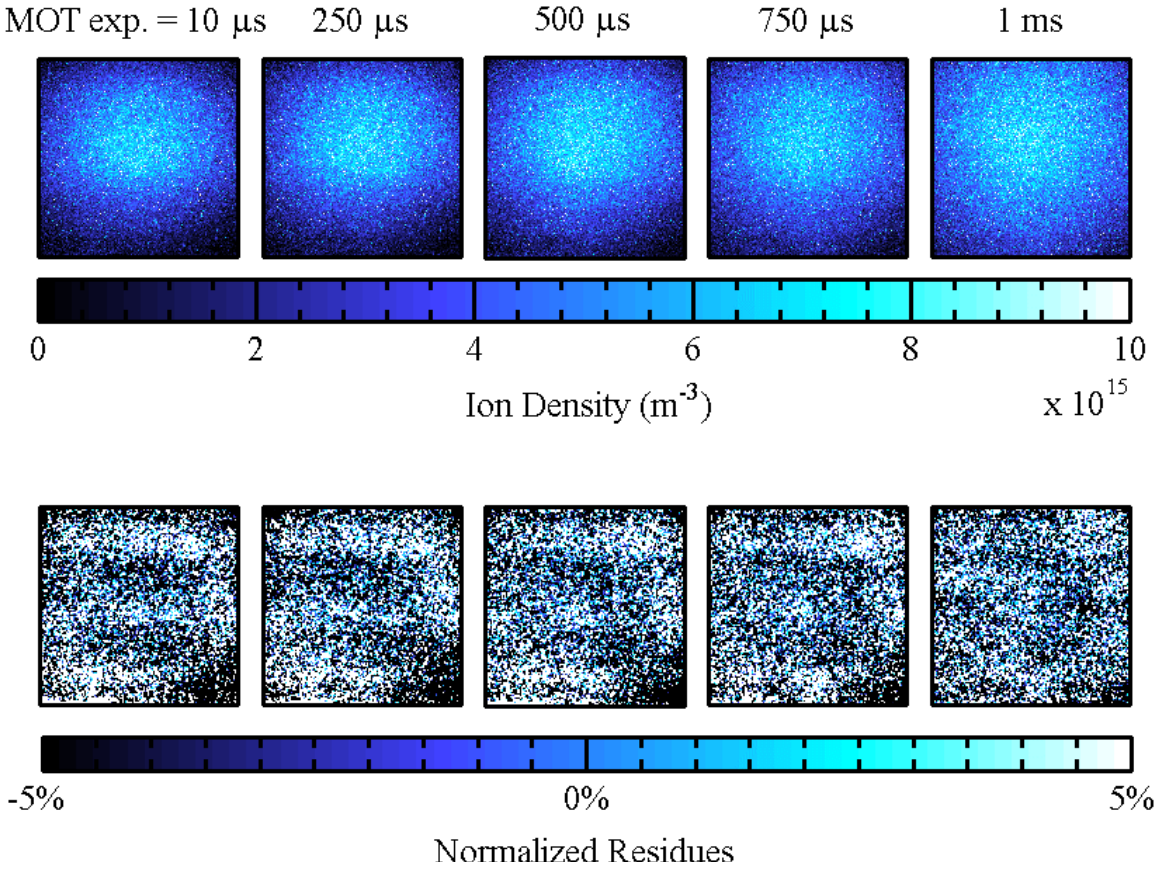

Figure 5.10 : 2D images of UNPs created with different MOT expansion times (top row). Note the decreasing structure within the normalized residues from a 2D Guassian fit as evolution time passes, particularly noticeable out to 500 µs. It is postulated this structure induces ion motion and contributes to ion heating.

ranging from 1 mm to 1.4 mm.. We used an electron temperature of ≈ 400 K. The density was kept constant by attenuating the ionizing beam to compensate for the changing density of the expanding MOT. This was accomplished by looking at ion resonance fluorescence for a small region of plasma and worked very well as seen in Fig. 5.11 (Top Right).

As seen in Figure 5.11 the results clearly show less extra energy as we allow the MOT to expand more before ionization. Particularly out to 500 µs, then it seems to

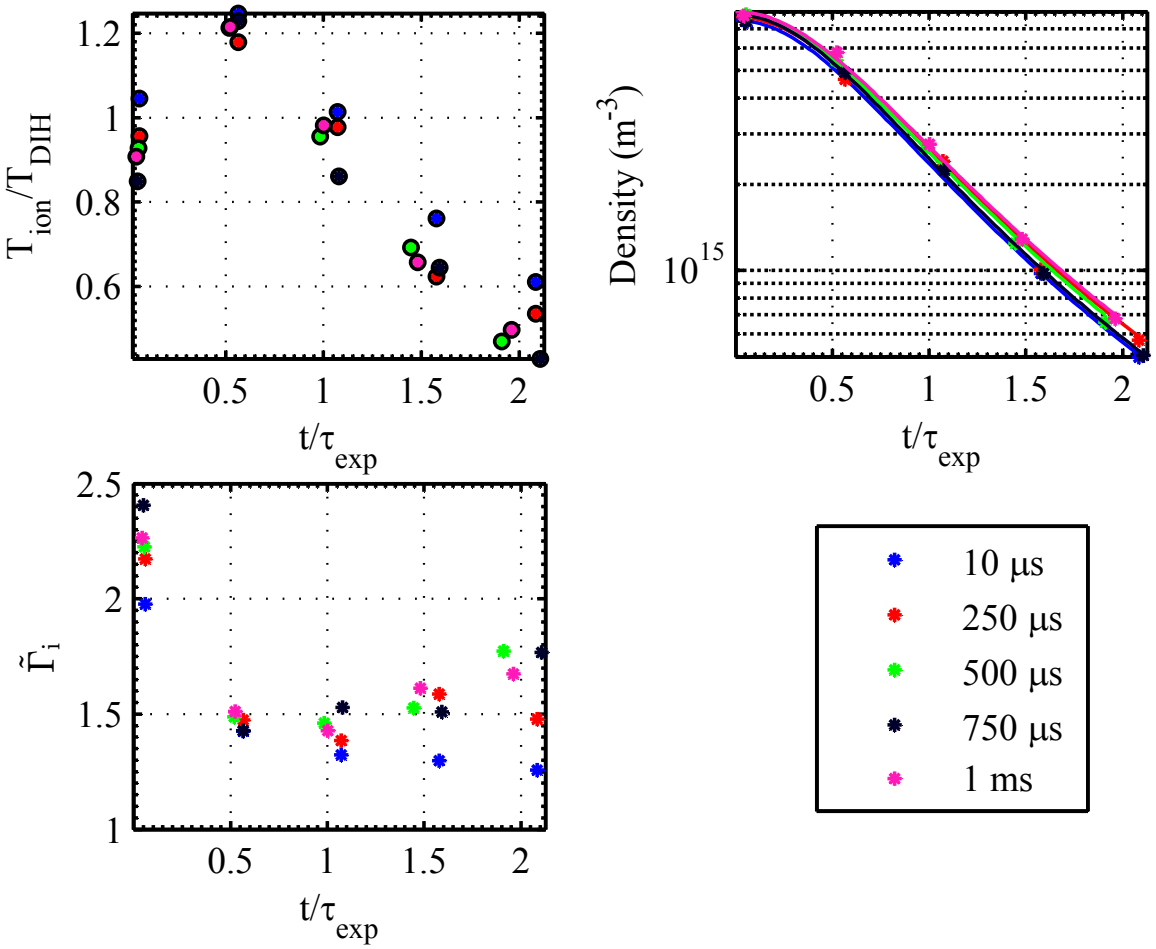

Figure 5.11 : (Top Left) Ion temperatures are higher for plasmas created from MOTs with less expansion time. (Top Right) Initial densities are similar and follow similar evolutions when scaled by τ_{exp}. (Bottom Left) The shielded coupling parameter reaches higher values for datasets with $t_{MOT} \geq$500 µs.

level out. Incidentally the longer expansion times lead to larger clouds and slower plasma expansion giving EIC heating more time. However calculations of expected evolutions show the difference to be insignificant for these conditions.

Ionization Modulation

Another source of density perturbations could be due to patterns on either of our ionizing beams that are then imprinted on the plasma. In the case of the push beam, i.e. the 461 nm beam, we are currently double pass amplifying the beam through a Bethune style dye cell achieving intensities upwards of hundreds of times I_{sat}. In this regime it is unlikely intensity patterns could be transferred to plasma. This is supported by the fact that retro-reflecting the push beam does not result in additional density. Furthermore the retro-reflection, when slightly offset would help to smooth out any lower intensity regions.

Patterns on the dye beam being imprinted onto the plasma is a very viable concern. We know we can intentionally perturb the plasma by modulating the intensity profile of the 412 nm beam. Furthermore dye lasers are known to exhibit poor beam quality. Visual inspection of our beam confirms that the quality is not great. There are patterns and stripes that change as the beam propagates indicating a large M^2 factor. There are clear diffraction effects visible from the transversely pump pre-amplifier stage which necessitates a trade off between gain and beam quality, even when leaning towards beam quality as far as possible, the beam still is not close to Gaussian.

Energy in an IAW

To estimate the feasibility of such concerns we look at the energy in an IAW. From Eqn. 30 in [23] we see that the energy imparted to the ions goes as

$$\Delta E_{ions} = \frac{1}{4} m_i (\frac{\omega}{k} A_0 e^{-\Gamma t})^2 sin^2(\omega t), \tag{5.5}$$

where m_i is the ion mass, ω is the IAW frequency, k is the IAW wavenumber, A_0 is the fractional density modulation, i.e. $\frac{\delta n}{n_0}$ and Γ is the decay rate of the wave.

If we assume that all the initial wave energy was converted to ion thermal energy we would obtain

$$E_{IAW} = \frac{1}{4} m_i (\frac{\omega}{k} A_0)^2 = \frac{3}{2} k_b \Delta T_{i,max}. \tag{5.6}$$

In the long wavelength limit $\frac{\omega}{k}$ can be replace with the sound speed $\sqrt{k_B T_e / m_i}$ we find that

$$\Delta T_{i,max} = \frac{1}{6} T_e[K] (A_0)^2. \tag{5.7}$$

In the short wavelength limit $\frac{\omega}{k}$ is replaced by $\frac{\omega_{pi}}{k}$ leading to

$$\Delta T_{i,max} = \frac{1}{6} \frac{ne^2}{\epsilon_0 k_B} \frac{A_0^2}{k^2} \tag{5.8}$$

We know from IAW and streaming plasma experiments we can clearly see the obvious modulations when they are on the order of 10% or even less. With a modest modulation depth of 5%, estimates yield a maximum heating on the order of $\sim 40\,\mathrm{mK}$ for 100 K electrons, and $\sim 160\,\mathrm{mK}$ for 400 K electrons. These estimates are on order of the measure discrepancies.

This concern is further supported by the time scale of the extra heat, with appears to manifest at or around $t = \tau_{exp}$. Incidentally this is the characteristic timescale for IAWs of wavelength equal to the characteristic cloud size, σ. Alternatively this would related to the arrival time of a wave packet one σ away.

High resolution regional analysis hints at structure within the density evolution that can appear to correlate with changes in temperature as well as shifts in center freq. Furthermore detailed review of regional center frequencies show deviations from expectations that seem to be correlated with the additional heating. Thus ion acoustic wave heating represents a feasible limitation for achieving stronger coupling given the current creation technique.

Transverse vs. Coaxial Excitation

Any ion motion induced by modulations of the ionizing process will be directed orthogonal to the beam and it's effect should be qualitatively different depending on the imaging beam geometry, since fluorescence is only sensitive to ion motion along its propagation axis. If the beams are transverse the motion should be immediately detectable, on the other hand, if the beams are coaxially oriented the ion motion will initially be imperceivable, until velocities are randomized and/or directed motion is damped. This is evident in temperature evolutions of similar plasmas imaged with the different geometries as shown in Fig. 5.12.

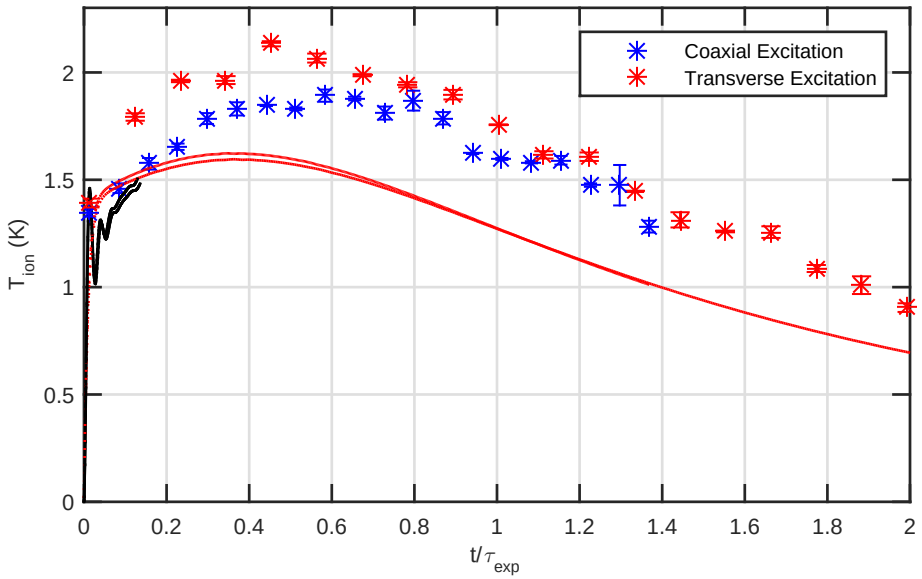

Figure 5.12 : Comparison of coaxial versus transverse ionization (relative to fluorescence beam) shows earlier and more significant extra heating for transverse ionization. This supports the idea that extra energy is the result of ionization modulation induced ion motion. For this study, $T_e = 50\,\mathrm{K}$ and $n = 4 \times 10^{15}\,\mathrm{m}^{-3}$

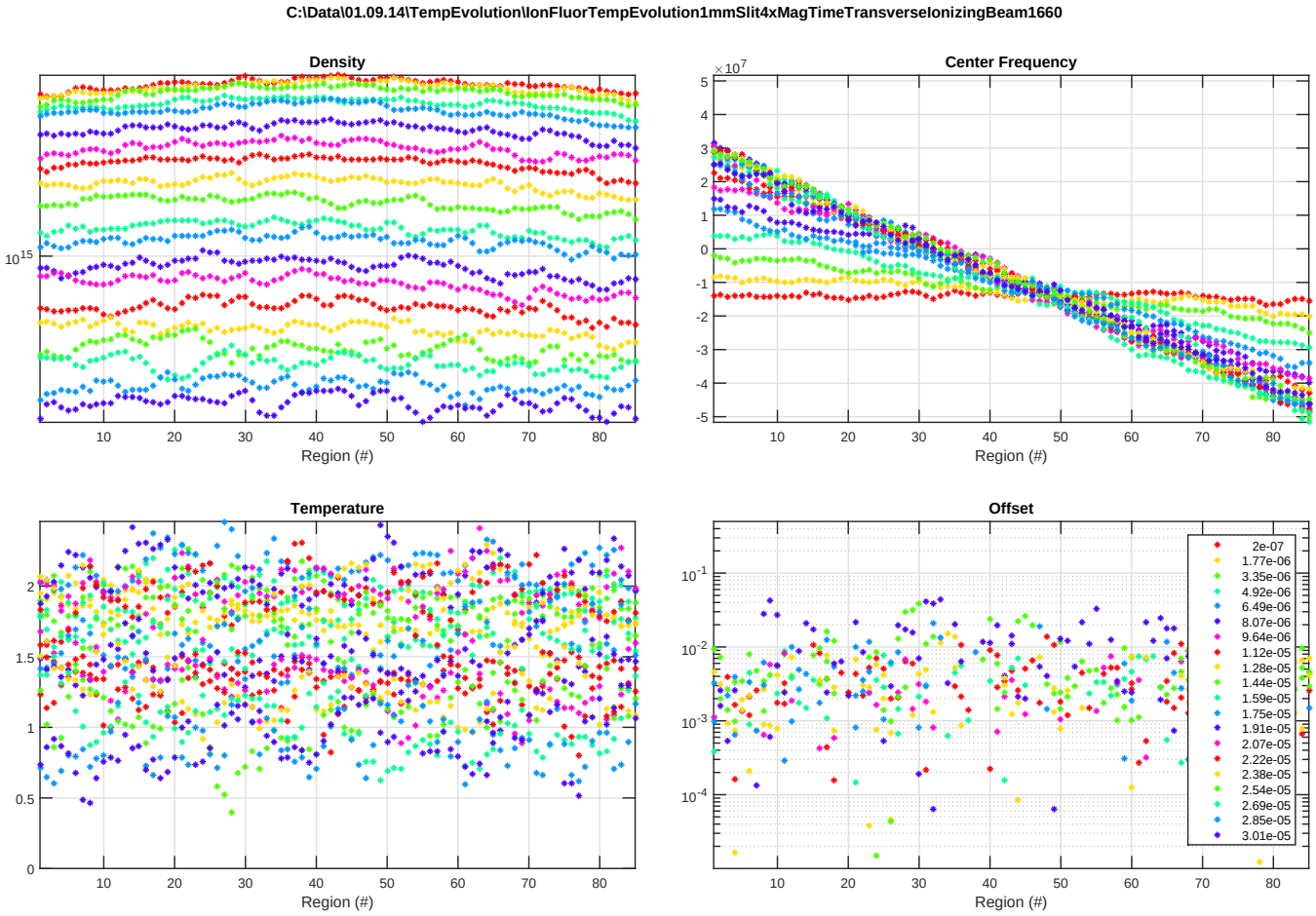

Figure 5.13 : Detailed regional analysis of transversely ionized UNP shows significant structure in both density and temperature profiles consistent with ionization induced ion motion.

5.3.2 Enhanced Electron Heating

The classical Spitzer treatment of electron-ion thermalization assumes a stationary plasma and uniform density. Perhaps density gradients or the expansion of the plasma effects collision rates. It is known that relative drift velocities enhance thermalization rates and during the earliest stage of the plasma expansion the electron component is experiencing a Coulomb explosion while the ions are at rest. [139]

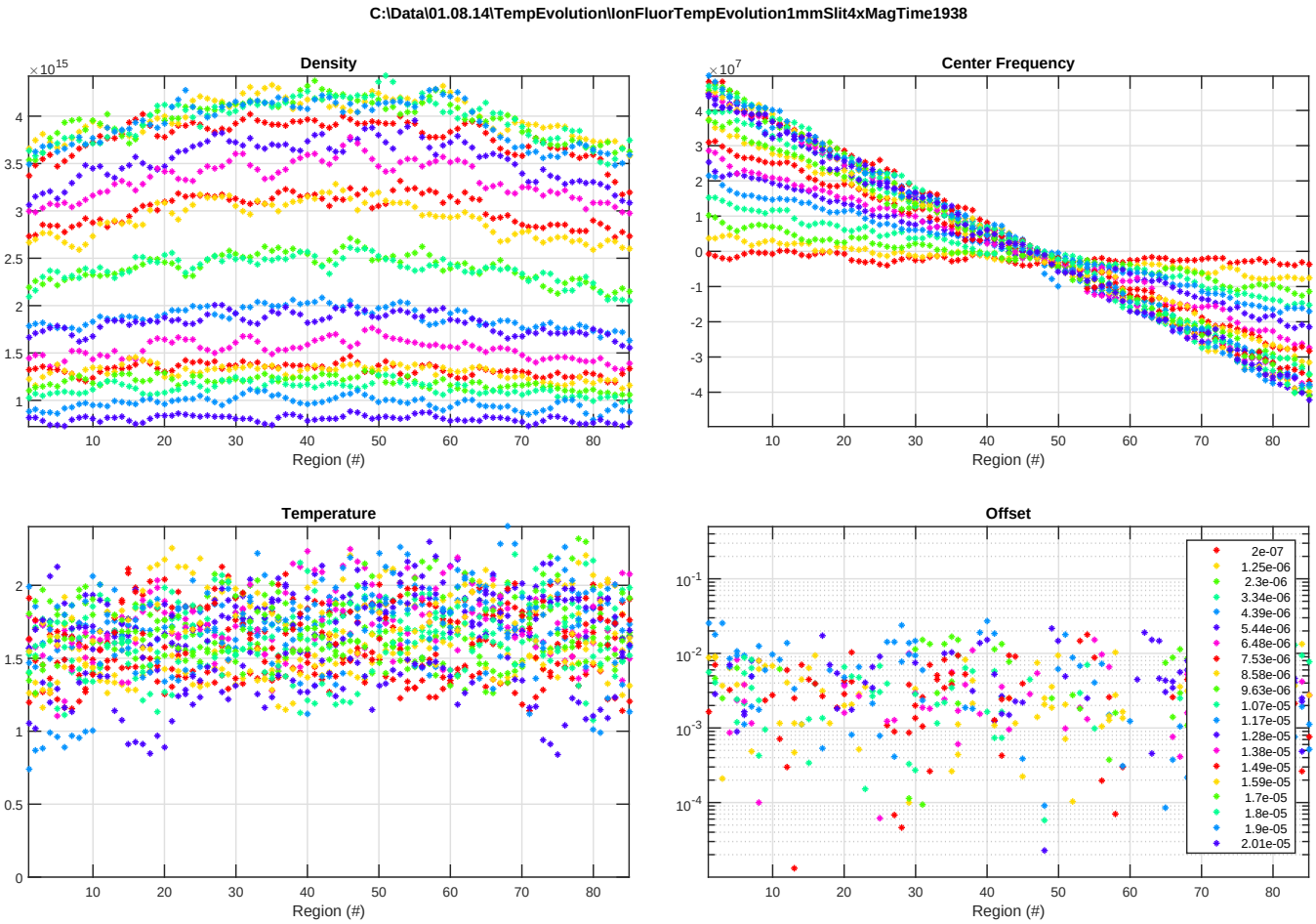

Figure 5.14 : Detailed regional analysis of coaxially ionized UNP shows less significant structure in temperature profiles.

5.3.3 Optical Pumping

The ion imaging transition, $^2S_{1/2} - {}^2P_{1/2}$ is not closed. Excited ions can decay into the $^2D_{3/2}$ with a branching ratio of 1 : 13 and a lifetime of ∼400 ms, see Fig. 2.3 for the ion's energy level diagram. The plasma only exists for ∼100 µs thus any ion falling in the $^2D_{3/2}$ will be lost into this "dark state."

Consider the process of collecting a full fluorescence spectra, on resonant ions will scatter more photons then those within the wings of the spectra and will preferentially

pumped into the dark state. This will soften the peak of the spectra resulting in an artificial broadening and the extraction of ion temperatures that are higher than actual. To avoid this effect one could image with short enough pulses that each ion only scatters one photon however this limits the amount of available signal and is not ideal. Instead we will attempt to find a maximum threshold for which the artificial broadening can be neglected.

To this effort a simulation of the imaging process was developed using rate equations for the three levels and the pertinent experimental parameters to calculate the expected fluorescence signal as a function of detuning, i.e. a spectrum. This can then be fit to our model Voigt profile to calculate the expected discrepancy. The results are summarized in Figure 5.15.

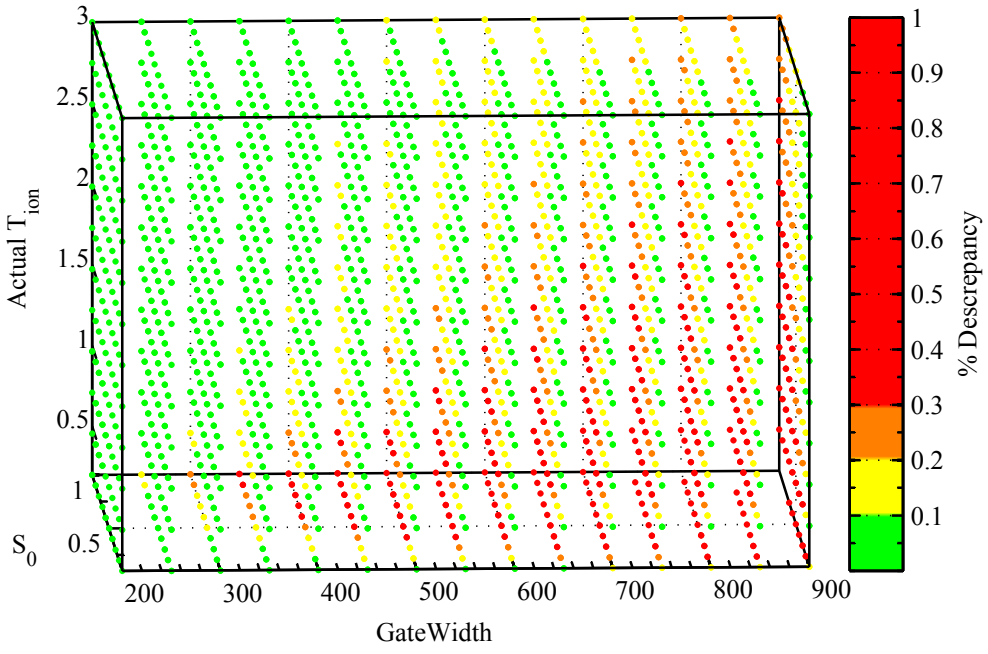

Figure 5.15 : Artificial broadening of ion florescence spectra due to optical pumping to the dark state. Notice how imaging times of even 200 ns can begin to cause 10% deviations in measured ion temperature.

5.4 Conclusions

The many estimates and considerations of this chapter show how easily ion temperatures can be skewed, thus great care must be take to maintain the integrity of the measurement. Particularly at higher electron temperatures, gatewidths must be kept small and regions narrow to avoid misinterpreting bulk flows as thermal energy. In many case gatewidths used within are on the boundary of causing siginificant effects and could contribute to some of the extra measured energy. Sheet fluorescence and magnified imaging both appear necessary for accurate temperature measurements, perhaps the typical 1 mm sheet width is still too large. Although it's time to pass on the proverbial torch, pursuit of stronger coupled ultracold neutral plasmas is gaining momentum and should bring many interesting surprises.

Appendix A

Calculations

A.1 Derivation of TBR Electron Cooling Shut off

As an approximation for the effects of TBR a simple approach is to simply "turn off" electron adiabatic cooling when TBR becomes significant. Since this happens at about $\Gamma_e \sim 0.2$ if suffices to set $\dot{\Gamma}_e = 0$ when $\Gamma_e > 0.2$. We will make use the following relations,

$$\Gamma_e = \frac{e^2}{4\pi\epsilon_0 a_{ws} k_B T_e} \implies \dot{\Gamma}_e = \frac{e^2}{4\pi\epsilon_0 k_B}\left[\frac{-\dot{a}_{ws}}{a_{ws}^2 T_e} - \frac{\dot{T}_e}{a_{ws} T_e^2}\right] \tag{A.1}$$

$$a_{ws} = \left[\frac{3}{4\pi n}\right]^{1/3} \implies \dot{a}_{ws} = -\frac{1}{3}\left[\frac{3}{4\pi}\right]^{1/3} n^{-4/3}\dot{n} \tag{A.2}$$

$$n = \frac{N}{\left(\sqrt{2\pi}\sigma\right)^3} \implies \dot{n} = \frac{-3N\dot{\sigma}}{(2\pi)^{3/2}\,\sigma^4} \tag{A.3}$$

$$\dot{\sigma^2} = 2\gamma\sigma^2 \implies \dot{\sigma} = \gamma\sigma. \tag{A.4}$$

Proceed to solve $\dot{\Gamma}_e = 0$ for $\dot{T}_e$.

$$\dot{T}_e = \frac{-T_e \dot{a}_{ws}}{a_{ws}} \tag{A.5}$$

$$= -\gamma T_e. \tag{A.6}$$

The result is very similar in form to the adiabatic result, i.e. $\dot{T}_e = -2\gamma T_e$ and is thus easy to implement as,

$$\frac{\partial T_e(t)}{\partial t} = -\left(2 - \mathcal{F}(\Gamma_e)\right)\gamma(t) T_e(t), \tag{A.7}$$

where

$$\mathcal{F}(\Gamma_e) = \begin{cases} 1, & \text{if } \Gamma_e > 0.2, \\ 0, & \text{otherwise.} \end{cases} \tag{A.8}$$

Note this derivation also shows that $\gamma = \frac{\dot{a}}{a} = \frac{\dot{\sigma}}{\sigma}$ which offers an intuitive interpretation of the expansion parameter, γ, the relative rate of change of length scale in the plasma.

A.2 Spectral Guessing Algorithms

Adaptive spectral guessing algorithms were developed to aide in fitting spectra for a wide array of plasma parameters. Data is treated differently the first time it is analyzed versus sub-sequent re-analysis. For the first analysis run only, density is estimated by a numerical integration of the spectra which can be related to the density within the region. First-run ion temperatures are estimated by modeling DIH and adiabatic expansion only, i.e. Eqn. 3.11, $\frac{\partial T_i(t)}{\partial t} = -2\gamma(t)T_i(t)$ with $T_i(0) = T_{DIH}$. On subsequent data runs, both density and temperature guesses are read from .mat files that store the previous robustly averaged regional temperature. On all data runs, the guesses for center frequency and offset are made on-the-fly. Center frequency estimates are simply the frequency with the maximal signal. Offsets are estimated by the mean of the lowest 10-percentile of spectra values. Unless, the spectral width is estimated to be larger then the scan range, then the offset is guessed to be 0. The results are consistent performance of spectral fits over a wide range of plasma parameters and this technique helps assist speedy convergence of nonlinear fitting routines. This was a key step in making full 2D analysis feasible.

A.3 Error Propagation

In order to properly propagate errors function definitions have been written in the following format with the inclusion of the MATLAB function "error_propagation" which accurately propagates errors numerically using randomly generated values within the provided standard deviations. By using the "nargin" conditional the base function will work with or without providing standard deviations of the parameters.

```
function [ReturnVal,ReturnSD] = FunctionName(Param1,Param2,Param1SD,Param2SD)


%% define the base function
Fn = @(Param1,Param2) Param1+Param2;


%% calculate return value and set ReturnSD=0 incase ParamSDs are not provided
ReturnVal=Fn(Param1,Param2);
ReturnSD=0.*Param1;


%% if ParamSDs are provided propagate errors
if nargin==4
    for i=1:size(Param1,1)
        [~,ReturnSD(i)]=error_propagation(Fn,Param1(i),Param2(i),Param1SD(i),...
        Param2SD(i));
    end
end


end
```

A.4 Numerically Simplified Formulas

In order to expedite code execution times, many plasma parameter formulas where recast into forms where all possible numerical simplification has been pre-calculated. Assuming densities in units of m^{-3} and temperatures in K,

$$\omega_{pi}[2\pi\mathrm{Hz}] = 0.1409\, n^{1/2} \tag{A.9}$$

$$\omega_{pe}[2\pi\mathrm{Hz}] = 56.40\, n^{1/2} \tag{A.10}$$

$$a_{ws}[\mathrm{m}] = 0.6204\, n^{-1/3} \tag{A.11}$$

$$\lambda_D[\mathrm{m}] = 69.02\, T_e^{1/2} n^{-1/2} \tag{A.12}$$

$$\lambda_l[\mathrm{m}] = 1.6706 \times 10^{-5}\, T_e^{-1} \tag{A.13}$$

$$\kappa_e = 8.988 \times 10^{3}\, n^{1/6} T_e^{-1/2} \tag{A.14}$$

$$\Gamma_{e,i} = 2.693 \times 10^{-5}\, n^{1/3} T_{e,i}^{-1}. \tag{A.15}$$

Appendix B

Useful Plots

B.1 Size Corrections

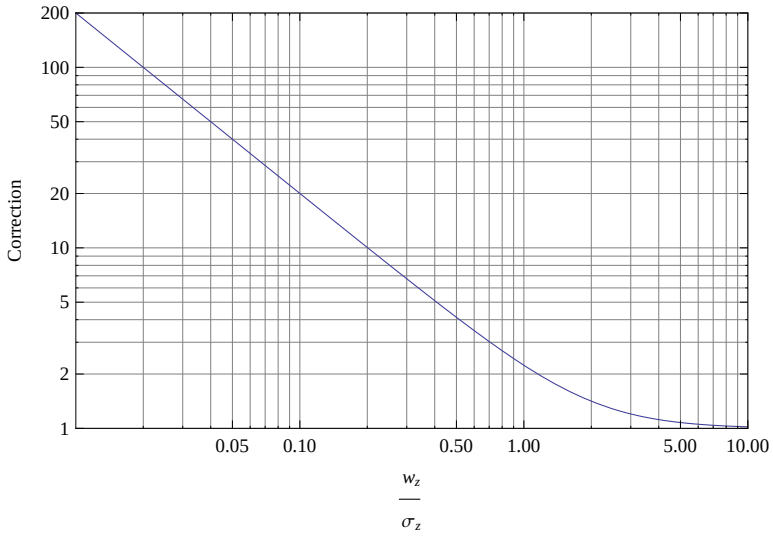

Figure B.1 : Size correction,Z_{corr}, plotted versus beam:cloud radius ratio

B.1.1 Correction at later times

We have seen how the plasma size, imaging beam size and slit height all effect the calibration of the density. At later times (e.g. $t \geq 10 * \tau_{exp}$) it's prudent to be concerned about the size and shape of the plasma as compared to the ideal self-similar model. With this in mind we explore the size corrections at late times, i.e.

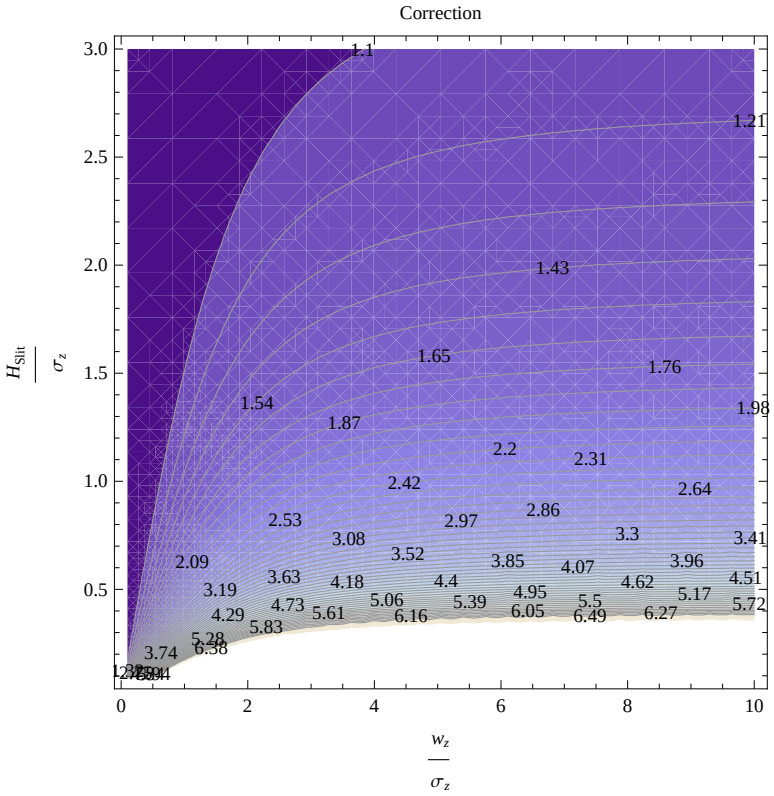

Figure B.2 : Slit correction, $Slit_{corr}$, plotted as a function of slit:cloud and beam:cloud size ratios

when $\sigma_z >> \omega_v$. The beam size correction along the imaging $\hat{z}$ direction is

$$\sqrt{\frac{\omega_z^2 + 4\sigma_z^2}{\omega_z^2}}, \tag{B.1}$$

which asymptotes to

$$2\sigma_z. \tag{B.2}$$

The correction due to slit size is

$$\frac{1}{erf\frac{H_{slit}\sqrt{4\sigma_z^2+\omega_z^2}}{2^{3/2}\omega_z * \sigma_z}} \tag{B.3}$$

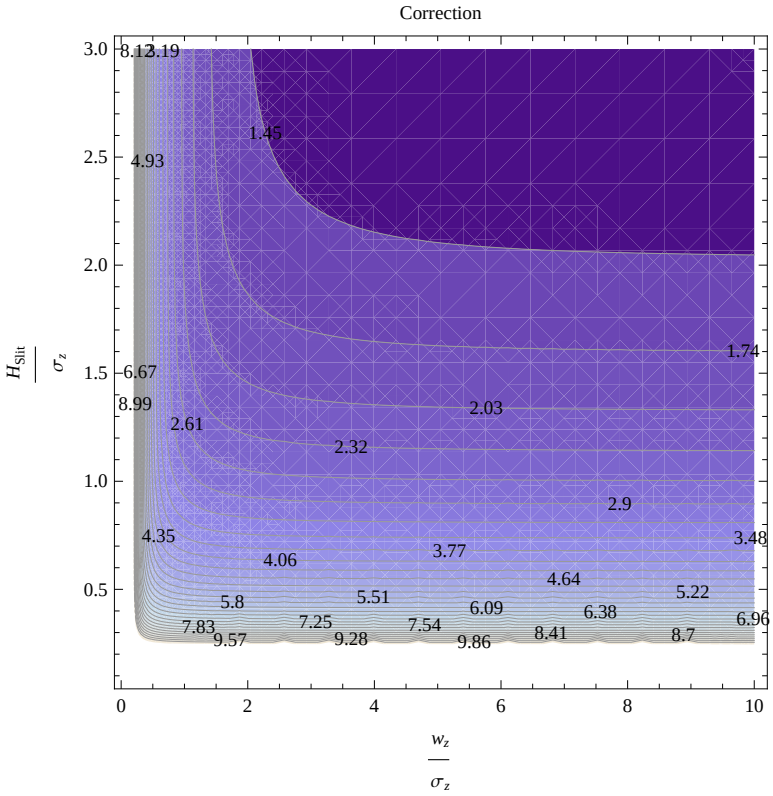

Figure B.3 : Total correction, $Slit_{corr} * Z_{corr}$, plotted as a function of slit:cloud and beam:cloud size ratios

which asymptotes towards

$$\frac{1}{erf\frac{2H_{slit}}{\omega_z}} \tag{B.4}$$

When combined, along with the conversion of areal density to volume density, (i.e. $(\sqrt{2\pi}\sigma_z)$) the overall correction is

$$\frac{\sqrt{2}}{\sqrt{\pi}erf\frac{2H_{slit}}{\omega_z}}, \tag{B.5}$$

which clearly does not depend on the size or shape of the plasma, nor time. This implies confidence in density measurements taking at late times and makes sense physically. Once the variations in density are large compared to the illuminated

region that region will contain a uniform density and the conversion factor should become a constant as seen.

B.2 Typical Value Plots

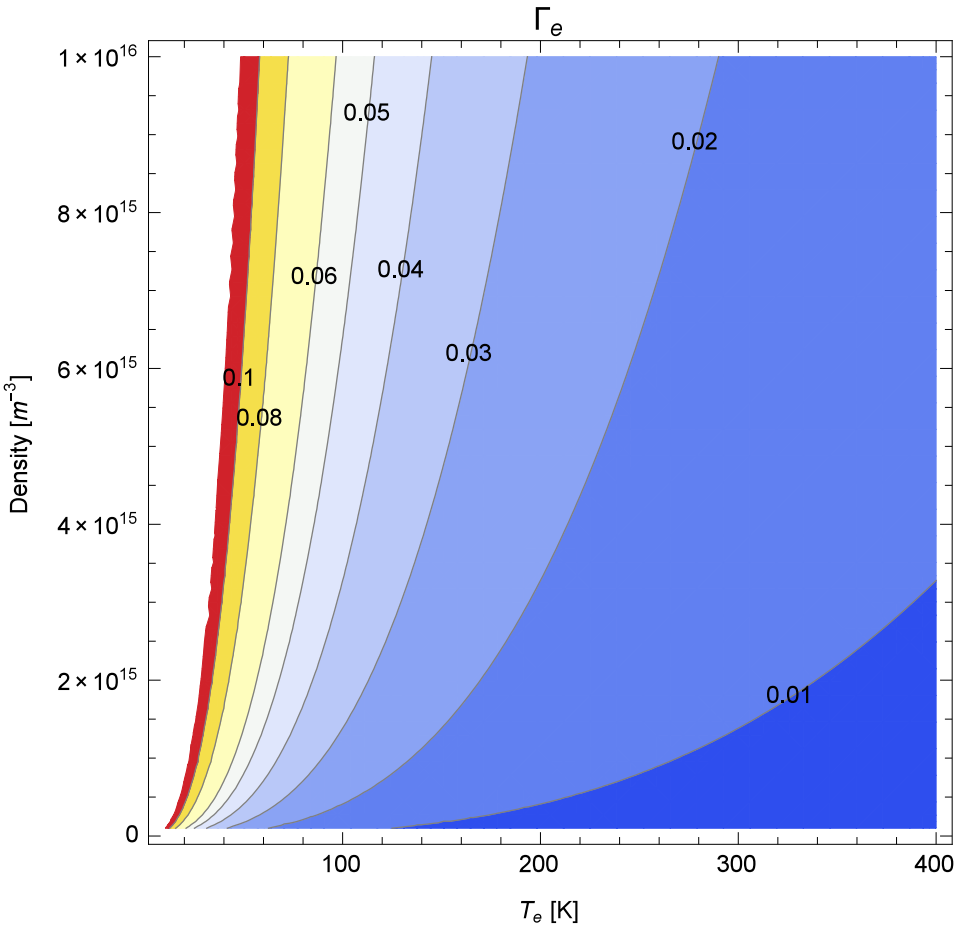

Figure B.4 : Typical values for the electron Coulomb coupling parameter, Γ_e plotted versus T_e and n.

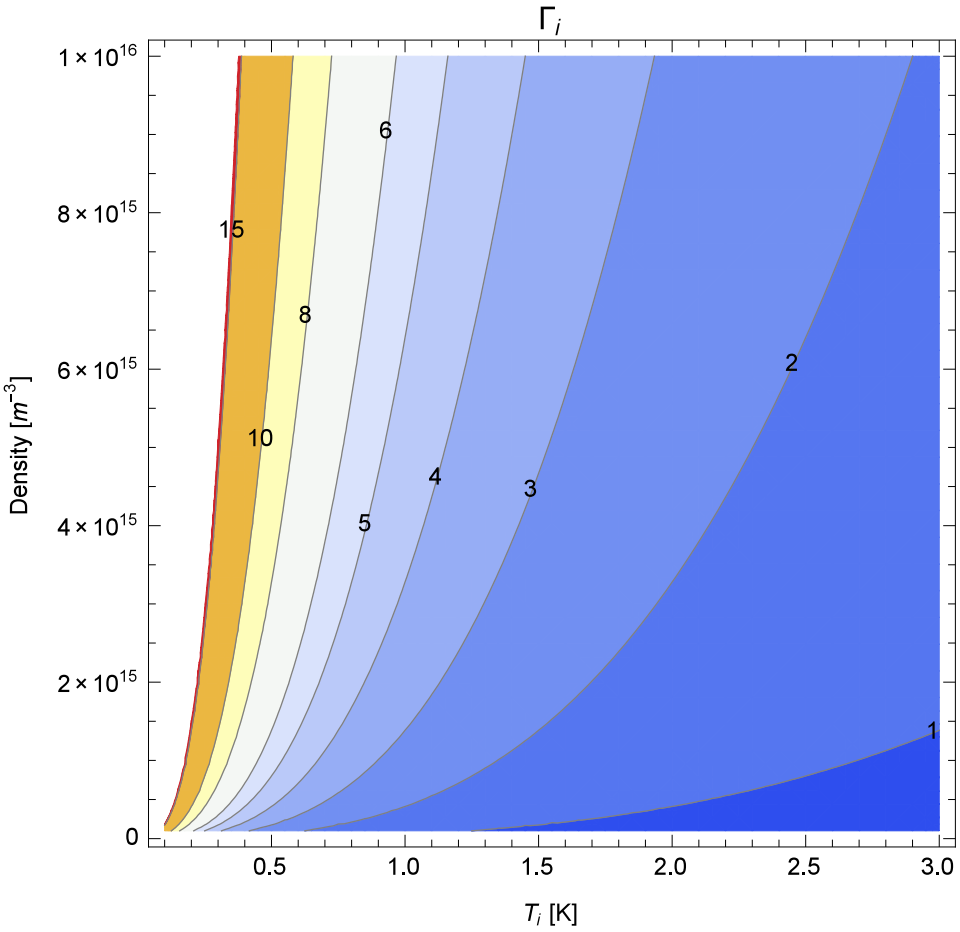

Figure B.5 : Typical values for the ion Coulomb coupling parameter, Γ_i plotted versus T_i and n.

B.3 2D Density Image Fits

2D density images are fit to a 2D Gaussian distribution and the results are plotted as shown in Fig. B.6. Notice how at later times the $\hat{x}$-dimension of the cloud is cut off as ion's are Doppler shifted out of resonance due to high bulk velocities. This could be avoided by scanning the imaging laser further, however it was not otherwise necessary for that dataset.

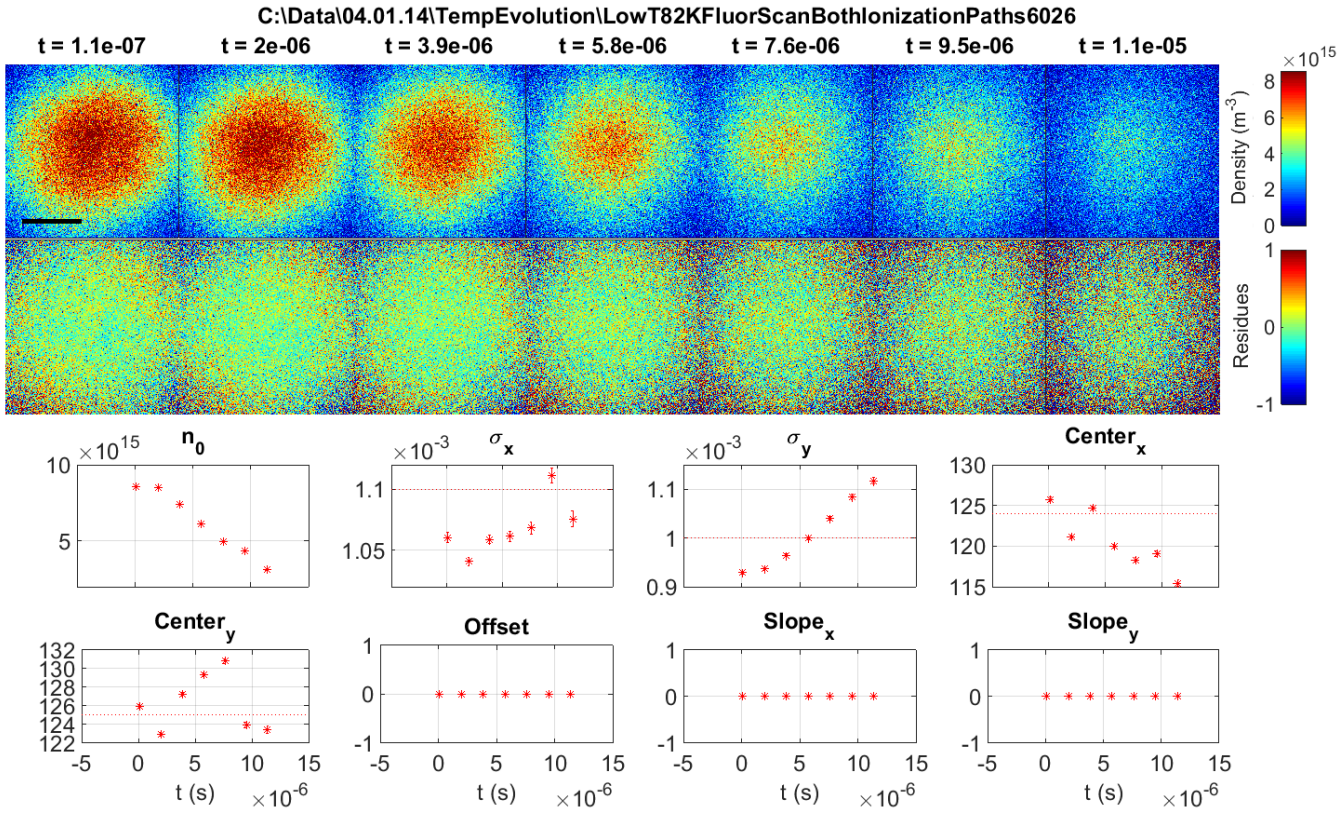

Figure B.6 : Evolution of 2D density images constructed from calibrated fluorescence spectroscopy signal.

B.4 Plasma Parameter Summary

At the end of each datasets post-processing, density and temperature evolutions are used to calculate a full slew of useful plasma parameters. The typical results are shown in Fig. B.7.

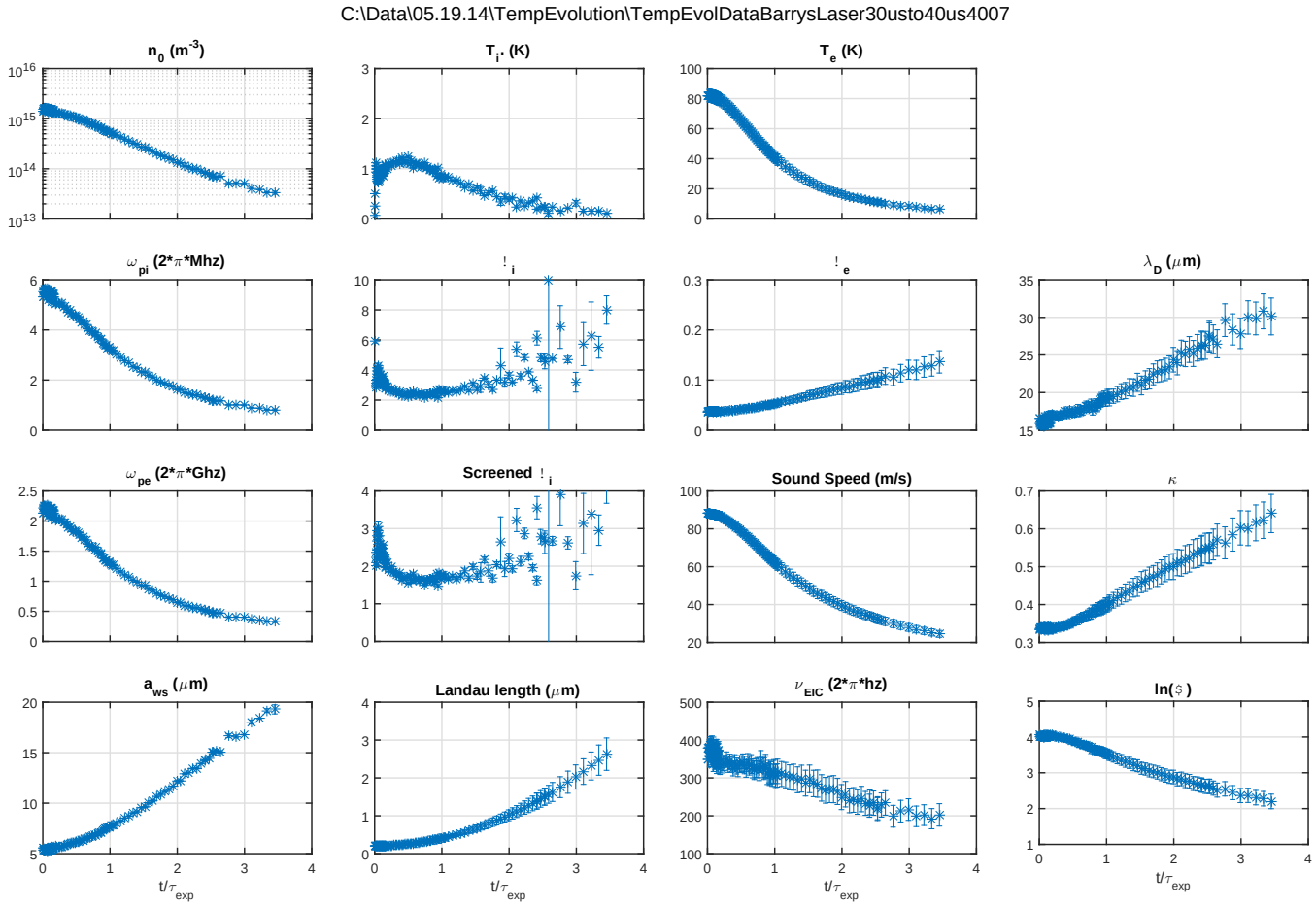

Figure B.7 : Summary plasma parameter plot offers a convenient summary of useful plasma parameters for quick reference and review.

Appendix C

Image Analysis

Salt and Pepper Removal

Looking at any raw data from a CCD one can typically find pixels with extreme values, those much higher or lower than expected are call 'hot' or 'cold' pixels respectively. Our experimental data is no exception. Often it is obvious to a human observer a pixel is bad, but how can a computer decide such and how can it distinguish false values from noisy data? This is a common problem in image processing that has been addressed by with an array of techniques. [140]

To this end I have developed a MATLAB function from removing pixels which are grossly statistically inconsistent with their neighbors. The function begins by creating a copy of the image to be processed and performs a 2D median filter on in. This filter creates an image in which each pixel is the median of it's neighborhood, eliminating outliers while preserving edges. [141] This median image will serve as replacement pixels for those that are found to be bad. To isolate the bad pixels a 2D standard deviation filter is applied to the original image, this creates another image in which each pixel represents the standard deviation of it's neighborhood. Pixels in the original image are deemed bad if they fall too many local standard deviations away from the local median. This confidence interval sets the sensitivity of the rejection criteria and should be is at least $\pm 4\sigma_{sd}$.

This process can be ran at various stages of analysis. Results of processing every

I_{img} and I_{bkd} for fluorescence imaging are shown in Fig. C.1. The results are aesthetically very pleasing, major holes and hot pixels are eliminated as shown Image dynamic range has been reduced so contrast is enhanced. Overall the quality of spectral data seems improved as well, smoother evolutions of density and temperature as well as fewer bad spectra fits. Even further improvement can be seen be running the process again on each image after background subtraction, (i.e. $I_{img} - I_{bkd}$). The code is relatively simple and is included in Sec. C.1. This process is also useful for simply plotting the data without noise, if done only to plotted data, one can enjoy the cosmetic benefits without any worry of effecting data or statistics.

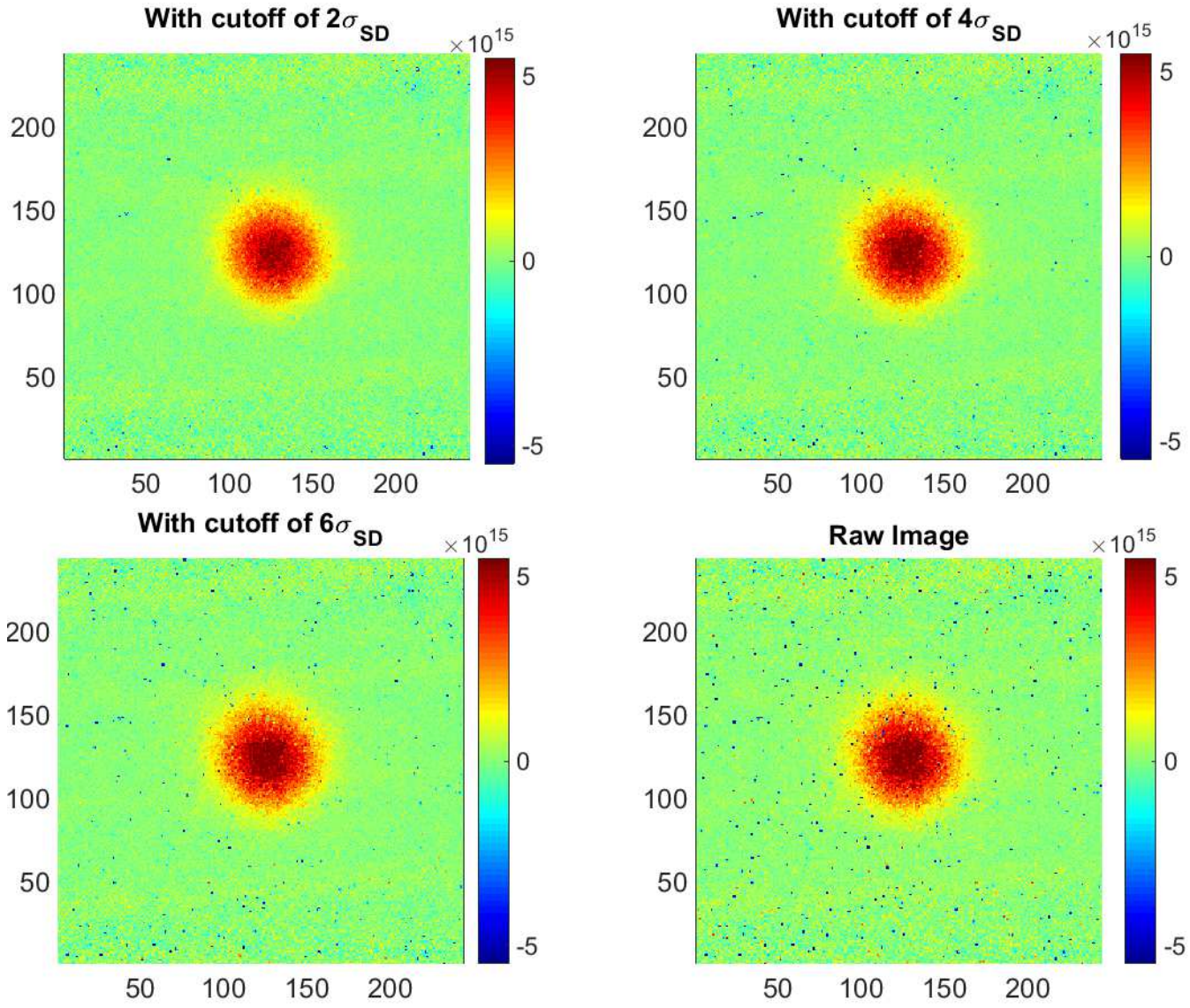

Figure C.1 : Results of salt and pepper removal on each image and each background. The automated elimination of extreme outliers results in better overall data quality and enhanced image contrast. Results are for various cutoff criteria of 2,4, or 6 times the local standard deviation. The process is ran on each detuning's image and background seperately, however, results are shown for the calibrated density representing an integration over detunings. Notice how a cutoff of $2\,\sigma_{SD}$ results in a slight alteration of measured peak density and is thus considered too stringent. Cutoff values of $4\,\sigma_{SD}$ and higher do not affect spectra fits results, other than sometimes improving error bars.

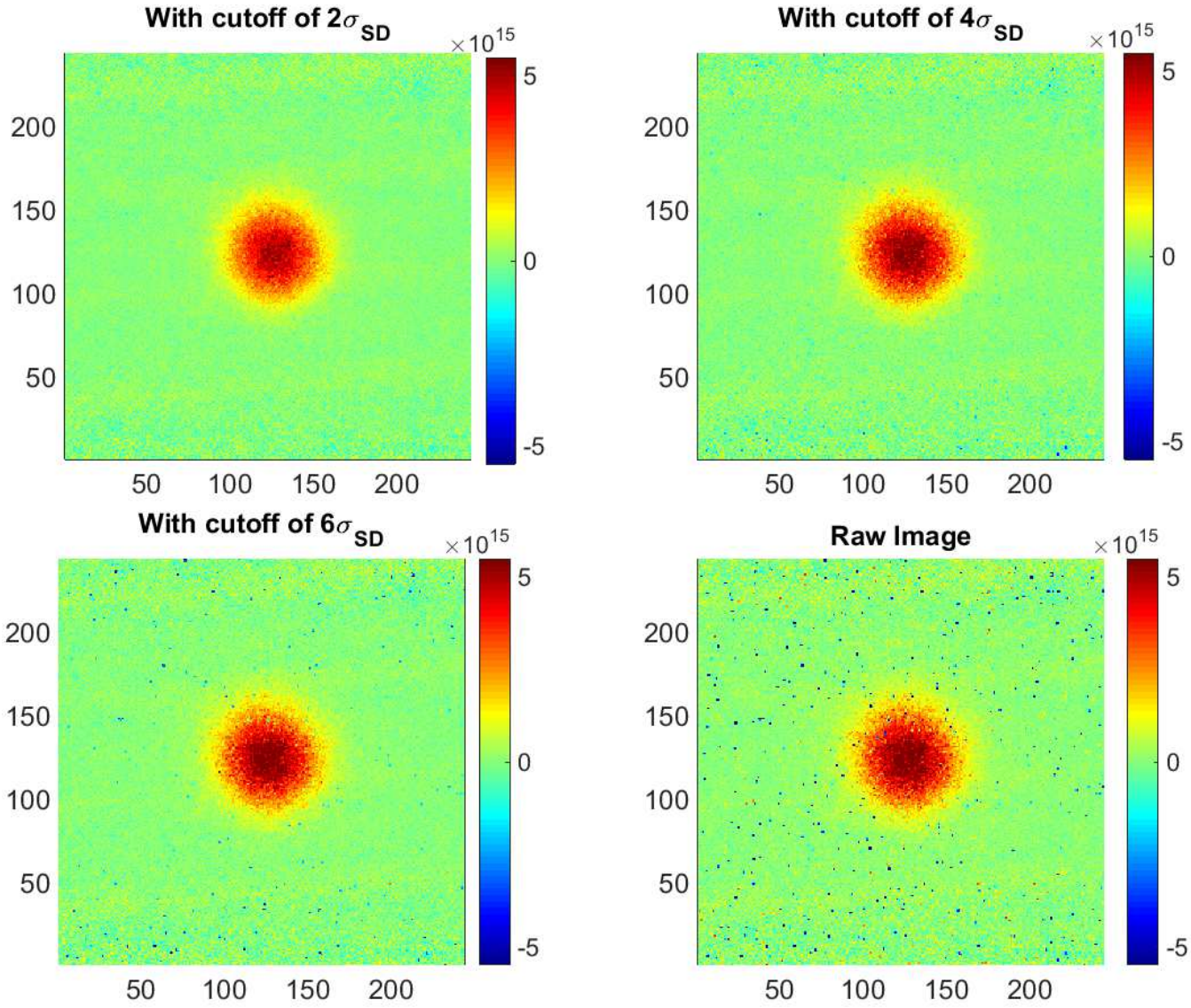

Figure C.2 : Running the process on each image, each background and then the image after background subtraction (i.e. $I_{img} - I_{bkd}$) yields even better results, as compared to Fig. C.1.

C.1 Salt and Pepper Code

```
function [ReturnImage]=RemoveSaltPepper(Image)


%%initialize vars
```

```
ReturnImage=Image;

%%Image used for replacing bad pixel values, keep size small to maintain
%%spatial resolution of replaced pixels (~3)
ReplaceHoodSize=3;
ReplaceImage=medfilt2(Image, [ReplaceHoodSize ReplaceHoodSize]);

%%Meant to represent ideal image, without outliers, keep size smaller
%%than plasma features (~7)
MedHoodSize=7;
MedianImage=medfilt2(Image, [MedHoodSize MedHoodSize]);

%%Local standard deviation, size should be large to avoid significant
%%influence from outliers (~17)
SDHoodSize=17;
SDImage=stdfilt(Image,ones(SDHoodSize));
SDImage=imfilter(SDImage,fspecial('gaussian',SDHoodSize,SDHoodSize/3));

%%How many SDs before rejected
SigmaLevel=4;

%%Calculate thresholds
UpperThreshold=MedianImage+SigmaLevel*SDImage;
LowerThreshold=MedianImage-SigmaLevel*SDImage;
```

```
%%Find outliers
[BadPixRow,BadPixCol]=find(Image<LowerThreshold||Image>UpperThreshold);

%%Replace outliers
for i=1:size(BadPixRow,1)
ReturnImage(BadPixRow(i),BadPixCol(i))=ReplaceImage(BadPixRow(i),BadPixCol(i));
end
```

C.2 Binning the Point Spread Function

Although the PSF was captured at 1x1 binning techniques to convert this measurement to binned versions were developed. Even though PSF deconvolution efforts were ultimately not applicable to 4x magnification results presented herein, this artificial binning technique is presented here since it is not necessarily suspected of causing the discrepancy.

We attribute the entirety of the blurring to the intensifier and so the PSF we use to post process data is calculated based on camera ccd binning only, regardless of any magnification that happens before the camera. To determine the PSF for binned images the full resolution PSF is binned artificially.

For example, to determine the PSF with 2x2 binning the image is spatially filtered with the following kernel,

$$\begin{bmatrix} 0.25 & 0.25 \\ 0.25 & 0.25 \end{bmatrix} \tag{C.1}$$

and every 2nd pixel (referenced from the peak) is extracted. However, the binning filter must be offset one half pixel up-down as well as left-right in order to preserve

centration of the peak so we actually filter with this kernel,

$$\begin{bmatrix} 0.0625 & 0.125 & 0.0625 \\ 0.125 & .25 & 0.125 \\ 0.0625 & 0.125 & 0.0625 \end{bmatrix}. \tag{C.2}$$

The extension to larger binnings is trivial and the results of the most common binnings are shown in Fig. C.3.

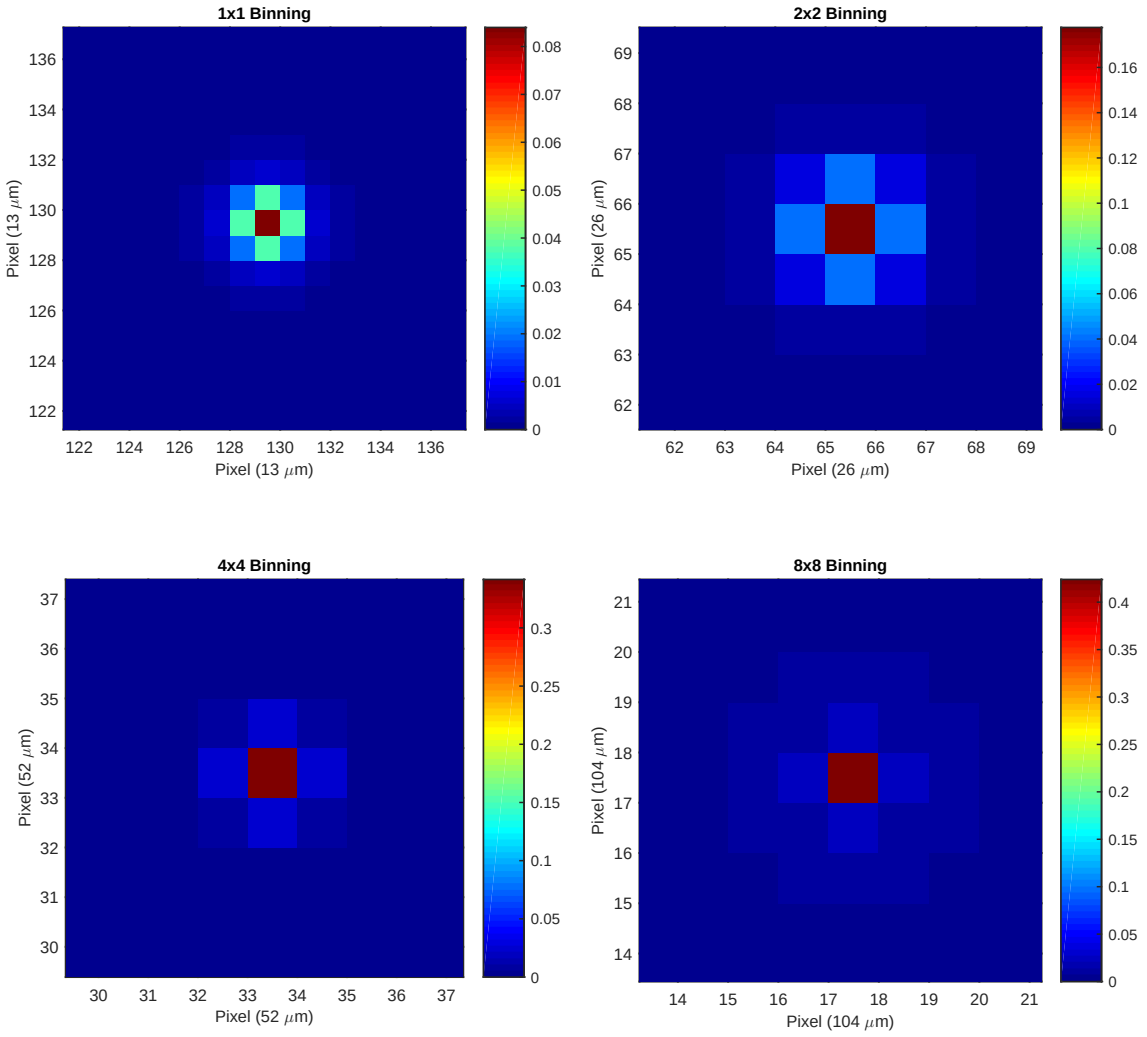

Figure C.3 : PSFs with various binning. Color indicates percentage of total signal within that pixel.

Appendix D

Bonus Material

Of all the things that must happen for science to be successful, many of them are not found in any textbook, but instead rely on the researcher's keen attention to detail as well as a constant mindfulness towards quality. This chapter aims to be a collection of pitfalls, tactics, and improvements that have proven to be valuable over the years.

D.1 Improving Stability

Stability of the experiment is paramount for the consistent collection of reliable data. However, being comprised of numerous innately sensitive pieces of equipment it is inevitably a delicate apparatus. Thus it's prudent to make sure the mechanical assembly is robust and does not enhance the sensitivity of the experiment. In fact, it is often not the $250,000 laser developed by a team of engineers that causes issues but the $5 cable that has been stepped on too many times. With this mindset and well maintained lasers the experiment can benefit from decreases downtime and greater productivity.

The most common failure mode of any electronic assembly is a simple open circuit and being that the experiment is a conglomerate of numerous sub-assemblies the possibilities for such are nearly countless. Anywhere physical connections are made, represents a potential failure of the experiment and we experience the consequences regularly. The most common parts to fail are this with mechanical structures meant

to make and break contact, such as toggle switches and BNCs. Both of these parts are rated for a finite number of cycles and as the lab approaches the middle of it's second decade, many of these are reaching the end of their life. Be on the lookout for spurious signals when cables or switches are manipulated. When designing experimental assemblies, the use of toggle switches should be kept to a minimum and it is recommended to use higher quality switches when possible. BNC style cables and connectors wear out over time and must be replaced when found faulty. When building BNC coaxial cables be sure to follow the manufacturer's guidelines for stripping dimensions and use the proper crimping tool for sturdy connections.

Solder joints represent the next most common failure point, often they are brittle and will break or dislodge when physically manipulated. This is typically the result of poor wetting when the joint was originally created. Proper solder joints should be smooth and shiny, almost wet in appearance. The solder itself should make a smooth fillet or ramp joining the pieces all around their contact area. Flux must always be used, not doing so will likely result in poor wetting. With proper techniques reliable joints are almost certain.

We experienced improved stability through the use of laser line filters on all photodiodes. For instance, shadows from personal walking pass the MOT power lock detector would cause perceivable fluctuations in MOT fluorescence. Using a 461 nm filter on the power monitor diode eliminated this unwanted effect.

It was found that for absolute best performance the ICCD camera should be triggered and exposed regularly. This helps with background subtraction by stabilizing the dark current level and the camera response but creates a risk of overexposing the camera that the operator must be mindful of. Starting and stopping the camera results in a $5 - 10$ minute detectable drift in signal level from even an empty expo-

sure. This rule of thumb applies throughout the experiment but is most notable in the camera, you simply want everything to be in a steady state from the start of data collection to the end.

In general, simple equals more reliable. Many times system performance was improved by utilizing less equipment. For example, large RF amplifiers with attenuators on their output were replaced with smaller RF amps and improved PDH lock performance was noticed. Circuits were more reliable with better noise performance by eliminating unused switches and extraneous circuitry.

Do not daisy chain power cables, instead distribute power from source in star configuration. The same applies for grounds. Coiling a cable turns it into an antenna, if a cable can not be shortened try to minimize the number of coils by making long runs.

D.2 Labview

The beauty of simplification carries over to the software world as well. Science often calls for on the fly measurements and unique tools and techniques that cause both physical and software systems to take on a Frankenstein nature. While the skill for such is useful, long term expandability of a system relies on having a strong and robust foundation. To this end the data collection process in Labview was reworked. Now the logical steps of data collection are functionalized into subvis resulting in a much cleaner and readable back panel. Data collection happens with the same sequence for absorption or fluorescence, background or image, and descriptive flags are placed in the batch file. Technique specific analysis is now handled solely in post analysis. The improvements help simplify a necessarily complex control program, avoid redundancy and facilitates the inclusion of new functionality.

D.2.1 10Hz Implementation

Previous methods of timing generation resulted in an experiment that was idle 49% of the time that it was 'running'. Using only the equipment already installed (and removing a home built trigger processor) the data collection rate was nearly doubled. The primary rep rate constraint for the experiment is that the Nd:YAG must fire it's flashlamps on a consistent 10 Hz clock. The somewhat reliable (10 ns jitter, 100 ns drift) internal clock use to serve as the master timing generator for the entire experiment. One pulse was used to sync the Pulseblaster and the next to ionize the plasma. We now provide that clock with the built in counter outputs of the PCI-6725 and can provide the proper presync (using two synchronized channels) without wasting every other shot. The clock reliability is also improved and t_0 is now absolutely stable to within 10 ns.

D.3 MATLAB

As analysis techniques become more involved and datasets larger MATLAB optimization becomes less of a nicety and more a necessity. Luckily there are a few simple rules that go a long way toward improve running times. By applying the following techniques the analysis runtime has been reduced by from hours to a few minutes.

The most common optimization advice is to vectorize whenever possible. MATLAB is inherently built to perform calculations on matrices, and it does so very efficiently. Using indices and for loops to process matrix elements one by one is often orders of magnitude slower than the same calculation performed in vector notation. For instance the following snippets of code both perform an element-wise sum on two random 10000 element vectors, yet the latter does so 13 times faster! More

complicated code will often benefit even more from vectorization.

```
tic
SumVal=0;
for i=1:size(x,1)
    SumVal(i)=x(i)+y(i);
end
toc
```

Elapsed time is 0.012494 seconds.

```
tic
SumVal=x+y;
toc
```

Elapsed time is 0.000967 seconds.

When it comes to data throughput in a PC the hard disk represents the bottleneck of any the subsystems thus it's access should be minimized and done so most efficiently. To this end we now store batch data in native MATLAB variable files. The very first time a dataset is analysed it will read in the .batch txt file from Labview which includes experimental parameters and pointers to the raw .dat files. The raw .dat files are read in using built-in MATLAB functions which can handle a wide array of data formats and are therefore very inefficient. Then all of this data is saved in a .m file which stores variables and their content in a format that MATLAB reads very efficiently, this is what will be read in on subsequent runs. For further time savings preprocessing can be performed before the data is re-saved and it will not need to be recalculated on subsequent analysis runs. Currently deconvolution with the PSF

is handled at this stage. Overall, this results in batch file processing times being reduced by about a factor of 30, from 33.06 s to 1.15 s for example.

It was found that next most intensive part of the analysis was calculating Voigt profiles and so the rather slow (albeit robust) built-in function for convolving the spectra was replaced by a more efficient and tailored trapezoidal approximation. This resulted in a marked decrease in spectral fit times, nearly an order of magnitude faster.

In general fitting routines make up most of the computational effort in analysis. For maximum efficiency the parameters should be scaled properly and tolerances adjusted per requirements. Its best to have all the fit parameters scaled near unity for proper convergence and error calculations.

D.4 LaTeX

For a process that is repeated by nearly every researcher in the world it's surprising how difficult it can be to create the proper image for inclusion into LaTeX. If done properly it's smooth and seamless, otherwise it can represent one of the largest challenges in writing a publication. Following are a few things found to largely impact the ease of the task. Use .png or .eps when possible, the former for bitmap images and the latter for vector formats. The essential difference is that vector graphics are scalable, the file is a set of instructions for drawing the image at any size with unlimited resolution. Meanwhile bitmap files store pixel by pixel color values for a finite number of pixels. This makes vector graphics best for plots, text, and simple diagrams. Bitmaps are more suitable for pictures or more complex drawings.

Avoid .jpg format, it is a compressed bitmap format (like .png) but is lossy and results in image artifacts. Solid colors will take on an array of values that complicate any manual touch-up or editing. For MATLAB figures save .fig file for future use.

For inclusion into LaTeXopen the figure with MATLAB and "save as" an .eps file with the size determine by the figure's PaperPosition property. This allows one to set the proper font size in order to match the body of the LaTeXdocument. GSView is good to auto calculate bounding boxes when missing from .eps files. bmp2eps is useful for converting .png or .bmp to an .eps file and epspdftk.exe for converting .pdf to .eps files.

Bibliography

[1] Y. Hayashi and K. Tachibana, "Observation of Coulomb-crystal formation from carbon particles grown in a methane plasma," *Japanese Journal of Applied Physics*, vol. 33, no. 6A, p. L804, 1994.

[2] J. M. Maxson, I. V. Bazarov, W. Wan, H. A. Padmore, and C. E. Coleman-Smith, "Fundamental photoemission brightness limit from disorder induced heating," *New Journal of Physics*, vol. 15, no. 10, p. 103024, 2013.

[3] S. D. Bergeson, A. Denning, M. Lyon, and F. Robicheaux, "Density and temperature scaling of disorder-induced heating in ultracold plasmas," *Phys. Rev. A*, vol. 83, p. 023409, Feb 2011.

[4] S. Ichimaru, "Strongly coupled plasmas: high-density classical plasmas and degenerate electron liquids," *Rev. Mod. Phys.*, vol. 54, pp. 1017–1059, Oct 1982.

[5] M. Bonitz, C. Henning, and D. Block, "Complex plasmas: a laboratory for strong correlations," *Reports on Progress in Physics*, vol. 73, no. 6, p. 066501, 2010.

[6] C. Deutsch, "Inertial confinement fusion driven by intense ion beams," in *Annales de Physique*, vol. 11, pp. 1–111, Les Editions de Physique, 1986.

[7] S. Atzeni and J. Meyer-ter Vehn, *The physics of inertial fusion*. Clarendon Press, 2004.

[8] S. Hu, B. Militzer, V. Goncharov, and S. Skupsky, "Strong coupling and degeneracy effects in inertial confinement fusion implosions," *Phys. Rev. Lett*, vol. 104, no. 23, p. 235003, 2010.

[9] M. Koenig, A. Benuzzi-Mounaix, A. Ravasio, T. Vinci, N. Ozaki, S. Lepape, D. Batani, G. Huser, T. Hall, D. Hicks, A. MacKinnon, P. Patel, H. S. Park, T. Boehly, M. Borghesi, S. Kar, and L. Romagnani, "Progress in the study of warm dense matter," *Plasma Physics and Controlled Fusion*, vol. 47, no. 12B, p. B441, 2005.

[10] P. K. Shukla, "A survey of dusty plasma physics," *Physics of Plasmas (1994-present)*, vol. 8, no. 5, pp. 1791–1803, 2001.

[11] M. S. Murillo, "Strongly coupled plasma physics and high energy-density matter," *Physics of Plasmas (1994-present)*, vol. 11, no. 5, pp. 2964–2971, 2004.

[12] J. P. Morrison, C. J. Rennick, J. S. Keller, and E. R. Grant, "Evolution from a molecular Rydberg gas to an ultracold plasma in a seeded supersonic expansion of no," *Phys. Rev. Lett.*, vol. 101, p. 205005, Nov 2008.

[13] V. Alekseev and I. Iakubov, "Non-ideal plasmas of metal vapours," *Physics Reports*, vol. 96, no. 1, pp. 1 – 69, 1983.

[14] V. E. Fortov and I. T. Iakubov, *The physics of non-ideal plasma*. World Scientific, 2000.

[15] M. R. Zaghloul, M. A. Bourham, J. Doster, and J. D. Powell, "On the average electronion momentum transport cross-section in ideal and non-ideal plasmas," *Physics Letters A*, vol. 262, no. 1, pp. 86 – 89, 1999.

[16] T. S. Ramazanov and S. K. Kodanova, "Coulomb logarithm of a nonideal plasma," *Physics of Plasmas (1994-present)*, vol. 8, no. 11, pp. 5049–5050, 2001.

[17] S. D. Baalrud and J. Daligault, "Extending plasma transport theory to strong coupling through the concept of an effective interaction potential," *Physics of Plasmas (1994-present)*, vol. 21, no. 5, p. 055707, 2014.

[18] J. P. Mithen, *Molecular dynamics simulations of the equilibrium dynamics of non-ideal plasmas*. Doctor of philosophy, University of Oxford, 2012.

[19] T. C. Killian, "Plasmas put in order," *Nature*, vol. 429, pp. 815–817, 2004.

[20] G. Bannasch, J. Castro, P. McQuillen, T. Pohl, and T. C. Killian, "Velocity relaxation in a strongly coupled plasma," *Phys. Rev. Lett.*, vol. 109, p. 185008, Nov 2012.

[21] J. Castro, G. Bannasch, P. McQuillen, T. Pohl, and T. C. Killian, "Creating non-maxwellian velocity distributions in ultracold plasmas," *AIP Conference Proceedings*, vol. 1421, no. 1, pp. 31–43, 2012.

[22] J. Castro, P. McQuillen, and T. C. Killian, "Ion acoustic waves in ultracold neutral plasmas," *Phys. Rev. Lett.*, vol. 105, p. 065004, Aug 2010.

[23] T. C. Killian, P. McQuillen, T. M. ONeil, and J. Castro, "Creating and studying ion acoustic waves in ultracold neutral plasmasa)," *Physics of Plasmas (1994-present)*, vol. 19, no. 5, p. 055701, 2012.

[24] P. McQuillen, J. Castro, T. Strickler, S. J. Bradshaw, and T. C. Killian, "Ion holes in the hydrodynamic regime in ultracold neutral plasmas," *Physics of*

Plasmas (1994-present), vol. 20, no. 4, p. 043516, 2013.

[25] S. Kulin, T. C. Killian, S. D. Bergeson, and S. L. Rolston, "Plasma oscillations and expansion of an ultracold neutral plasma," *Phys. Rev. Lett.*, vol. 85, pp. 318–321, Jul 2000.

[26] R. S. Fletcher, X. L. Zhang, and S. L. Rolston, "Observation of collective modes of ultracold plasmas," *Phys. Rev. Lett.*, vol. 96, p. 105003, Mar 2006.

[27] K. A. Twedt and S. L. Rolston, "Electronic detection of collective modes of an ultracold plasma," *Phys. Rev. Lett.*, vol. 108, p. 065003, Feb 2012.

[28] A. Lyubonko, T. Pohl, and J.-M. Rost, "Collective energy absorption of ultracold plasmas through electronic edge-modes," *New Journal of Physics*, vol. 14, no. 5, p. 053039, 2012.

[29] M. P. Robinson, B. L. Tolra, M. W. Noel, T. F. Gallagher, and P. Pillet, "Spontaneous evolution of Rydberg atoms into an ultracold plasma," *Phys. Rev. Lett.*, vol. 85, pp. 4466–4469, Nov 2000.

[30] T. Pohl, T. Pattard, and J. M. Rost, "Plasma formation from ultracold Rydberg gases," *Phys. Rev. A*, vol. 68, p. 010703, Jul 2003.

[31] T. C. Killian, M. J. Lim, S. Kulin, R. Dumke, S. D. Bergeson, and S. L. Rolston, "Formation of Rydberg atoms in an expanding ultracold neutral plasma," *Phys. Rev. Lett.*, vol. 86, pp. 3759–3762, Apr 2001.

[32] T. F. Gallagher, P. Pillet, M. P. Robinson, B. Laburthe-Tolra, and M. W. Noel, "Back and forth between Rydberg atoms and ultracold plasmas," *J. Opt. Soc. Am. B*, vol. 20, pp. 1091–1097, May 2003.

[33] P. McQuillen, X. Zhang, T. Strickler, F. B. Dunning, and T. C. Killian, "Imaging the evolution of an ultracold strontium Rydberg gas," *Phys. Rev. A*, vol. 87, p. 013407, Jan 2013.

[34] C. E. Simien, Y. C. Chen, P. Gupta, S. Laha, Y. N. Martinez, P. G. Mickelson, S. B. Nagel, and T. C. Killian, "Using absorption imaging to study ion dynamics in an ultracold neutral plasma," *Phys. Rev. Lett.*, vol. 92, p. 143001, Apr 2004.

[35] E. A. Cummings, J. E. Daily, D. S. Durfee, and S. D. Bergeson, "Fluorescence measurements of expanding strongly coupled neutral plasmas," *Phys. Rev. Lett.*, vol. 95, p. 235001, Nov 2005.

[36] T. C. Killian, T. Pattard, T. Pohl, and J. M. Rost, "Ultracold neutral plasmas," *Physics Reports*, vol. 449, p. 77, 2007.

[37] T. C. Killian, V. S. Ashoka, P. Gupta, S. Laha, S. B. Nagel, C. E. Simien, S. Kulin, S. L. Rolston, and S. D. Bergeson, "Ultracold neutral plasmas: recent experiments and new prospects," *Journal of Physics A: Mathematical and General*, vol. 36, no. 22, p. 6077, 2003.

[38] T. Pohl, T. Pattard, and J. M. Rost, "Coulomb crystallization in expanding laser-cooled neutral plasmas," *Phys. Rev. Lett.*, vol. 92, p. 155003, Apr 2004.

[39] D. Gericke and M. Murillo, "Disorder-induced heating of ultracold plasmas," *Contributions to Plasma Physics*, vol. 43, no. 5-6, pp. 298–301, 2003.

[40] T. Pohl, T. Pattard, and J. M. Rost, "On the possibility of 'correlation cooling' of ultracold neutral plasmas," *Journal of Physics B: Atomic, Molecular and Optical Physics*, vol. 37, no. 9, p. L183, 2004.

[41] M. S. Murillo, "Using Fermi statistics to create strongly coupled ion plasmas in atom traps," *Phys. Rev. Lett.*, vol. 87, p. 115003, Aug 2001.

[42] G. Bannasch, T. C. Killian, and T. Pohl, "Strongly coupled plasmas via Rydberg blockade of cold atoms," *Phys. Rev. Lett.*, vol. 110, p. 253003, Jun 2013.

[43] Y. Klimontovich and D. Haar, *Kinetic Theory of Nonideal Gases and Nonideal Plasmas: International Series in Natural Philosophy*. International series in natural philosophy, Elsevier Science, 2013.

[44] M. H. J. Hagen, I. Pagonabarraga, C. P. Lowe, and D. Frenkel, "Algebraic decay of velocity fluctuations in a confined fluid," *Phys. Rev. Lett.*, vol. 78, pp. 3785–3788, May 1997.

[45] M. Bonitz, D. Semkat, and D. Kremp, "Short-time dynamics of correlated many-particle systems: Molecular dynamics versus quantum kinetics," *Physical Review E*, vol. 56, no. 1, p. 1246, 1997.

[46] K. Morawetz, "The Landau equation including memory and energy conservation," *Physics Letters A*, vol. 199, no. 34, pp. 241 – 244, 1995.

[47] K. Morawetz, V. Špička, and P. Lipavský, "Formation of binary correlations in strongly coupled plasmas," *Physics Letters A*, vol. 246, no. 34, pp. 311 – 317, 1998.

[48] G. Zwicknagel, "Molecular dynamics simulations of the dynamics of correlations and relaxation in an OCP," *Contributions to Plasma Physics*, vol. 39, no. 1-2, pp. 155–158, 1999.

[49] K. Morawetz, M. Bonitz, V. G. Morozov, G. Röpke, and D. Kremp, "Short-time dynamics with initial correlations," *Phys. Rev. E*, vol. 63, p. 020102, Jan 2001.

[50] Z. Donkó, G. J. Kalman, and K. I. Golden, "Caging of particles in one-component plasmas," *Phys. Rev. Lett.*, vol. 88, p. 225001, May 2002.

[51] J. Daligault, "Liquid-state properties of a one-component plasma," *Phys. Rev. Lett.*, vol. 96, p. 065003, Feb 2006.

[52] J. Daligault, "Diffusion in ionic mixtures across coupling regimes," *Phys. Rev. Lett.*, vol. 108, p. 225004, May 2012.

[53] T. Pohl, T. Pattard, and J. M. Rost, "Kinetic modeling and molecular dynamics simulation of ultracold neutral plasmas including ionic correlations," *Phys. Rev. A*, vol. 70, p. 033416, Sep 2004.

[54] P. McQuillen, T. Strickler, T. Langin, and T. C. Killian, "Ion temperature evolution in an ultracold neutral plasma," *Physics of Plasmas (1994-present)*, vol. 22, no. 3, p. 033513, 2015.

[55] A. V. Gurevich, L. V. Pariiskaya, and L. P. Pitaevskii, "Self-similar motion of rarefied plasma," *J. Exptl. and Theoret. Phys. (U.S.S.R.)*, vol. 49, pp. 647–654, 1965.

[56] J. Denavit, "Collisionless plasma expansion into a vacuum," *Physics of Fluids (1958-1988)*, vol. 22, no. 7, pp. 1384–1392, 1979.

[57] P. Mora and R. Pellat, "Selfsimilar expansion of a plasma into a vacuum," *Physics of Fluids (1958-1988)*, vol. 22, no. 12, pp. 2300–2304, 1979.

[58] C. Sack and H. Schamel, "Plasma expansion into vacuum a hydrodynamic approach," *Physics Reports*, vol. 156, no. 6, pp. 311 – 395, 1987.

[59] D. S. Dorozhkina and V. E. Semenov, "Exact solution of Vlasov equations for quasineutral expansion of plasma bunch into vacuum," *Phys. Rev. Lett.*, vol. 81, pp. 2691–2694, Sep 1998.

[60] A. V. Baitin and K. M. Kuzanyan, "A self-similar solution for expansion into a vacuum of a collisionless plasma bunch," *Journal of Plasma Physics*, vol. 59, pp. 83–90, 1 1998.

[61] P. Mora, "Plasma expansion into a vacuum," *Phys. Rev. Lett.*, vol. 90, p. 185002, May 2003.

[62] P. Mora, "Collisionless expansion of a Gaussian plasma into a vacuum," *Physics of Plasmas (1994-present)*, vol. 12, no. 11, p. 112102, 2005.

[63] S. Betti, F. Ceccherini, F. Cornolti, and F. Pegoraro, "Expansion of a finite-size plasma in vacuum," *Plasma Physics and Controlled Fusion*, vol. 47, no. 3, p. 521, 2005.

[64] T. Grismayer and P. Mora, "Influence of a finite initial ion density gradient on plasma expansion into a vacuum," *Physics of Plasmas (1994-present)*, vol. 13, no. 3, p. 032103, 2006.

[65] S. Laha, P. Gupta, C. E. Simien, H. Gao, J. Castro, T. Pohl, and T. C. Killian, "Experimental realization of an exact solution to the Vlasov equations for an expanding plasma," *Phys. Rev. Lett.*, vol. 99, p. 155001, Oct 2007.

[66] J. Castro, H. Gao, and T. C. Killian, "Using sheet fluorescence to probe ion dynamics in an ultracold neutral plasma," *Plasma Physics and Controlled Fusion*, vol. 50, no. 12, p. 124011, 2008.

[67] M. D. Perry and G. Mourou, "Terawatt to petawatt subpicosecond lasers," *Science*, vol. 264, no. 5161, pp. 917–924, 1994.

[68] J. Lindl, "Development of the indirect-drive approach to inertial confinement fusion and the target physics basis for ignition and gain," *Physics of Plasmas (1994-present)*, vol. 2, no. 11, pp. 3933–4024, 1995.

[69] H. Daido, "Review of soft x-ray laser researches and developments," *Reports on Progress in Physics*, vol. 65, no. 10, p. 1513, 2002.

[70] E. L. Clark, K. Krushelnick, M. Zepf, F. N. Beg, M. Tatarakis, A. Machacek, M. I. K. Santala, I. Watts, P. A. Norreys, and A. E. Dangor, "Energetic heavy-ion and proton generation from ultraintense laser-plasma interactions with solids," *Phys. Rev. Lett.*, vol. 85, pp. 1654–1657, Aug 2000.

[71] R. A. Snavely, M. H. Key, S. P. Hatchett, T. E. Cowan, M. Roth, T. W. Phillips, M. A. Stoyer, E. A. Henry, T. C. Sangster, M. S. Singh, S. C. Wilks, A. MacKinnon, A. Offenberger, D. M. Pennington, K. Yasuike, A. B. Langdon, B. F. Lasinski, J. Johnson, M. D. Perry, and E. M. Campbell, "Intense high-energy proton beams from petawatt-laser irradiation of solids," *Phys. Rev. Lett.*, vol. 85, pp. 2945–2948, Oct 2000.

[72] A. Maksimchuk, S. Gu, K. Flippo, D. Umstadter, and V. Y. Bychenkov, "Forward ion acceleration in thin films driven by a high-intensity laser," *Phys. Rev. Lett.*, vol. 84, pp. 4108–4111, May 2000.

[73] D. R. Symes, M. Hohenberger, A. Henig, and T. Ditmire, "Anisotropic explosions of hydrogen clusters under intense femtosecond laser irradiation," *Phys. Rev. Lett.*, vol. 98, p. 123401, Mar 2007.

[74] T. Pohl, T. Pattard, and J. M. Rost, "Relaxation to nonequilibrium in expanding ultracold neutral plasmas," *Phys. Rev. Lett.*, vol. 94, p. 205003, May 2005.

[75] T. Pohl, T. Pattard, and J. M. Rost, "Influence of electronion collisions on Coulomb crystallization of ultracold neutral plasmas," *Journal of Physics B: Atomic, Molecular and Optical Physics*, vol. 38, no. 2, p. S343, 2005.

[76] M. S. Murillo and M. W. C. Dharma-wardana, "Temperature relaxation in hot dense hydrogen," *Phys. Rev. Lett.*, vol. 100, p. 205005, May 2008.

[77] J. N. Glosli, F. R. Graziani, R. M. More, M. S. Murillo, F. H. Streitz, M. P. Surh, L. X. Benedict, S. Hau-Riege, A. B. Langdon, and R. A. London, "Molecular dynamics simulations of temperature equilibration in dense hydrogen," *Phys. Rev. E*, vol. 78, p. 025401, Aug 2008.

[78] J. Hansen and I. McDonald, "Thermal relaxation in a strongly coupled two-temperature plasma," *Physics Letters A*, vol. 97, no. 12, pp. 42 – 44, 1983.

[79] L. S. Brown, D. L. Preston, and R. L. S. Jr., "Charged particle motion in a highly ionized plasma," *Physics Reports*, vol. 410, no. 4, pp. 237 – 333, 2005.

[80] G. Dimonte and J. Daligault, "Molecular-dynamics simulations of electron-ion temperature relaxation in a classical Coulomb plasma," *Phys. Rev. Lett.*, vol. 101, p. 135001, Sep 2008.

[81] J. Daligault and G. Dimonte, "Correlation effects on the temperature-relaxation rates in dense plasmas," *Physical Review E*, vol. 79, no. 5, p. 056403, 2009.

[82] L. S. Brown and R. L. Singleton, "Temperature equilibration in a fully ionized plasma: Electron-ion mass ratio effects," *Phys. Rev. E*, vol. 79, p. 066407, Jun 2009.

[83] S. Ichimaru, S. Mitake, S. Tanaka, and X.-Z. Yan, "Theory of interparticle correlations in dense, high-temperature plasmas. I. General formalism," *Phys. Rev. A*, vol. 32, pp. 1768–1774, Sep 1985.

[84] Z. Donkó, B. Nyíri, L. Szalai, and S. Holló, "Thermal conductivity of the classical electron one-component plasma," *Phys. Rev. Lett.*, vol. 81, pp. 1622–1625, Aug 1998.

[85] L. Spitzer and R. Härm, "Transport phenomena in a completely ionized gas," *Phys. Rev.*, vol. 89, pp. 977–981, Mar 1953.

[86] Y. T. Lee and R. M. More, "An electron conductivity model for dense plasmas," *Physics of Fluids (1958-1988)*, vol. 27, no. 5, pp. 1273–1286, 1984.

[87] S. Ichimaru and S. Tanaka, "Theory of interparticle correlations in dense, high-temperature plasmas. V. Electric and thermal conductivities," *Phys. Rev. A*, vol. 32, pp. 1790–1798, Sep 1985.

[88] V. Mintsev, V. Fortov, and V. Gryaznov, "Electric conductivity of a high-temperature nonideal plasma," *JETP*, vol. 52, no. 1, p. 59, 1980.

[89] D. B. Boercker, "Kinetic theory of electrical conductivity in plasmas," *Phys. Rev. A*, vol. 23, pp. 1969–1981, Apr 1981.

[90] D. B. Boercker, F. J. Rogers, and H. E. DeWitt, "Electron collision frequency in plasmas," *Phys. Rev. A*, vol. 25, pp. 1623–1631, Mar 1982.

[91] J. R. Adams, N. S. Shilkin, V. E. Fortov, V. K. Gryaznov, V. B. Mintsev, R. Redmer, H. Reinholz, and G. Röpke, "Coulomb contribution to the direct current electrical conductivity of dense partially ionized plasmas," *Physics of Plasmas (1994-present)*, vol. 14, no. 6, p. 062303, 2007.

[92] T. C. Killian, Y. C. Chen, P. Gupta, S. Laha, Y. N. Martinez, P. G. Mickelson, S. B. Nagel, A. D. Saenz, and C. E. Simien, "Absorption imaging and spectroscopy of ultracold neutral plasmas," *Journal of Physics B: Atomic, Molecular and Optical Physics*, vol. 38, no. 2, p. S351, 2005.

[93] S. Laha, Y. C. Chen, P. Gupta, C. E. Simien, Y. N. Martinez, P. G. Mickelson, S. B. Nagel, and T. C. Killian, "Kinetic energy oscillations in annular regions of ultracold neutral plasmas," *The European Physical Journal D - Atomic, Molecular, Optical and Plasma Physics*, vol. 40, no. 1, pp. 51–56, 2006.

[94] S. Laha, J. Castro, H. Gao, P. Gupta, C. E. Simien, and T. C. Killian, "Optical probes of ultracold neutral plasmas," *AIP Conference Proceedings*, vol. 926, no. 1, pp. 69–78, 2007.

[95] P. McQuillen, "High resolution sculpting and imaging of ultracold neutral plasmas," master of science thesis, Rice University, 2012.

[96] W. E. Cooke, T. F. Gallagher, S. A. Edelstein, and R. M. Hill, "Doubly excited autoionizing Rydberg states of sr," *Phys. Rev. Lett.*, vol. 40, pp. 178–181, Jan 1978.

[97] S. ul Haq, S. Mahmood, N. Amin, Y. Jamil, R. Ali, and M. A. Baig, "Measurements of photoionization cross sections from the 5s5p $^1\mathbf{P_1}$ and 5s6s $^1\mathbf{S_0}$ excited states of strontium," *Journal of Physics B: Atomic, Molecular and Optical Physics*, vol. 39, no. 7, p. 1587, 2006.

[98] A. Siegman, *Lasers*. University Science Books, 1986.

[99] G. Reinaudi, T. Lahaye, Z. Wang, and D. Guéry-Odelin, "Strong saturation absorption imaging of dense clouds of ultracold atoms," *Opt. Lett.*, vol. 32, pp. 3143–3145, Nov 2007.

[100] A. Madej, L. Marmet, and J. Bernard, "Rb atomic absorption line reference for single Sr^+ laser cooling systems," *Applied Physics B*, vol. 67, no. 2, pp. 229–234, 1998.

[101] A. Sinclair, M. Wilson, and P. Gill, "Improved three-dimensional control of a single strontium ion in an endcap trap," *Optics Comm.*, vol. 190, no. 1-6, pp. 193–203, 2001.

[102] A. Shiner, A. Madej, P. Dubé, and J. Bernard, "Absolute optical frequency measurement of saturated absorption lines in Rb near 422 nm," *Applied Physics B*, vol. 89, no. 4, pp. 595–601, 2007.

[103] F. Robicheaux and J. D. Hanson, "Simulated expansion of an ultra-cold, neutral plasma," *Physics of Plasmas (1994-present)*, vol. 10, no. 6, pp. 2217–2229, 2003.

[104] T. C. Killian, S. Kulin, S. D. Bergeson, L. A. Orozco, C. Orzel, and S. L. Rolston, "Creation of an ultracold neutral plasma," *Phys. Rev. Lett.*, vol. 83, pp. 4776–4779, Dec 1999.

[105] T. Wilson, W.-T. Chen, and J. Roberts, "Influence of electron evaporative cooling on ultracold plasma expansion," *Physics of Plasmas (1994-present)*, vol. 20, no. 7, p. 073503, 2013.

[106] E. A. Cummings, J. E. Daily, D. S. Durfee, and S. D. Bergeson, "Ultracold neutral plasma expansion in two dimensions," *Physics of Plasmas (1994-present)*, vol. 12, no. 12, p. 123501, 2005.

[107] Y. C. Chen, C. E. Simien, S. Laha, P. Gupta, Y. N. Martinez, P. G. Mickelson, S. B. Nagel, and T. C. Killian, "Electron screening and kinetic-energy oscillations in a strongly coupled plasma," *Phys. Rev. Lett.*, vol. 93, p. 265003, Dec 2004.

[108] M. Lyon and S. D. Bergeson, "The influence of electron screening on disorder-induced heating," *Journal of Physics B: Atomic, Molecular and Optical Physics*, vol. 44, no. 18, p. 184014, 2011.

[109] F. Robicheaux and J. D. Hanson, "Simulation of the expansion of an ultracold neutral plasma," *Phys. Rev. Lett.*, vol. 88, p. 055002, Jan 2002.

[110] L. Guo, R. H. Lu, and S. S. Han, "Molecular dynamics simulation of disorder-induced heating in ultracold neutral plasma," *Phys. Rev. E*, vol. 81, p. 046406, Apr 2010.

[111] L. Jin-Xing, C. Ming-Tao, H. Liang, Q. Yue-Rong, Z. Shou-Gang, G. Hong, L. Fu-Li, and T. C. Killian, "Calculation of ion equilibrium temperature in ultracold neutral plasmas," *Chinese Physics Letters*, vol. 28, no. 12, p. 123201, 2011.

[112] M. Lyon, S. D. Bergeson, and M. S. Murillo, "Limit of strong ion coupling due to electron shielding," *Phys. Rev. E*, vol. 87, p. 033101, Mar 2013.

[113] S. G. Kuzmin and T. M. ONeil, "Numerical simulation of ultracold plasmas," *Physics of Plasmas (1994-present)*, vol. 9, no. 9, pp. 3743–3751, 2002.

[114] S. G. Kuzmin and T. M. O'Neil, "Numerical simulation of ultracold plasmas: How rapid intrinsic heating limits the development of correlation," *Phys. Rev. Lett.*, vol. 88, p. 065003, Jan 2002.

[115] R. T. Farouki and S. Hamaguchi, "Thermodynamics of stronglycoupled Yukawa systems near the one-componentplasma limit. II. Molecular dynamics simulations," *The Journal of Chemical Physics*, vol. 101, no. 11, pp. 9885–9893, 1994.

[116] S. Hamaguchi, R. T. Farouki, and D. H. E. Dubin, "Phase diagram of Yukawa systems near the onecomponentplasma limit revisited," *The Journal of Chemical Physics*, vol. 105, no. 17, pp. 7641–7647, 1996.

[117] S. Hamaguchi, R. T. Farouki, and D. H. E. Dubin, "Triple point of Yukawa systems," *Phys. Rev. E*, vol. 56, pp. 4671–4682, Oct 1997.

[118] G. Chabrier and A. Y. Potekhin, "Equation of state of fully ionized electron-ion plasmas," *Phys. Rev. E*, vol. 58, pp. 4941–4949, Oct 1998.

[119] L. Spitzer, *Physics of Fully Ionized Gases*. Interscience tracts on physics and astronomy, 3, Interscience Publishers, 1956.

[120] D. Rose and M. Clark, *Plasmas and controlled fusion: by David J. Rose and Melville Clark, Jr.* M.I.T. Press, 1961.

[121] A. Ng, P. Celliers, G. Xu, and A. Forsman, "Electron-ion equilibration in a strongly coupled plasma," *Phys. Rev. E*, vol. 52, pp. 4299–4310, Oct 1995.

[122] L. Landau, "Kinetic equation for the Coulomb effect," *Phys. Z. Sowjetunion*, vol. 10, p. 154, 1936.

[123] R. S. Cohen, L. Spitzer, and P. M. Routly, "The electrical conductivity of an ionized gas," *Phys. Rev.*, vol. 80, pp. 230–238, Oct 1950.

[124] W. B. Thompson and J. Hubbard, "Long-range forces and the diffusion coefficients of a plasma," *Rev. Mod. Phys.*, vol. 32, pp. 714–718, Oct 1960.

[125] R. L. Liboff, "Transport coefficients determined using the shielded Coulomb potential," *Physics of Fluids (1958-1988)*, vol. 2, no. 1, pp. 40–46, 1959.

[126] T. Kihara and O. Aono, "Unified theory of relaxations in plasmas, I. basic theorem," *Journal of the Physical Society of Japan*, vol. 18, no. 6, pp. 837–851, 1963.

[127] L. S. Brown, D. L. Preston, and R. L. S. Jr., "Charged particle motion in a highly ionized plasma," *Physics Reports*, vol. 410, no. 4, pp. 237 – 333, 2005.

[128] D. O. Gericke, M. S. Murillo, and M. Schlanges, "Dense plasma temperature equilibration in the binary collision approximation," *Phys. Rev. E*, vol. 65, p. 036418, Mar 2002.

[129] J. D. Callen, "Fundamentals of plasma physics." http://homepages.cae.wisc.edu/ callen/book.html, 2006. Book Draft.

[130] I. Hutchinson, "Collisions in plasmas." http://ocw.mit.edu/courses/nuclear-engineering/22-611j-introduction-to-plasma-physics-i-fall-2006/readings/chap3.pdf, 2003. Lecture Notes.

[131] P. Gupta, S. Laha, C. E. Simien, H. Gao, J. Castro, T. C. Killian, and T. Pohl, "Electron-temperature evolution in expanding ultracold neutral plasmas," *Phys. Rev. Lett.*, vol. 99, p. 075005, Aug 2007.

[132] T. Pohl, D. Vrinceanu, and H. R. Sadeghpour, "Rydberg atom formation in ultracold plasmas: Small energy transfer with large consequences," *Phys. Rev. Lett.*, vol. 100, p. 223201, Jun 2008.

[133] G. Bannasch and T. Pohl, "Rydberg-atom formation in strongly correlated ultracold plasmas," *Phys. Rev. A*, vol. 84, p. 052710, Nov 2011.

[134] R. S. Fletcher, X. L. Zhang, and S. L. Rolston, "Using three-body recombination to extract electron temperatures of ultracold plasmas," *Phys. Rev. Lett.*, vol. 99, p. 145001, Oct 2007.

[135] H. Sadeghi, A. Kruyen, J. Hung, H. Gurian, J. P. Morrison, J. M. Schulz-Weiling, N. Saquet, J. Rennick, C. and R. Grant, E. "Dissociation and the development of spatial correlation in a molecular ultracold plasma," *Phys. Rev. Lett.*, vol. 112, p. 075001, Feb 2014.

[136] Z. Donko and P. Hartmann, "Thermal conductivity of strongly coupled Yukawa liquids," *Phys. Rev. E*, vol. 69, no. 1, p. 016405, 2004.

[137] R. Gonzalez and R. Woods, *Digital Image Processing.* Pearson/Prentice Hall, 2008.

[138] P. McQuillen, J. Castro, and T. C. Killian, "High-resolution ionization of ultracold neutral plasmas," *Journal of Physics B: Atomic, Molecular and Optical Physics*, vol. 44, no. 18, p. 184013, 2011.

[139] P. Hellinger and P. Trávníček, "Effective collision frequency due to ion-acoustic instability: Theory and simulations," *Geophysical Research Letters*, vol. 31, p. L10806, 2004.

[140] A. Buades, B. Coll, and J. M. Morel, "A review of image denoising algorithms, with a new one," *Multiscale Modeling & Simulation*, vol. 4, no. 2, pp. 490–530, 2005.

[141] A. D. R. Girón and H. L. Correa, "A new algorithm for detecting and correcting bad pixels in infrared images," *Ingeniería e Investigación*, vol. 30, pp. 197 – 207, 08 2010.